EXPERIMENTAL AND ANALYTICAL STUDIES ON THE EVALUATION OF ELASTOMERIC BRIDGE BEARINGS

EXPERIMENTAL AND ANALYTICAL STUDIES ON THE EVALUATION OF ELASTOMERIC BRIDGE BEARINGS

By

Seyed Saleh Ahmadi Soleimani

B.Sc., M.Sc.

A Thesis Submitted to the School of Graduate
Studies in Partial Fulfilment of the Requirements for
the Degree

Doctor of Philosophy

McMaster University
Hamilton, Ontario, Canada
April 2022

Doctor of Philosophy (2022) (Civil Engineering)

McMaster University Hamilton, Ontario

TITLE:	Experimental and Analytical Studies on the Evaluation of Elastomeric Bridge Bearings
AUTHOR:	Seyed Saleh Ahmadi Soleimani, B.Sc., M.Sc.
SUPERVISORS:	Georgios Balomenos, Ph.D., P.Eng.
	Dimitrios Konstantinidis, Ph.D.
NUMBER OF PAGES:	xxviii, 142

Dedicated

to my mother for her endless love, support, and encouragement,

and to the memory of my father.

May his memory forever be a comfort and blessing

Abstract

Elastomeric bridge bearings (composed of alternating rubber layers and steel laminates surrounded by a rubber cover all around) have been historically introduced between the girder and the pier or abutment to accommodate service-level movements and rotations. During a seismic event, these bearings can also experience deformation demands that are considerably larger than the service-level demands. The manufacturing process of these bearings involves compression molding during which imperfections such as vertically misaligned, rotationally misaligned, and bent steel laminates might develop. The current quality control procedures for bearings involve costly, time-consuming, destructive tests on sample bearings. Therefore, there is a need for an efficient, nondestructive methodology for quality control testing of bearings. In addition, these bearings are a key component of the bridge, and thus the effects of manufacturing imperfections on different aspects of the bearing's performance must be understood and quantified.

In the first phase of this research, an efficient vision-based assessment methodology was developed for the nondestructive identification of the internal structure of elastomeric bridge bearings and their potential imperfections. The developed methodology requires the application of three-dimensional digital image correlation (3D-DIC) and relies on the local extrema forming in displacement and strain fields on the vertical sides of compressed bearings. In the next two phases, extensive nonlinear 3D FEA studies were undertaken to evaluate the effects of imperfections on the behavior of bearings under maximum service loading and under large lateral displacements resulting from seismic actions. Based on the FEAs results, imperfections are not expected to trigger shear delamination in bearings and their increased vertical deflections due to imperfections would be also minimal. However, imperfections can appreciably increase the tensile stresses in the laminates and lead to greater extents of plasticity in them. In the third phase of this research, the examined bearings were subjected to simultaneous axial loading and five cycles of lateral displacements with increasing amplitudes, up to 200% of their total rubber thickness. It was found that imperfections do not cause a considerable difference in the overall deformed shape of bearings but can expedite the rollover of bearings in lower shear strains and

increase their risks of instability. Although all the examined bearings exhibited fairly stable hysteretic response, their effective lateral stiffness and lateral force could increase up to 18% and 40%, respectively, due to imperfections. Imperfections could also increase damage measured using a plastic-energy-based damage factor by up to more than five times for bearings subjected to the five-cycle displacement protocol. However, the yielded laminates in all examined bearings under maximum service loading or cyclic lateral displacement were far from fracturing. The increase of plastic damage during a strong earthquake and due to imperfections is not expected to cause immediate failure of bearings, provided that no or limited plastic damage occurs prior to that and under the service-level condition.

The proposed nondestructive methodology can be adopted by departments/ministries of transportation as an alternative to the current destructive approaches for quality control of elastomeric bearings. For bearings subjected to maximum service loading, the use of sufficiently thick laminates (e.g., 4-mm-thick) is suggested to prevent plastic damage to the laminates, and thus alleviate concerns about the service-level performance of the bearings. Considering the risks of rollover, instability, and spread of plastic damage in the laminates under cyclic loading, slender bearings with laminate thicknesses of 2 mm, or less, and slender bearings in which the majority of laminates feature relatively large rotational misalignments (in the order of 0.025 rad, or more) should be avoided.

Acknowledgements

My sincere gratitude goes to my supervisors Dr. Dimitrios Konstantinidis and Dr. Georgios Balomenos for their consistent support, guidance, and patience throughout this research. Their immense knowledge and plentiful experience have truly encouraged me throughout the course of my Ph.D. I am also extremely grateful to the previous and current members of my supervisory committee, Dr. Michael Tait and Dr. Ken Sivakumaran, and Dr. Cancan Yang for their valuable comments and suggestions.

I would like to appreciate the Ministry of Transportation of Ontario (MTO) for the financial support. I am very grateful to Kris Mermigas (Head Engineer, Structures Office, MTO), Jennifer Astle-Tranmer (Senior Materials Officer), and Ben Huh (Lead Engineer, Structures Office, MTO) for their committed support during this research.

I would also like to thank the technical staffs at the ADL: Mr. Kent Wheeler and Mr. Paul Heerema. The experimental study would not have been possible without their support.

My gratitude extends to all my friends and colleagues for their moral supports, helpful discussions, and encouragements.

Finally and most importantly, I would like to express my deepest appreciation to my family for their love and spiritual support without which the completion of my dissertation would not have been possible.

Contents

List of Tables

List of Figures

Figure 4.17 Ω and μ_ε of examined bearings with geometries (a) B1, (b) B2, and (c) B3126

Co-Authorship

This thesis has been prepared in accordance with the regulations for a 'Sandwich' thesis format or as a compilation of papers stipulated by the Faculty of Graduate Studies at McMaster University. The work was completed under the supervision, guidance, and review of Dr. Georgios Balomenos and Dr. Dimitrios Konstantinidis. Initially, Dr. Konstantinidis served as the first supervisor and Dr. Balomenos as the second supervisor (September 2017-December 2018). When Dr. Konstantinidis left McMaster University, Dr. Balomenos assumed the role of first supervisor and Dr. Konstantinidis became the second supervisor. Chapters 2 to 4 of the thesis have been co-authored as:

Chapter 2: Nondestructive Assessment of Elastomeric Bridge Bearings Using 3D Digital Image Correlation

Authors: Seyed Saleh Ahmadi Soleimani, Dimitrios Konstantinidis, and Georgios Balomenos

This chapter has been published in the *ASCE Journal of Structural Engineering*, Vol. 148, Issue 1 (January 2022), 04021233, Reston, VA, DOI: 10.1061/(ASCE)ST.1943-541X.0003200. The roles of contributors to this article were as follows:

Seyed Saleh Ahmadi Soleimani: Literature review and conducting a research process; development or design of methodology; creation and validation of models; programming; implementation of the computer code and supporting algorithms; designing and building the experimental setup; performing the experiments; application of mathematical and computational techniques to analyze data; preparation and creation of the published work, specifically writing the initial draft; critical reviews and revisions in preparation of the published work

Dimitrios Konstantinidis: Conceptualization and formulation of ideas and goals; acquisition of the financial support for the project leading to this publication; development or design of methodology; provision of study materials, laboratory samples, devices, instruments, computing resources, or other analysis tools; critical reviews and revisions in

preparation of the published work; supervision for the research activity planning and execution

Georgios P. Balomenos: Development or design of methodology; provision of study materials, laboratory samples, devices, instruments, computing resources, or other analysis tools; critical reviews and revisions in preparation of the published work; supervision for the research activity planning and execution

Chapter 3: Effect of Manufacturing Imperfections on the Service-level Performance of Elastomeric Bridge Bearings

Authors: Seyed Saleh Ahmadi Soleimani, Dimitrios Konstantinidis, and Georgios Balomenos

This chapter has been accepted for publication in the *ASCE Journal of Structural Engineering (in-press as of the submission date of this thesis)*. The roles of contributors to this article were as follows:

Seyed Saleh Ahmadi Soleimani: Conceptualization of ideas and goals; literature review and conducting a research process; development or design of methodology; creation and validation of models; programming; implementation of the computer code; application of mathematical and computational techniques to analyze data; preparation and creation of the published work, specifically writing the initial draft; critical reviews and revisions in preparation of the published work

Dimitrios Konstantinidis: Acquisition of the financial support for the project leading to this publication; development or design of methodology; provision of computing resources; critical reviews and revisions in preparation of the published work; supervision for the research activity planning and execution

Georgios P. Balomenos: Development or design of methodology; provision of computing resources; Programming; critical reviews and revisions in preparation of the published work; supervision for the research activity planning and execution

Chapter 4: Effects of Steel Laminate Characteristics and Imperfections on the Behavior of Unbonded Elastomeric Bridge Bearings Subjected to Large Lateral Displacements

Authors: Seyed Saleh Ahmadi Soleimani, Dimitrios Konstantinidis, and Georgios Balomenos

This chapter will be submitted for publication in a peer-reviewed journal. The roles of contributors to this article were as follows:

Seyed Saleh Ahmadi Soleimani: Literature review and conducting a research process; development or design of methodology; creation and validation of models; programming; implementation of the computer code; application of mathematical and computational techniques to analyze data; preparation and creation of the published work, specifically writing the initial draft; critical reviews and revisions in preparation of the published work

Dimitrios Konstantinidis: Conceptualization of ideas and goals; acquisition of the financial support for the project leading to this publication; development or design of methodology; provision of computing resources; critical reviews and revisions in preparation of the published work; supervision for the research activity planning and execution

Georgios P. Balomenos: Development or design of methodology; provision of computing resources; Programming; critical reviews and revisions in preparation of the published work; supervision for the research activity planning and execution

List of Symbols

A	Creep parameter in the hysteretic model
A_h	Bearing's plan area
A_p	Yielded area of a steel laminate of a bearing
$\overline{A}_p$	Plastic area ratio (= A_p/A_s)
A_s	Plan area of steel laminates of a bearing
C	Creep strain exponent in the hysteretic model
C_{1i}	Material constant related to the shear modulus of rubber in the Yeoh model
D	Lateral displacement amplitude of a cycle imposed on a bearing
D_i	Material constant that introduces compressibility in Yeoh model
dx_B	Horizontal distance between two neighboring nodes at the interface of a bearing and its top support
dx_T	Horizontal distance between two neighboring nodes at the interface of a bearing and its bottom support
E_s	Young's modulus of steel
$E_{Sp,\,j}$	Plastic energy dissipation in the jth steel laminate of bearing
E_W	Work done by external forces imposed on a bearing
ESS	Equivalent shear strain imposed on a bearing (i.e., lateral displacement divided by total rubber thickness)
F	Maximum absolute horizontal force of a bearing with imperfection
F_0	Maximum absolute horizontal force of a bearing without imperfection
F_{max}	Lateral force of a bearing at +ESS
F_{min}	Lateral force of a bearing at -ESS
G	Shear modulus of rubber
G_{NEO}	Shear modulus of neoprene
G_{NR}	Shear modulus of natural rubber
$\bar{I}_1$	First modified invariant of the left Cauchy-Green deformation tensor
J_{el}	Elastic volume ratio

K_{eff}	Effective lateral stiffness of a bearing
$\overline{K}_{eff}$	Normalized lateral stiffness of a bearing (= K_{eff}/K_h)
K_{eff0}	Effective lateral stiffness of a bearing without imperfection
K_h	Nominal lateral stiffness of a bearing
K_v	Vertical stiffness of a bearing
K_{v0}	Vertical stiffness of a bearing without imperfection
L	Length (long side) of a bearing
L_p	Yielded length of a steel laminate of a bearing
$\overline{L}_p$	Plastic length ratio for a steel laminate of a bearing (= L_p/L_s)
L_s	Length of a steel laminate of a bearing
m	Effective stress exponent in the hysteretic model
r_σ	Stress-based demand-to-capacity ratio (= σ_{max}/σ_{ys})
S_{SF}	Stress scaling factor in the hysteretic model
t	Design thickness of rubber layers of a bearing
t_b	Total design thickness of an elastomeric bearing
t_c	Design thickness of side rubber cover in an elastomeric bearing
t_i	Analysis time of a run in Abaqus
t_r	Total rubber thickness of a bearing
t_s	Thickness of steel laminates in a bearing
U_X	Displacement along the global X-direction
U_Z	Displacement along the global Z-direction
W	Width (short side) of a bearing
W_D	Energy dissipated in a bearing per cycle of lateral displacement
α	Rotation imposed on a bearing about its width
$\gamma_{a,\,cy}$	Maximum interfacial shear strains caused by cyclic axial load
$\gamma_{a,\,st}$	Maximum interfacial shear strains caused by static axial load
γ_{cy}	Maximum cyclic interfacial shear strain (= $\gamma_{a,\,cy} + \gamma_{r,\,cy} + \gamma_{s,\,cy}$)
γ_{eff}	Maximum effective interfacial shear strain (= $\gamma_{st} + 1.75\gamma_{cy}$)

$\gamma_{r,\,cy}$	Maximum interfacial shear strains caused by cyclic rotation
$\gamma_{r,\,st}$	Maximum interfacial shear strains caused by static rotation
$\gamma_{s,\,cy}$	Maximum interfacial shear strains caused by cyclic shear displacement
$\gamma_{s,\,st}$	Maximum interfacial shear strains caused by static shear displacement
γ_{st}	Maximum static interfacial shear strain ($= \gamma_{a,\,st} + \gamma_{r,\,st} + \gamma_{s,\,st}$)
γ_{st+cy}	Maximum combined interfacial shear strain ($= \gamma_{st} + \gamma_{cy}$)
γ_{XY}	Twice the XY component of the Green-Lagrange strain tensor
Δ	Total vertical deflection [i.e., caused by total axial load] of a bearing
Δ_0	Total vertical deflection of a bearing without imperfections
Δ_{LL}	Live-load deflection of a bearing (mm)
$\Delta\varepsilon_{yo}$	Difference between local maxima of ε_y corresponding to the rubber layer above a steel laminate and that in rubber layer below
δ_{trv}	Cumulative slip travel of a bearing
δy	Vertical distance between a local minimum of ε_y curve on the vertical cross-sectional line on the surface of a bearing and the mid-height of steel laminate adjacent to that local minimum
ε_{max}	Maximum total principal strain ($= \varepsilon_{ys} + \varepsilon_{pl,\,max}$) in the steel laminate of a bearing
$\varepsilon_{pl,\,max}$	Maximum principal plastic strain in the steel laminate of a bearing
ε_y	In-plane strain along the y-direction on the surface of bearing
ε_{ys}	Yield strain of steel
θ	Rotational misalignment of a single steel laminate in a bearing
$\theta\theta$	Simultaneous rotation of all steel laminates of a bearing except its top and bottom ones
μ	Friction coefficient value in Coulomb model
μ_ε	Strain-based ductility ($= \varepsilon_{max}/\varepsilon_{ys}$)
v	Vertical misalignment of a single steel laminate in a bearing

v_b	Shearing velocity of a bearing
v_s	Poisson's ratio of steel
v_{NR}	Poisson's ratio of natural rubber
v_{NEO}	Poisson's ratio of Neoprene
ξ_{eff}	Effective damping ratio of a bearing
ρ	Amplitude of the half-sine curve approximating the bent shape of a single steel laminate in a bearing
$\rho\rho$	Amplitude of the half-sine curve approximating the same bent shape of all steel laminates of a bearing except its top and bottom ones
σ_{bond}	Resultant tangential contact stress, or resultant shear stress carried at the interface nodes of the steel and elastomer
σ_{max}	Maximum von Mises stress induced in the steel laminates
σ_n	Normal contact stress at steel-elastomer interface
σ_t	Resultant tangential contact stress at steel-elastomer interface (= $\sigma_t = \sqrt{\tau_{Cx}^2 + \tau_{Cz}^2}$)
σ_v	Average axial pressure imposed on a bearing
σ_{ys}	Yield stress of steel
τ_{Cx}	Tangential shear stress acting at steel-elastomer interface in the local *x* axis in the deformed configuration
τ_{Cz}	Tangential shear stress acting at steel-elastomer interface in the local *z* axis in the deformed configuration
Ω_E	Plastic-energy-based damage factor

List of Abbreviations

DIC	Digital image correlation
3D-DIC	Three-dimensional digital image correlation
DCR	Demand-to-capacity ratio
ESS	Equivalent shear strain
FE	Finite element
FEA	Finite element analysis
3D-FEA	Three-dimensional finite element analysis
HIIFP	Highway infrastructure innovation funding program
MTO	Ministry of Transportation of Ontario
NR	Natural rubber
NEO	Neoprene
PDE	Python development environment
RLC	Rubber layer cover
SLC	Steel laminate cover

1 Introduction

1.1 Elastomeric Bridge Bearings

Elastomeric bridge bearings have been used in bridges since the late 1950s (Roeder and Stanton 1991), and they are now the most widely used devices for providing vertical, rotational, and longitudinal support conditions idealized as roller or pin supports in basic structural analysis. These bearings typically consist of elastomeric layers, interleaved with steel reinforcing laminates and are surrounded by a protective elastomeric cover all around. The elastomer used in these bearings is mostly polyisoprene (natural rubber) or polychloroprene (neoprene) because of their long-term reliable performance and also their low costs. Natural rubber and neoprene consist of isoprene (C5H8) monomers and chloroprene (C4H5Cl) monomers, respectively, both of which form continuous chain molecules with structures very similar to each other. However, neoprene is more expensive and has lower flexibility under low temperatures. To improve different properties (such as flexibility, strength, and environmental resistance) of natural rubber and neoprene for engineering applications, the antidegradant and fillers such as carbon black and silica are added to them (Konstantinidis et al. 2008). In elastomeric bearings, the steel and elastomer are chemically bonded together through the vulcanization process in which the elastomer is subjected to pressure and high temperature (Stanton et al. 2008). The vulcanization process also changes the chemical structure of elastomer and makes it more flexible, strong and stable (Konstantinidis et al. 2008). Three different installation methods of elastomeric bearings can be found around the world, i.e., fully unbonded, fully bonded, and single-side bonded (as shown in Figure 1.1). In fully bonded bearings, the top and bottom sides are vulcanized to steel end plates which are then bolted or welded to the bridge supports. However, fully unbonded and single-side bonded bearings are held in place by the frictional resistance of the contact surfaces. At these interfaces, the elastomer as a soft material deforms and fill in the contacting asperities of support surfaces made up of concrete or steel (Konstantinidis et al. 2008). Although such a contact between elastomer and steel or concrete material makes the overall frictional interaction between them

different from being Coulomb friction, several studies (Han 2016; Xiang and Li 2017; Huang et al. 2018; Khaloo et al. 2020) have demonstrated that this simple friction law provides reasonable representation of the true stick or slip behavior at the bearing-support interfaces. In summary, the advantage of fully bonded bearings over the other two types of elastomeric bearings is the better control of the horizontal displacement of the bridge girder, while extensive sliding of the other two may result in partial or total unseating of the bridge girder from the supports.

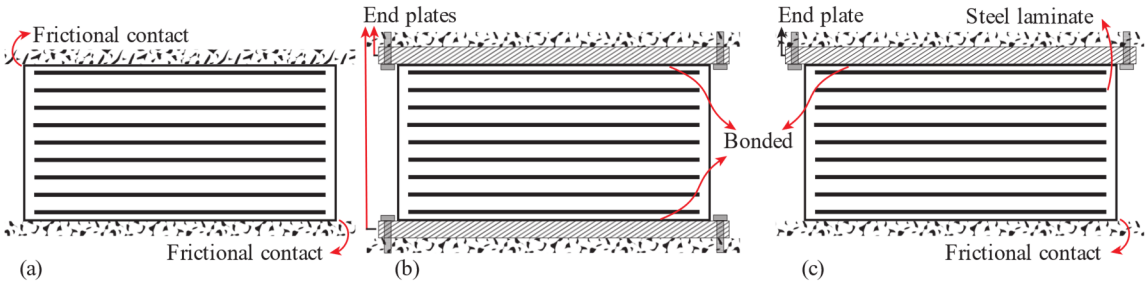

Figure 1.1 Common boundary connections for elastomeric bearings: (a) fully unbonded, (b) fully bonded, (c) single-side bonded

1.2 Purpose of Elastomeric Bridge Bearings

Elastomeric bridge bearings are cost-efficient devices from both installation and maintenance perspectives. These bearings are typically used in small to medium span bridges and are designed for a variety of service-level deformations, caused by temperature variations, gravity, traffic, concrete shrinkage, creep, and construction misalignment. The inherent shear flexibility of rubber allows the bearings to experience service-level deformations without inducing significant forces while their steel laminates limit the lateral bulging of the elastomer and thus enable the bearings to withstand large vertical loads. The lateral displacements of bearings are usually restricted to 50–70% of the total rubber thickness (AASHTO 2017; CSA 2019) with side retainers such as stiffened angle anchorages.

Although elastomeric bridge bearings are not typically intended for seismic isolation of bridges, they are inevitably subjected to dynamic loads when an earthquake occurs. In case of a strong earthquake, the displacement restrainers of bearings might fail, and bearings

might experience shear deformations much larger than expected under service-level conditions. In such scenarios, fully unbonded or single-side bonded bearings might even slide at their interfaces with supports (Xiang et al. 2021). The lateral load-displacement backbone curve of these bearings is divided into three different phases (Konstantinidis et al. 2008; Wu et al. 2018). In the first phase, pure elastic shear deformations occur in rubber, and the response is approximately linear elastic. In the second phase, as the imposed displacements is increasing, the steel laminates are flexing and corners of the bearing at top and bottom surfaces start to roll off the support surfaces, resulting in a reduction in the tangential horizontal stiffness (Konstantinidis et al. 2008). In the third phase, bearings experience obvious sliding at the bearing–support interfaces. Experimental studies (Steelman et al. 2012; Xiang and Li 2017; Xiang et al. 2018) have shown that these bearings can effectively decrease the inertia force from the bridge superstructure, provide stable hysteretic shear-sliding behavior with considerable energy dissipation capacities, and sustain vertical loads while experiencing large slip travel demands.

An innovative, pragmatic design concept, called *seismic fusing* or *quasi-isolation* has been also proposed based on the application of bridge bearing systems such as elastomeric bearings and their side restrainers to limit the force transmitted to bridge substructure under large earthquakes (Filipov et al. 2013a; Filipov et al. 2013b; Luo et al. 2017). In this concept, side retainers are intended to give way under strong seismic events, allowing fully unbonded or single-side bonded bearings to act as isolation systems by experiencing large shear deformations and sliding displacements and dissipating energy through friction sliding mechanisms (Filipov et al. 2013b). This concept stems from the Earthquake Resisting System methodology (ERS), which is currently in use by the Illinois Department of Transportation (IDOT 2012). The key characteristics of this design concept is the significantly simplified design approach of a bridge and low fabrication and installation costs of these bearings compared to the conventional seismic isolation bearings. This design concept is proposed to be used in regions with a potential for large earthquakes only at long recurrence intervals and is intended to limit damage for small seismic events and avoid span loss during a strong event.

1.3 Modes of Failure in Elastomeric Bridge Bearings

Elastomeric bridge bearings are key components of a bridge and shall not fail nor compromise the serviceability of the bridge during its lifespan. There are a number of modes in which the bearings can fail. The most common mode of failure is shear delamination, which is defined as propagated horizontal shear crack or debonding along a steel-to-elastomer interface, as shown in Figure 1.2(a,b). Shear delamination can happen under a severe, monotonic load (e.g., compression or shear), but is usually caused by cyclic loading and preceded by tension debonding of the elastomer cover from the ends of the steel laminates (Stanton et al. 2008). Shear delamination can also result in excessive vertical deflections and unpredictable horizontal reaction forces of bearings (Stanton et al. 2008). The second failure mode is yielding and then fracture of the steel laminates, as shown in Figure 1.2(c). The lateral bulging of elastomeric layers in bearings under compression induces tension in the steel laminates which can potentially lead to their fracture. However, this failure mode is less frequent since the fracture loads can be up to 10 times larger than the design loads (Stanton et al. 2008). Similar to the shear delamination, fracture of steel laminates can result in a substantial reduction of the vertical stiffness due to the loss of their effectiveness in constraining the lateral bugling of rubber layers. The reduction of vertical stiffness and excessive vertical deflection of bearings can increase the impact loading from traffic, damage deck joints and seals (Roeder et al. 1989), and cause differential deflection of the superstructure and excessive stresses in girders (Yura et al. 2001). Buckling (see Figure 1.2(d,e)) is the third mode of failure which can occur in thick bearings subjected to compression (Schapery and Skala 1976) or both compression and shear (Belivanis 2017). Although elastomeric bearings are not slender devices in general, their buckling can be a concern because of their high shear flexibility (Stanton et al. 2008).

In a fully bonded bearing subjected to a light axial load and large rotation (Figure 1.2(e)), local tension stress close to the hydrostatic state is induced in the elastomer on the tension side which might lead to the sudden, brittle, internal rupture of the elastomer (Stanton et

al. 2008). This fourth mode of failure is usually referred to as *uplift* and is most likely to happen when slender steel girders are first set during the construction of the bridge superstructure. In such a scenario, the axial loads on bearings are limited to the girder self-weight, and large rotations up to about 0.04 radians might be applied on them due to thermal camber (Stanton et al. 2008). As the fifth mode of failure, in fully bonded bearings, the tearing of rubber (Figure 1.2(f)) can happen under strong earthquakes. In this case, the bearing is separated into two parts, and the superstructure can fall off the support, observed during the 2011 Great East Japan earthquake (Kawashima 2012). Finally, unseating of a fully unbonded bearing (Figure 1.2(g)) might also happen when a strong earthquake happens. In such a scenario, the lateral force overcomes the frictional resistance of contact surfaces, and the accumulated slippages of the bearings eventually lead to this failure mode (Xiang and Li 2017).

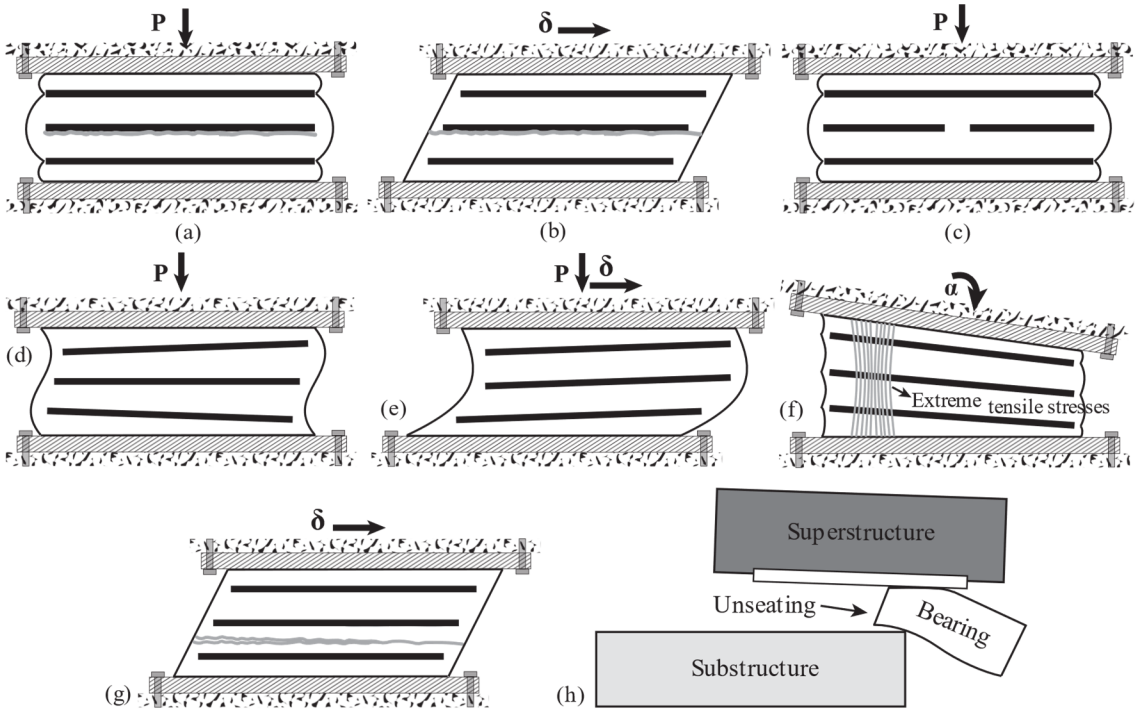

Figure 1.2 Failure modes in elastomeric bearings: (a,b) shear delamination; (c) fracture of a steel laminate; (d,e) buckling; (f) uplift; (g) rubber tearing; (h) unseating

1.4 Design of Elastomeric Bridge Bearings

To prevent the failure modes mentioned above and ensure satisfactory long-term performance of elastomeric bearings, bridge codes (ECS 2005; AASHTO 2017; CSA 2019) specify different design provisions on the load and displacement demands, aspect ratio, stability, and serviceability requirements (e.g., slippage and deflection). For instance, because of stability concerns, the axial load demand on bearings is limited to half the buckling loads (AASHTO 2017; CSA 2019). Also, to prevent yielding and fatigue failure of steel laminates, AASHTO (2017) specifies constraints on their minimum thickness based on the axial load demands on the bearings. Moreover, bridge codes (AASHTO 2017; CSA 2019) prevent the brittle rupture of rubber caused by the uplift of fully bonded bearings by limiting the peak hydrostatic tension demand on the rubber under all critical loading combinations. Most importantly, bridge codes (AASHTO 2017; CSA 2019) specify a total shear strain design approach according to which the explicit summation of shear strains induced at the steel–rubber interfaces by static and cyclic loads, with the latter multiplied by the amplification factor of 1.7, should be limited to 5. This design approach is based on the fact that compression, rotation, and shear loadings all cause the peak shear strains at the same location within the rubber layer, i.e., at the edge of the steel laminate (Gent and Meinecke 1970), as shown in Figure 1.3. It is noted that the specified shear strain limit of 5 is an empirical limit according to the experimental tests conducted by Stanton et al. (2008) to avoid shear delamination in bearings.

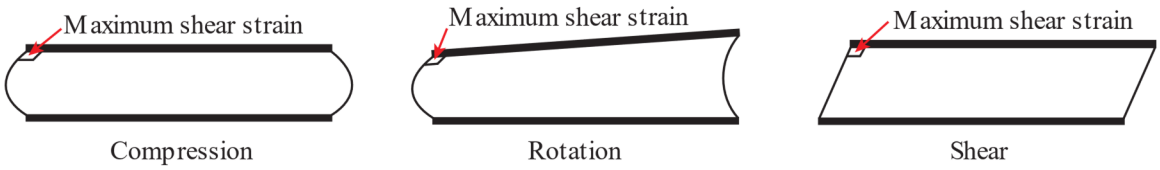

Figure 1.3 Deformations of a laminated elastomeric bearing layer and the peak shear strains caused by compression, rotation, and shear

1.5 Manufacturing Imperfections and Design Tolerances

Elastomeric bridge bearings are expected to have a satisfactory long-term performance if they are well-designed and well-manufactured. However, the manufacturing process of elastomeric bridge bearings is not always flawless. During the manufacturing process, heat and pressure are applied from outside the bearing mold to vulcanize the rubber, activate the adhesive, and make rubber form the mold. However, inward pressure and heat penetration do not usually take place uniformly in different directions, which can cause undesirable flow of rubber inside the mold and uneven rubber curing (Roeder and Stanton 1997). This may finally lead to different forms of internal imperfections such as horizontal, vertical, and rotational misalignments as well as bending of the steel laminates in the finished bearing. Laminate misalignments might also happen due to the malfunction of seats when used by the manufacturer for maintaining accurate laminate placement during the manufacturing process (Kumar 2001).

Bridge specifications in North America specify various design tolerances for the geometrical dimensions of the elastomeric bridge bearings. For instance, Table 1.1 shows the tolerance limits specified by OPSS (2017) and AASHTO (2018) for the design thickness of each rubber layer (denoted as t), design thickness of rubber cover (denoted as t_c), and design thickness of bearing (denoted as t_b). OPSS (2017) also specifies a tolerance limit of 25% for the overall non-parallelism of steel laminates. AASHTO (2018) also requires that if the exact thickness of each rubber layer at any point within the bearing differs from t (mm) by more than 3 mm, the vertical misalignment and rotational misalignment of associated laminates (denoted as v (mm) and θ (radians), respectively) should meet $\theta + {}^{v}\!/_{t} \leq 0.35$ (provided that $\theta \leq 0.02$ radians). This interaction equation, proposed by Kumar (2001) is aimed at limiting specific performance variables such as principal strain in the rubber, von Mises stress in steel laminates, and percentage changes in the vertical and lateral stiffness of bearings.

Table 1.1 Some design tolerances specified in bridge codes for elastomeric bridge bearings

Parameter	Acceptable tolerances	
	AASHTO (2018)	OPSS (2017)
t	±3 mm	$\pm 0.2t$
t_c	–0, +3 mm	N/A
t_b	–0, +3 mm (if $t_b \leq 32$ mm) –0, +6 mm (if $t_b > 32$ mm)	–0, +3 mm (if $t_b \leq 40$ mm) –0, +6 mm (if $t_b > 40$ mm)

1.6 Motivation

Currently, transportation ministries and departments such as the Ministry of Transportation of Ontario conduct destructive quality control testing of sample bearings per lot of received bearings from the manufacturer (i.e., usually they test one bearing per 10 received) with respect to the design tolerances. This involves cutting the sample bearings to measure their exact internal geometrical properties, which makes the sample bearings unusable. Also, because of its destructive nature, the test is usually conducted on only two bearings as the sample bearings, and the whole lot is rejected at the manufacturing stage when the sample bearings fail to comply with the design tolerance (OPSS 2017; AASHTO 2018). Given these limitations, an efficient nondestructive assessment methodology is needed for routine quality control testing of manufactured elastomeric bridge bearings. In this regard, a vision-based measurement technique called Digital Image Correlation (DIC) seems to be a powerful and accessible technique for developing the assessment methodology needed for bearings. DIC is based on digital image processing and numerical computing, which is introduced in more details in the following section.

The effects of manufacturing imperfections on the performance of bearings under service-level conditions and under seismic actions (or lateral displacements expected under seismic actions) have received very limited attention and no attention, respectively. Also, the logic behind all the aforementioned design tolerances is either not clear or questionable. For example, the interaction equation developed by Kumar (2001) is based on the results of a finite element study on the effects of only misaligned steel laminates in a specific bonded bearing. Kumar (2001) also examined the bearings under service-level load demands less

than what is permitted according to current bridge codes (e.g., AASHTO (2017)). Therefore, it is not clear whether the current design tolerances can appropriately prevent poor performance or failure of the bearings. For instance, the shear delamination and yielding of steel laminates might be accelerated or exacerbated due to the imperfections. Also, the bearing's mechanical behavior (e.g., vertical, rotational, and horizontal stiffnesses) might be adversely affected by the imperfections because of their high sensitivity to geometrical aspects (Konstantinidis et al. 2008; Kelly and Konstantinidis 2011). The total shear strain design approach specified in bridge codes (e.g., AASHTO's (2017) design Method B) allows relatively large load and displacement demands under which the potentially detrimental effects of imperfections including the misaligned and bent steel laminates need to be assessed. Similar to their effects on the service-level performance, imperfections might also trigger poor performance and failure of bearings subjected to lateral displacements beyond their service level. For instance, imperfections might change the behavioral characteristics of fully unbonded bearings such as shearing and sliding patterns, effective lateral stiffness, and effective damping ratio. Lateral performance of fully unbonded bearings is associated with roll-off which can be substantially affected by the imperfections. Additionally, the potential plastic damage in the steel laminates of bearings subjected to large cyclic lateral displacement might worsen because of the imperfections. In this context, thickness properties of steel laminates seem to be also an important factor. All in all, it is needed to investigate the potential effects of manufacturing imperfections on the performance of bearings subjected to different loading and displacement scenarios including the maximum service loading and large cyclic lateral displacements expected under relatively strong earthquakes.

1.7 Digital Image Correlation and Its Application

DIC is a measurement technique that provides displacements and strains on the surface of a deforming or moving object by comparing digital images of its undeformed state and its deformed or displaced state. DIC was first introduced by Peters and Ranson (Peters and Ranson 1982) and was first implemented for experimental stress analysis at the University

of South Carolina in the 1980s while image processing was still in its early stages of growth (Pan et al. 2009). DIC can be implemented with a single camera (typically denoted as 2D-DIC) or with a calibrated stereo-camera system consisting of two cameras (typically denoted as 3D-DIC). The limitation of 2D-DIC with a single camera is that it works well when the relative out-of-plane motion of the object surface with respect to the camera lens is almost zero. When a single camera is used to obtain object deformations, the relative out-of-plane motion of the object surface introduces pseudo image-plane displacement gradients. These pseudo displacement gradients affect the real in-plane displacement and strain measurements (Sutton et al. 2009). However, 3D-DIC integrates the principles of DIC and stereovision and can provide the full spatial field of surface displacements and strains. In 3D-DIC, the three-dimensional positions are determined before and after experiencing out-of-plane motions, and the measured in-plane motions and strains are not corrupted by the out-of-plane motion (Sutton et al. 2009).

DIC (including both 2D-DIC and 3D-DIC) has been established as a powerful and precise tool for a broad area of applications, including the investigation of the deformation characteristics of materials (Ivanov et al. 2009; Van Paepegem et al. 2009; Srikar et al. 2016), the identification of the mechanical behavior of materials (Cooreman et al. 2007; Cooreman et al. 2008), and the health monitoring and damage detection of structures (Sas et al. 2012). DIC applications on steel and concrete beams have demonstrated its capability in monitoring the deflections, surface stains, curvatures, and flexural crack growth (Lecompte et al. 2006; Destrebecq et al. 2011; Dutton et al. 2013; De Wilder et al. 2016). Load-resistance mechanisms and damage evolution in masonry walls subjected to horizontal in-plane loads have been successfully monitored using the DIC technique (Salmanpour and Mojsilovic 2013; Ghorbani et al. 2015). DIC has been successful in tracking the evolution of surface strain fields over the entire plate of different gusset plate connections as they approach failure (Iadicola 2012). Using the DIC technique, full profiles of curvature, shear deformations, rotation, and plasticity spread were successfully distinguished in concrete columns subjected to reversed cyclic loading (Sokoli et al. 2014). DIC has been also found to be a versatile tool for validating the finite element models of

structural components (e.g., profiled steel sheets (Piekarczuk et al. 2015)). Given the observed versatility of DIC in many engineering applications, DIC seems to be useful for also the condition assessment or monitoring of elastomeric bridge bearings.

1.8 Objectives and Methods

The overarching goal of the research was to physically identify and characterize the geometry of potential manufacturing imperfections in elastomeric bridge bearings and to investigate the effects of these imperfections on the behavior of the bearings under service and extreme demands. The research was divided into three phases with the following primary objectives:

- Develop a nondestructive assessment methodology for efficiently inferring the geometrical aspects of elastomeric bearings, including the thickness of the rubber layers and side covers and the intensity of potential imperfections, such as vertically misaligned, rotationally misaligned, and bent steel laminates.
- Investigate how imperfections in elastomeric bearings affect their service-level performance by assessing various performance variables, including shear strain in the rubber, bond stress at steel–rubber interfaces, intensity and extent of plastic deformations in the steel laminates, and vertical deflection of the bearings under maximum service loading.
- Investigate how imperfections in fully unbonded bearings and thickness properties of their steel laminates affect performance variables, including roll-off amount, sliding displacement, effective lateral stiffness, effective damping ratio, and intensity and extent of plastic deformations in the steel laminates under large cyclic lateral displacements.

This research involved both experimental and analytical studies. To achieve the first objective, 3D finite element analyses (FEA) were conducted on models of elastomeric bearings, and 3D-DIC was used in an experimental study involving compression tests on two fully unbonded rectangular bearings. In this regard, 3D-DIC was implemented instead of 2D-DIC to avoid pseudo-displacement gradient measurements occurring in 2D-DIC due

to the out-of-plane motion of the compressed bearings. To achieve the second and third objectives, two series of 3D FEA studies were conducted on different elastomeric bearings. In this regard, a python script was developed using the Abaqus Python Development Environment to efficiently develop large numbers of 3D finite element models of bearings in the software Abaqus (Dassault Systemes 2019).

1.9 Organization of the Thesis

This thesis was prepared in accordance with the regulations of a "sandwich" thesis format. Chapter 2, Chapter 3, and Chapter 4 were prepared to become stand-alone journal papers, and thus each chapter has its own introduction, conclusion, and references. Therefore, some overlap exists between chapters, mainly among the introductory parts of them.

Chapter 2 (i.e., Journal Paper #1) develops a nondestructive, vision-based methodology for inferring the internal structure of elastomeric bridge bearings including the thickness of rubber layers and side cover. The developed methodology requires 3D-DIC of the bulging patterns forming on the vertical sides of bearings under compression. Initially, 3D FEAs were conducted on several bearings with and without imperfections to develop the methodology, and it was then evaluated in 3D-DIC of two bearings during compression testing. The developed methodology can ease transportation departments to efficiently assess whether the bearings delivered by the manufacturers meet the design specifications.

Following the identification and quantification of manufacturing imperfections in elastomeric bridge bearings in Chapter 2, Chapter 3 (i.e., Journal Paper #2) conducts a numerical study to assess the effects of such imperfections including vertically misaligned, rotationally misaligned, and bent steel laminates on the service-level performance of elastomeric bearings. 3D FEAs were conducted on 97 models of bearings with different characteristics in terms of shape factor, steel laminate thickness, elastomer material properties, bond condition at bearing–support interfaces, and imperfection configurations. The study was focused on five different aspects of the performance of the bearings subjected to maximum service loading chosen according to the total shear strain design approach in bridge specifications. The examined performance aspects include shear strains

induced in the elastomer, tensile stresses in the steel laminates, bond stresses at steel–elastomer interfaces, and vertical deflection and stiffness of bearings.

Following the numerical study in Chapter 3 regarding the effects of manufacturing imperfections in bearings under service-level loading conditions, Chapter 4 (i.e., Journal Paper #3) performs another numerical study to assess the effects of imperfections including rotationally misaligned and bent laminates and their thickness properties on the performance of fully unbonded bearings subjected to lateral displacements beyond their service level. 3D FEAs were conducted on 27 models of bearings with different characteristics in terms of plan dimensions, slenderness, shape factor, laminate thickness, and imperfection configuration. Examined bearings were subjected to compressive loads followed by 5 cycles of lateral displacements with increasing amplitude, up to 200% of their total rubber thickness. Initially, the deformation and displacement patterns of bearings were studied. Then, hysteretic responses of the bearings were evaluated in terms of their effective horizontal stiffness and equivalent damping ratio. Finally, the potential plastic damage in the steel laminates of examined bearings was assessed in terms of maximum induced von mises stress, maximum principal plastic strain, yielded area, and dissipated plastic energy.

Chapter 5 concludes the thesis. It summarizes the important findings and provides recommendations for future research.

References

AASHTO. (American Association of State Highway and Transportation Officials). 2017. *AASHTO LRFD bridge design specifications*. Washington, DC: AASHTO.

AASHTO. (American Association of State Highway and Transportation Officials). 2018. *Standard specification for plain and laminated elastomeric bridge bearings*. Washington, DC.

Belivanis, K. V. 2017. "Expanding the use of elastomeric bearings for higher demand applications." Ph.D. thesis, Dept. of Civil, Architectural and Environmental Engineering, The Univ. of Texas at Austin.

Cooreman, S., D. Lecompte, H. Sol, J. Vantomme, and D. Debruyne. 2007. "Elasto-plastic material parameter identification by inverse methods: Calculation of the sensitivity

matrix." *Int. J. Solids. Struct.*, 44 (13), 4329-4341. https://doi.org/10.1016/j.ijsolstr.2006.11.024.

Cooreman, S., D. Lecompte, H. Sol, J. Vantomme, and D. Debruyne. 2008. "Identification of mechanical material behavior through inverse modeling and DIC." *Exp. Mech.*, 48 (4), 421-433. https://doi.org/10.1007/s11340-007-9094-0.

CSA. (Canadian Standards Association). 2019. *S6-19 Canadian highway bridge design code*. Section 11: Joints and Bearings. Toronto, Ontario.

Dassault Systemes. 2019. "ABAQUS 2019 Theory manual." *Dassault Systemes Simulia Corp., Providence, Rhode Island*.

De Wilder, K., G. De Roeck, and L. Vandewalle. 2016. "The use of advanced optical measurement methods for the mechanical analysis of shear deficient prestressed concrete members." *Int. J. Concr. Struct. Mater.*, 10 (2), 189-203. https://doi.org/10.1007/s40069-016-0135-x.

Destrebecq, J.-F., E. Toussaint, and E. Ferrier. 2011. "Analysis of cracks and deformations in a full scale reinforced concrete beam using a digital image correlation technique." *Exp. Mech.*, 51 (6), 879-890. https://doi.org/10.1007/s11340-010-9384-9.

Dutton, M., W. A. Take, and N. A. Hoult. 2013. "Curvature monitoring of beams using digital image correlation." *J. Bridge Eng.*, 19 (3), 1-13. https://doi.org/10.1061/(ASCE)BE.1943-5592.0000538.

ECS. (European Commission for Standardization). 2005. *Structural Bearings-Part 3: Elastomeric Bearings*. Brussels, Belgium.

Filipov, E. T., L. A. Fahnestock, J. S. Steelman, J. F. Hajjar, J. M. LaFave, and D. A. Foutch. 2013a. "Evaluation of quasi-isolated seismic bridge behavior using nonlinear bearing models." *Eng. Struct.*, 49, 168-181. http://dx.doi.org/10.1016/j.engstruct.2012.10.011.

Filipov, E. T., J. R. Revell, L. A. Fahnestock, J. M. LaFave, J. F. Hajjar, D. A. Foutch, and J. S. Steelman. 2013b. "Seismic performance of highway bridges with fusing bearing components for quasi-isolation." *Earthq. Eng. Struct. Dyn.*, 42 (9), 1375-1394. https://doi.org/10.1002/eqe.2277.

Gent, A., and E. Meinecke. 1970. "Compression, bending, and shear of bonded rubber blocks." *Polym. Eng. Sci.*, 10 (1), 48-53. https://doi.org/10.1002/pen.760100110.

Ghorbani, R., F. Matta, and M. A. Sutton. 2015. "Full-field deformation measurement and crack mapping on confined masonry walls using digital image correlation." *Exp. Mech.*, 55 (1), 227-243. https://doi.org/10.1007/s11340-014-9906-y.

Han, L. 2016. "Elastomeric bearings in high demand applications: Numerical study and experimental Validation." Ph.D. thesis, Dept. of Civil, Architectural and Environmental Engineering, The Univ. of Texas at Austin.

Huang, W., X. Xu, K. Wang, and W. Liu. 2018. "Numerical Simulation of Steel-Laminated Bearing Considering Friction Slipping." *International Journal of Engineering and Technology*, 10 (2). https://doi.org/10.7763/IJET.2018.V10.1052.

Iadicola, M. A. 2012. *Digital image correlation measurements during gusset plate connection testing to structural failure*. *Report NIST Technical Note 1752*, National Institute of Standards and Technology (NIST), U.S. Department of Commerce.

IDOT. (Illinois Department of Transportation). 2012. *IDOT Bridge Manual*. Springfield, IL.

Ivanov, D., S. Ivanov, S. Lomov, and I. Verpoest. 2009. "Strain mapping analysis of textile composites." *Opt. Lasers Eng.*, 47 (3-4), 360-370. http://dx.doi.org/10.1016/j.optlaseng.2008.05.013.

Kawashima, K. 2012. "Damage of bridges due to the 2011 Great East Japan Earthquake." *J. Jpn. Assoc. Earthq. Eng.*, 12 (4), 4_319-314_338. https://doi.org/10.5610/JAEE.12.4_319.

Kelly, J. M., and D. Konstantinidis. 2011. *Mechanics of rubber bearings for seismic and vibration isolation*. Chichester, UK: John Wiley & Sons.

Khaloo, A., A. Maghsoudi-Barmi, and M. E. Moeini. 2020. "Numerical parametric investigation of hysteretic behavior of steel-reinforced elastomeric bearings under large shear deformation." *Structures*, 26, 456-470. https://doi.org/10.1016/j.istruc.2020.04.029.

Konstantinidis, D., J. M. Kelly, and N. Makris. 2008. *Experimental investigation on the seismic response of bridge bearings*. *Report EERC-2008/02*, Earthquake Engineering Research Center, University of California, Berkeley.

Kumar, A. 2001. "Performance related parameters of elastomeric bearings." Ph.D. Dissertation, Dept. of Civil, Architectural and Environmental Engineering, The Univ. of Texas at Austin.

Lecompte, D., J. Vantomme, and H. Sol. 2006. "Crack detection in a concrete beam using two different camera techniques." *Struct. Health Monit.*, 5 (1), 59-68. https://doi.org/10.1177%2F1475921706057982.

Luo, J., L. A. Fahnestock, D. L. Kozak, and J. M. LaFave. 2017. "Seismic analysis incorporating detailed structure–abutment–foundation interaction for quasi-isolated highway bridges." *Struct. Infrastruct. Eng.*, 13 (5), 581-603. https://doi.org/10.1080/15732479.2016.1177094.

OPSS. (Ontario Provincial Standard Specification). 2017. *Material specification for bearings - elastomeric plain and steel laminated*.

Pan, B., A. Asundi, H. Xie, and J. Gao. 2009. "Digital image correlation using iterative least squares and pointwise least squares for displacement field and strain field measurements." *Opt. Lasers Eng.*, 47 (7-8), 865-874. http://dx.doi.org/10.1016/j.optlaseng.2008.10.014.

Peters, W., and W. Ranson. 1982. "Digital imaging techniques in experimental stress analysis." *Opt. Eng.*, 21 (3), 213427. https://doi.org/10.1117/12.7972925.

Piekarczuk, A., K. Malowany, P. Więch, M. Kujawińska, and P. Sulik. 2015. "Stability and bearing capacity of arch-shaped corrugated shell elements: experimental and numerical study." *B. Pol. Acad. Sci-Tech.*, 63 (1), 113-123. https://doi.org/10.1515/bpasts-2015-0013.

Roeder, C., and J. Stanton. 1997. "Steel Bridge Bearing Selection and Design Guide American Iron and Steel Institute." *Highway Structures Design Handbook*, 2.

Roeder, C. W., and J. F. Stanton. 1991. "State-of-the-art elastomeric bridge bearing design." *ACI Struct. J.*, 88 (1), 31-41. https://doi.org/10.14359/3086.

Roeder, C. W., J. F. Stanton, and T. Feller. 1989. *Low temperature behavior and acceptance criteria for elastomeric bridge bearings*. Washington, DC: Transportation Research Board.

Salmanpour, A., and N. Mojsilovic. "Application of Digital Image Correlation for strain measurements of large masonry walls." In *Proc., APCOM & ISCM,* Singapore.

Sas, G., T. Blanksvärd, O. Enochsson, B. Täljsten, and L. Elfgren. 2012. "Photographic strain monitoring during full-scale failure testing of Örnsköldsvik bridge." *Struct. Health Monit.*, 11 (4), 489-498. https://doi.org/10.1177/1475921712438568.

Schapery, R., and D. Skala. 1976. "Elastic stability of laminated elastomeric columns." *Int. J. Solids. Struct.*, 12 (6), 401-417.

Sokoli, D., W. Shekarchi, E. Buenrostro, and W. M. Ghannoum. 2014. "Advancing behavioral understanding and damage evaluation of concrete members using high-resolution digital image correlation data." *Earthquakes Struct.*, 7 (5), 609-626. http://dx.doi.org/10.12989/eas.2014.7.5.609.

Srikar, G., G. Anand, and S. S. Prakash. 2016. "A study on residual compression behavior of structural fiber reinforced concrete exposed to moderate temperature using digital image correlation." *Int. J. Concr. Struct. Mater.*, 10 (1), 75-85. https://doi.org/10.1007/s40069-016-0127-x.

Stanton, J. F., C. W. Roeder, P. Mackenzie-Helnwein, C. White, C. Kuester, and B. Craig. 2008. *Rotation limits for elastomeric bearings*. *Report 596*, National Cooperative Highway Research Program (NCHRP), Washington, DC: Transportation Research Board.

Steelman, J. S., L. A. Fahnestock, E. T. Filipov, J. M. LaFave, J. F. Hajjar, and D. A. Foutch. 2012. "Shear and friction response of nonseismic laminated elastomeric bridge bearings subject to seismic demands." *J. Bridge Eng.*, 18 (7), 612-623. http://dx.doi.org/10.1061/(ASCE)BE.1943-5592.0000406.

Sutton, M. A., H. Schreier, and J.-J. Orteu. 2009. *Image correlation for shape, motion and deformation measurements*. New York, US: Springer.

Van Paepegem, W., A. A. Shulev, I. R. Roussev, S. De Pauw, J. Degrieck, and V. C. Sainov. 2009. "Study of the deformation characteristics of window security film by digital image correlation techniques." *Opt. Lasers Eng.*, 47 (3-4), 390-397. https://doi.org/10.1016/j.optlaseng.2008.03.005.

Wu, G., K. Wang, G. Lu, and P. Zhang. 2018. "An Experimental Investigation of Unbonded Laminated Elastomeric Bearings and the Seismic Evaluations of Highway Bridges with Tested Bearing Components." *Shock and Vibration*, 2018. https://doi.org/10.1155/2018/8439321.

Xiang, N., M. S. Alam, and J. Li. 2018. "Shake table studies of a highway bridge model by allowing the sliding of laminated-rubber bearings with and without restraining

devices." *Eng. Struct.*, 171, 583-601. https://doi.org/10.1016/j.engstruct.2018.05.121.

Xiang, N., Y. Goto, M. S. Alam, and J. Li. 2021. "Effect of bonding or unbonding on seismic behavior of bridge elastomeric bearings: lessons learned from past earthquakes in China and Japan and inspirations for future design." *Advances in Bridge Engineering*, 2 (1), 1-17. https://doi.org/10.1186/s43251-021-00036-9.

Xiang, N., and J. Li. 2017. "Experimental and numerical study on seismic sliding mechanism of laminated-rubber bearings." *Eng. Struct.*, 141, 159-174. http://dx.doi.org/10.1016/j.engstruct.2017.03.032.

Yura, J., A. Kumar, A. Yakut, C. Topkaya, E. Becker, and J. Collingwood. 2001. *Elastomeric bridge bearings: Recommended test methods*. *Report NCHRP 449*, National Cooperative Highway Research Program (NCHRP), Washington, DC: Transportation Research Board.

2 Nondestructive Assessment of Elastomeric Bridge Bearings Using 3D Digital Image Correlation

Soleimani S.A., Konstantinidis D., and Balomenos G.P. (2022). Nondestructive Assessment of Elastomeric Bridge Bearings Using 3D Digital Image Correlation. *Journal of Structural Engineering*, Vol. 148, Issue 1: 04021233, DOI: 10.1061/(ASCE)ST.1943-541X.0003200.

Abstract

Elastomeric bridge bearings are installed between the bridge superstructure and substructure to accommodate translational and rotational deformations. The manufacturing quality of elastomeric bridge bearings is of high significance because manufacturing defects (such as variations in rubber layer thickness and nonparallel steel laminates) may jeopardize their short- and long-term structural behavior and integrity. Current quality control procedures involve destructive testing of samples of bearings from a lot. This type of testing is time consuming and costly, and thus limited to a relatively small sample size, which may undermine confidence in the quality of remaining bearings in the lot. This paper presents an alternative, vision-based assessment methodology for the nondestructive identification of the internal structure of elastomeric bridge bearings. The methodology capitalizes on the high deformability of rubber and the near inextensibility of the steel laminates, which together result in a unique deformation pattern on the vertical surfaces of a bearing when it is subjected to axial load. This deformation pattern features local extrema in in-plane strain and horizontal displacement fields on the vertical surfaces. These local extrema are analyzed to deduce the thicknesses of the rubber layers and rubber side covers. The methodology is developed based on three-dimensional finite element analyses (3D-FEA). Then, three-dimensional digital image correlation (3D-DIC) is used in experimental tests to evaluate its capability to identify manufacturing defects in elastomeric bridge bearings. Finally, the methodology is validated against destructive tests. The nondestructive method presented in this study is conducted in conjunction with

compressive tests that departments of transportation carry out routinely and is therefore expected to facilitate rapid and cost-effective qualification of elastomeric bridge bearings.

Key words: Elastomeric Bridge Bearings, Vision-Based Assessment, 3D Digital Image Correlation, Quality Control, Experimental Testing, Finite Element Analysis

2.1 Introduction

Steel-laminated elastomeric bearings are used widely in bridge applications to accommodate translations and rotations due to temperature variations, traffic loading, shrinkage, creep, and construction misalignments. A high manufacturing quality is important to ensure that bearings perform well. However, during the vulcanization process, unavoidable flow of rubber inside the mold due to high pressure and nonuniform heating in different directions may cause different forms of internal defects, such as horizontal, vertical, and rotational misalignments, as well as bending of the steel laminates (Yura et al. 2001; Belivanis 2017), as illustrated in Figure 2.1. Laminate misalignments might also happen due to malfunction of seats used for maintaining accurate laminate placement during the vulcanization process (Belivanis 2017).

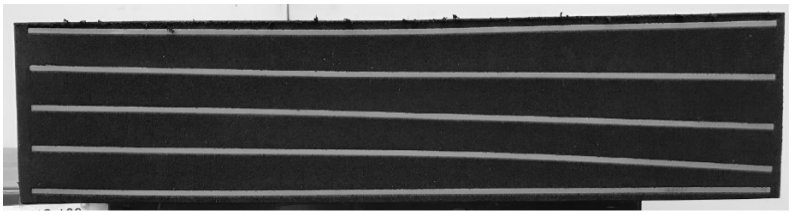

Figure 2.1 Photograph of cut elastomeric bridge bearing with manufacturing defects

Manufacturing imperfections like these can adversely affect the mechanical properties of elastomeric bearings, which are sensitive to their geometric characteristics (Konstantinidis et al. 2008; Kelly and Konstantinidis 2011). For instance, Yura et al. (2001) and Belivanis (2017) observed that the vertical and bending stiffnesses of elastomeric bearings can be sensitive to vertical misalignments and bending of the steel laminates. Excessive deflection at supports can cause uneven road surface in single-span bridges and excessive stress in girders of multi-span bridges (Yura et al. 2001). Limiting the vertical deflection of the

bearing is also important for preventing damage to expansion joints and controlling the impact loading arising from traffic across a stepped road surface at these joints (Roeder et al. 1989). In addition, internal defects, such as variations in the thickness of the rubber layers, can also affect the long-term performance of the bearings. For instance, shear delamination (i.e., propagated horizontal shear cracks along steel–elastomer interfaces) can be accelerated by these internal defects (Yura et al. 2001). Yura et al. (2001) showed that the laminate misalignment may affect the distribution of strains and stresses in the bearing and amplify their maxima at critical locations. Also, the outward expansion of the rubber layers due to initial imperfections may cause increased shear stresses in the laminates, resulting in local yielding (Yura et al. 2001).

To ensure adequate long-term performance, bridge specifications in North America (e.g., OPSS 2017, AASHTO 2018) include design tolerances for both the external and internal dimensions of elastomeric bridge bearings. Before acceptance of elastomeric bridge bearings from the manufacturer, departments/ministries of transportation cut sample bearings to certify that these tolerances are met. However, this current quality control procedure is destructive in nature, making the sample bearings unusable. Because of this, only a limited number of sample bearings from a lot is tested; e.g., according to AASHTO (2018), one full-size bearing per every ten per lot, or a minimum of two bearings. Given these limitations, there is a need to develop a measurement technique that can enable routine, rapid, nondestructive assessment of elastomeric bridge bearings.

Various nondestructive techniques exist for health monitoring at a local or global scale. Common local-scale techniques include acoustic emission, different forms of interferometry, X-ray computerized tomography, and shearography (Doyle 2004; Grediac 2004; Mayinger 2013). Most of these techniques are complex, labor-intensive, and costly to implement, and they require attaching contact sensors to the structure. A noncontact alternative for health monitoring at a local level is digital image correlation (DIC). Three-dimensional digital image correlation (3D-DIC) integrates DIC and stereovision, and it is a promising technique because of its simple implementation, high accuracy, and full-field

nature (Sutton et al. 1983; Sutton et al. 2009; McGinnis et al. 2012). 3D-DIC provides the full spatial fields of surface displacements and strains by comparing stereo digital images of the initial and final configuration of the object surface. This vision-based measurement approach has been extensively validated using contact sensors (Dutton et al. 2013; Ghorbani et al. 2015).

In recent years, DIC has been used to inspect and monitor various types of structural components, including reinforced concrete beams and columns (Dutton et al. 2013; Sokoli et al. 2014; De Wilder et al. 2016), timber-framed structures (Sieffert et al. 2016), masonry walls (Ghorbani et al. 2015; Bolhassani et al. 2016; Mojsilović and Salmanpour 2016), and full-scale gusset plate connections (Iadicola 2012). Such applications have been made feasible due to advancements in high-resolution digital cameras and computing. To the best of the authors' knowledge, DIC has not been used in applications involving bridge or seismic isolation bearings.

This paper presents a nondestructive, vision-based methodology for inferring the internal structure of elastomeric bridge bearings. The methodology is based on 3D-DIC of the bulging patterns that form on the vertical surfaces of compressed elastomeric bearings due to the stark difference between the deformability of rubber and steel. Initially, 3D finite element analyses (FEA) are conducted on elastomeric bearings to develop an accurate technique for pinpointing the mid-height locations of the steel laminates. Knowing the thickness of the steel laminates (specified in the design) then allows the determination of the thicknesses of the rubber layers. Finally, the side covers are determined. The developed technique is used to support 3D-DIC of elastomeric bridge bearings in an experimental investigation aimed at evaluating the proposed methodology. It is pointed out that FEA was used for the development of the methodology but is not needed for its application. Finally, to validate the methodology, two bearings are physically cut, and their actual internal structures are compared against the vision-based inferred internal structures. The methodology presented in this study provides a promising, reliable, and efficient way to assess whether manufactured elastomeric bridge bearings meet their design specifications.

2.2 Inferring the Internal Structure of a Laminated Elastomeric Bearing from Deformation Measurements on Its Surface

The precise locations of the steel laminates are not known in a manufactured elastomeric bridge bearing because a thin protective rubber cover conceals them. However, when a vertical load is applied to the bearing, the rubber layers budge out prominently because of the rubber's high deformability; whereas the steel laminates, which are nearly inextensible along their plane (Osgooei et al. 2014), restrain this bulging. This results in a ribbed pattern forming on the vertical surfaces of the bearing (Ahmadi Soleimani et al. 2020), which can be exploited to identify the locations of the steel laminates, infer the thicknesses of the rubber layers, and approximately quantify the thickness of side covers.

The methodology involves conducting a compression test on a laminated elastomeric bearing under sufficient load to produce the aforementioned ribbed deformation pattern on the vertical surfaces of the bearing. During the test, images of the deformation pattern are captured by two calibrated digital cameras (stereoscopy). A stereoscopic approach is required because the deformation is predominantly in the direction normal to the imaged vertical surface. The images are then processed using 3D-DIC to map strain fields on the bearing's vertical surfaces. Specific features of the strain fields are used to identify the mid-height locations of steel laminates. Once the laminates are mapped, the thicknesses of the rubber layers are deduced. Also, a specific feature of displacement fields is used to deduce the thickness of the side covers.

To determine what specific features of the measured displacement and strain fields on the bearing's surface most accurately identify for positions of the steel laminates, 3D FEA were conducted on different elastomeric bridge bearings using Abaqus (Dassault Systemes 2019). The next two sections present details of the FEA approach and the determination of the vertical positions of the steel laminates, respectively.

2.2.1 Finite Element Analysis of Elastomeric Bridge Bearings

Seven finite element models were considered with different characteristics in terms of bearing geometry, rubber properties, and contact interactions at the top and bottom interfaces. The characteristics of the seven finite element models are listed in Table 2.1. The label for each model is comprised of three parts: the first two characters identify the bearing geometry, the second two characters the rubber compound, and the last character the contact interaction. It is noted that μ in Table 2.1 refers to the friction coefficient value adopted for modeling contact at the top and bottom supports of unbonded bearings, as described below.

Table 2.1 Finite element models considered for developing an approach for quality control of elastomeric bearings

Model	Bearing geometry	Rubber type	Contact interaction
B1R1U	B1	R1	Unbonded ($\mu = 0.1$)
B1R2U	B1	R2	Unbonded ($\mu = 0.1$)
B1R3U	B1	R3	Unbonded ($\mu = 0.1$)
B1R2B	B1	R2	Bonded
B2R2B	B2	R2	Bonded
B2R2U	B2	R2	Unbonded ($\mu = 0.1$)
B3R2U	B3	R2	Unbonded ($\mu = 0.1$)

Figure 2.2 (a),(b),(c) illustrates the three different bearing geometries considered in this study, denoted as B1, B2, and B3. All geometries had the same plan dimensions, as shown in Figure 2.2 (d), which illustrates the mesh of geometry B1. However, in order to introduce a geometric imperfection, the interior rubber layers had different thicknesses.

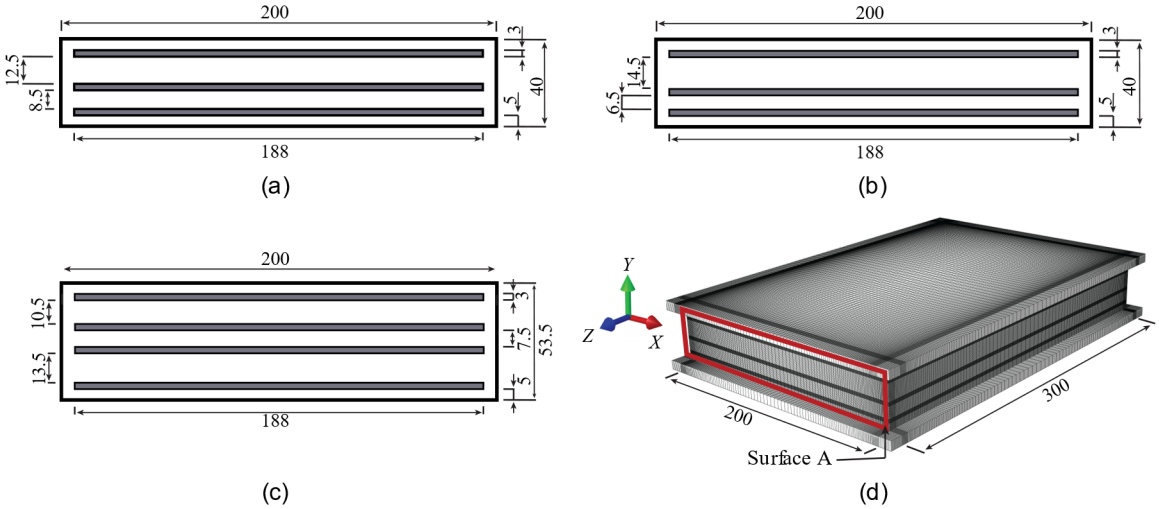

Figure 2.2 Geometry of the bearings (a) B1, (b) B2, and (c) B3 and (d) finite element mesh of bearing B1 and top and bottom plates (all dimensions in mm)

Three different rubber compounds, taken from previous studies and denoted here as R1 (Yura et al. (2001), R2 (Forni et al. (1999), and R3 (Yura et al. (2001), were chosen to examine the effect of the rubber behavior in the methodology. It is noted that R1, R2, and R3 represent natural rubbers with low, moderate, and high shear modulus, respectively. Figure 2.3 shows the experimentally recorded stress–strain relationships of the considered rubber compounds. It is noted that the stress–strain curve for R2 corresponds to pure shear loading, whereas the curves for R1 and R3 correspond to simple shear loading.

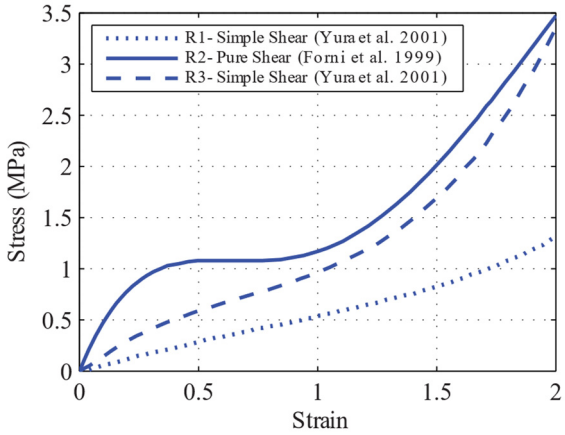

Figure 2.3 Stress-strain relationships of the three rubber compounds considered in this study, from either simple shear or pure shear

Bearings both with and without vulcanized end plates were considered in order to cover both ways elastomeric bearings are installed in bridges. Bearings with vulcanized end plates are herein referred to as *bonded*, while those without end plates are referred to as *unbonded*. Accordingly, different contact descriptions were considered at the top and bottom supports of the bearing. For unbonded bearings, the top and bottom plates served the role of loading plates, and Coulomb friction with a penalty contact method was used to model the interfaces between these plates and the rubber. This contact constraint enforcement method has been proven to be efficient in overcoming numerical issues associated with the Coulomb friction model without affecting the overall finite element response (Belivanis 2017). Friction coefficient values, μ, ranging from 0.2 to 0.5 are suggested for elastomer–steel and elastomer–concrete interfaces, depending on the smoothness of the loading plates (Muscarella and Yura 1995; Yakut and Yura 2002). In compression tests conducted as part of this study, machined-surface steel plates were used at the top and bottom of the bearings as loading plates. Vision-based measurements of the out-of-plane displacements near the top and bottom edges of the tested bearings were relatively large because of slip occurring at the top and bottom loading plates. Comparing the out-of-plane displacement values measured in the tests and those computed in FEA indicated that a value of $\mu = 0.1$ is a better lower limit for the friction coefficient. Therefore, $\mu = 0.1$ was used in the FEA of the unboned bearing models. It is noted that the bonds among rubber layers, steel laminates, and rubber cover were simulated by merging the coinciding nodes at the interfaces, effectively imposing continuity constraints; in bonded bearings, the nodes at the interfaces of the outermost rubber layers and the end plates were also merged. These modeling assumptions were reasonable because debonding was not expected under the low levels of loading applied in this study.

The rubber portions of the bearings were discretized with 8-node linear brick, hybrid, constant-pressure elements ["C3D8H" elements in Abaqus]. These hybrid elements include an extra degree of freedom that enables direct determination of the pressure and thus prevent the volumetric locking associated with nearly incompressible rubberlike materials. The steel laminates and end and loading plates were discretized using 8-node

linear brick elements with incompatible modes [C3D8I]. The addition of incompatible modes to this kind of element eliminates shear locking (Dassault Systemes 2019).

Both global and local refinements of the mesh were examined until desirable mesh sizes were achieved for both global behavior (e.g., the vertical stiffness) and local behavior (e.g., induced strains in rubber) of the bearings. Global refinement of the mesh included increasing the number of elements per rubber layer and number of elements along the length and width of the bearing. To this end, mesh sensitivity analyses were conducted on the models with a convergence criterion based on less than 1% difference in the vertical deflection (under 4 MPa pressure) between consecutive mesh refinements. For instance, for the bearing shown in Figure 2.2(d), the converged mesh included 12 and 8 elements along the thickness of the top and bottom interior rubber layers, respectively, 4 elements along the thickness of each of the top and bottom cover layers, and 120 elements along the length and width of the bearing. The mesh convergence study also examined the effects of the aspect ratios of the steel and rubber elements on the responses of interest (i.e., surface displacements and strains) to ensure that the selected aspect ratios achieved robust responses.

The vision-based methodology proposed in this study is based on strains induced in the side covers adjacent to the steel laminates, and thus are herein referred to as *steel laminate covers* (SLC), as shown in Figure 2.4(a). To accurately capture the high strain gradients developing in the SLCs, 10 elements were considered along the height of the steel laminates and their adjacent covers. Additionally, the meshes were refined locally using trapezoidal elements (see Figure 2.4(b)) toward the vertical sides of the bearings, where larger deformations were expected. With this local refinement, the vertical distance between adjacent integration points in the SLCs was reduced to about 0.1 mm.

The behavior of the rubber was described by a compressible Yeoh hyperelastic material model (Yeoh 1993), which has been used in several past studies to describe the rubber in elastomeric bearings (Stanton et al. 2008; Sun 2015; Moghadam and Konstantinidis

2017a). The model is defined by the following strain energy density function in Abaqus (Dassault Systemes 2019),

$$W = \sum_{i=1}^{3} C_{i0} \left(\overline{I}_1 - 3 \right)^i + \sum_{i=1}^{3} D_i \left(J_{el} - 1 \right)^{2i} \tag{2.1}$$

which differs slightly in appearance, but not substance, from that the original work by Yeoh (1993). In Eq. (2.1), $\overline{I}_1$ = first modified invariant of the left Cauchy-Green deformation tensor, J_{el} = elastic volume ratio, C_{10}, C_{20}, C_{30} = material constants related to the shear modulus, and D_1, D_2, D_3 = material constants that introduce compressibility. The material constants are determined by fitting the stress–strain curves resulting from this model to the curves from standard material test results. Table 2.2 lists model parameter values for the three rubber compounds, together with the corresponding values of shear modulus, G, and the material constants used. The values of D_1 = 0.001 MPa^{-1}, D_2 = 0.0 MPa^{-1}, D_3 = 0.0 MPa^{-1} correspond to a bulk modulus of 2000 MPa, the value suggested by EN 1337-3 (2005). The behavior of the steel was characterized with a bilinear elastic-plastic material model. The Young's modulus, yield stress, post-yielding tangent modulus, and Poisson's ratio were selected as 200 GPa, 248 MPa, 1034 MPa, and 0.3, respectively, corresponding to the nominal mechanical properties of ASTM A36 steel.

Table 2.2 Model parameters for the constitutive models of rubbers

Rubber	G (MPa)	C_{10} (MPa)	C_{20} (MPa)	C_{30} (MPa)	D_1 (MPa^{-1})	D_2 (MPa^{-1})	D_3 (MPa^{-1})
R1	0.6	0.2937	–0.0148	0.0032	0.001	0.0	0.0
R2	0.8	0.4813	–0.0398	0.0047	0.001	0.0	0.0
R3	1.3	0.5763	–0.0517	0.0149	0.001	0.0	0.0

The nonlinear analysis was conducted using an updated Lagrangian formulation and Newton-Raphson iteration method. An axial load of 420 kN (corresponding to 7 MPa average pressure) was applied statically in small increments. At this level of loading, the bearings remain elastic. Both material and geometric nonlinearities were applied in the analysis to accommodate the effects of large deformation and large strains.

It is noted that the bearing models were validated in compression using analytical solutions (Kelly and Konstantinidis 2011; Kelly and Van Engelen 2015), but details are not included herein due to space limitations.

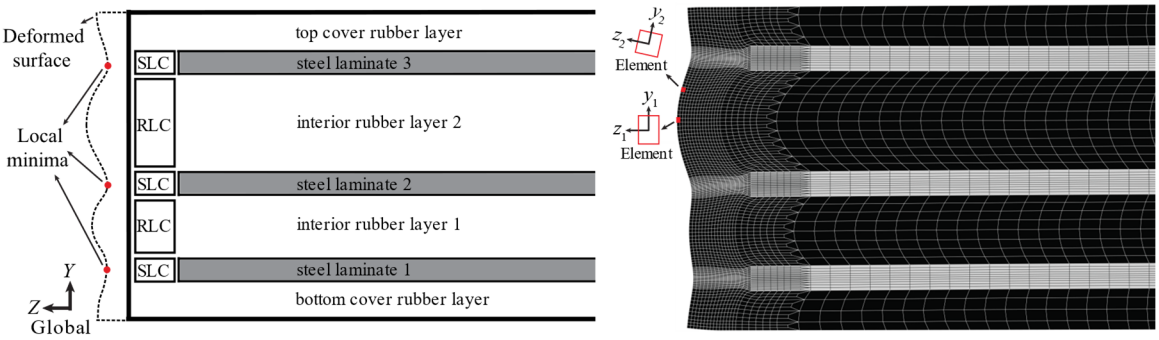

Figure 2.4 (a) Definitions of rubber layer covers (RLC) and steel laminate covers (SLC) in a bearing without geometrical imperfections (b) Deformation pattern under compression in Model B1R2U

Figure 2.4(b) shows the deformation pattern of the rubber layers close to the edge of Model B1R2U under a 7 MPa pressure. The SLC experience lower outward displacements compared to the portions of the side cover identified in Figure 2.4(a) as *rubber layer covers* (RLC), which are being squeezed out. This results in high gradients of the in-plane strain along the *y*-direction, ε_y, from tensile in the RLC to compressive in the SLC. Herein, lower-case "*y*" indicates coordinates in the *deformed* configuration (see Figure 2.4(b)), in contrast to upper-case "*Y*" which indicates coordinates in the *reference* (undeformed) configuration (see Figure 2.4(a)). The local minima of ε_y reveal the mid-height locations of the steel laminates. The reason for using ε_y, rather than ε_Y, to measure in-plane strain on the surface of bearing was because that is what the 3D-DIC program measures.

2.2.2 Identifying the Vertical Positions of Steel Laminates from Local Minima of Surface Strains Determined with FEA

Figure 2.5 shows contour plots of the displacement along the global *Z*-direction, U_Z, and the ε_y (logarithmic) on the smaller surface of Model B1R2U (surface A in Figure 2.2(d)).

As can be seen in the contours of Figure 2.5(a), the largest values of U_Z are concentrated in the RLC region of interior rubber layer 2. This is because the lateral bulging of an interior rubber layer (i.e., a rubber layer between two steel laminates) is proportional to its thickness. It is also observed that the ε_y values (Figure 2.5(b)) undulate along the height, as the RLC regions mainly experience tensile stresses in the vertical direction due to the outward expansion, while SLC regions mainly experience compressive stresses.

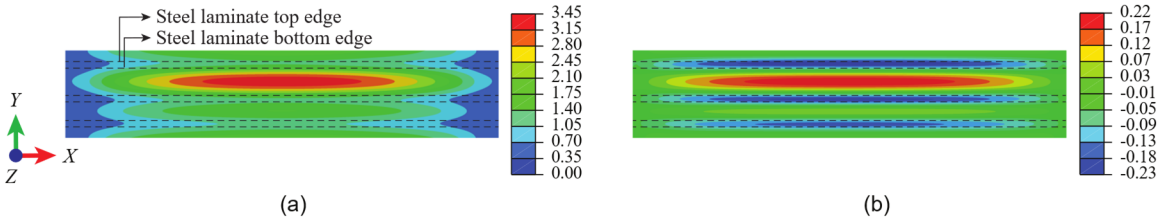

Figure 2.5 Contours of (a) U_Z (mm) and (b) ε_y on shorter side of Model B1R2U

Figure 2.6(a) shows the evolution of ε_y along line path CC′ in Model B1R2U, which is unbonded, for average pressure from 0 to 7 MPa in increments of 0.5 MPa. The vertical axis represents the vertical coordinates of material points in the reference (initial) configuration, Y. The local minima of each ε_y curve are denoted with thick dots, and the exact locations of the edges of the three interior steel laminates are shown with dashed horizontal lines. The ε_y profiles for bonded bearings are slightly different than unbonded ones, as can be seen in Figure 2.6(b) that shows the ε_y profile along line path CC′ for Model B1R2B at average pressures of 2 and 7 MPa. Most notably, in the case of unbonded bearings, the ε_y local peaks in the top and bottom cover rubber layers occur at the contact surfaces, while in the case of bonded bearings, they occur around mid-height of the cover layers, as shown in Figure 2.6(b).

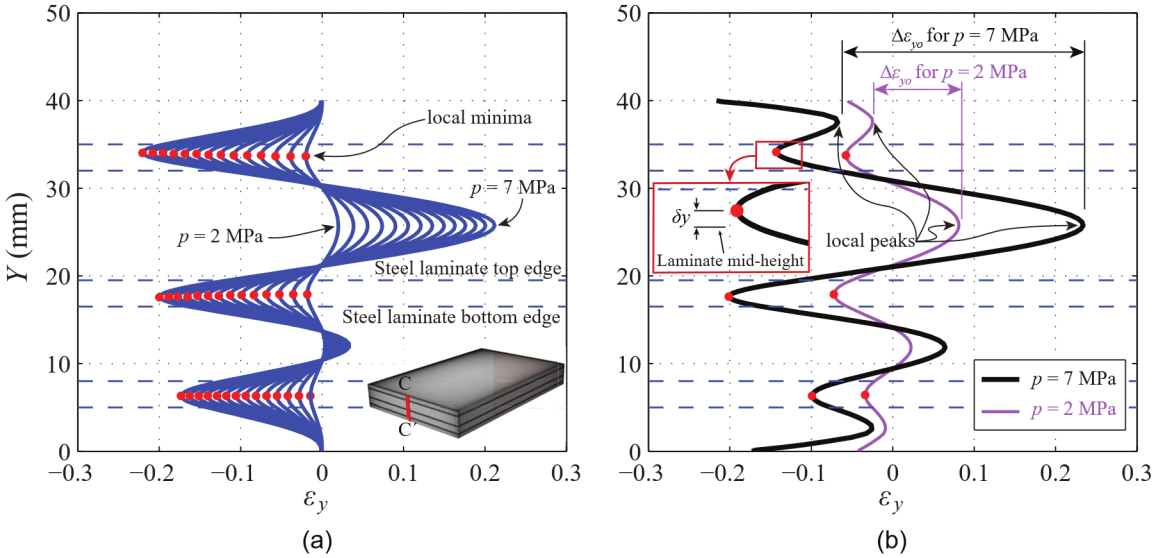

Figure 2.6 (a) Evolution of ε_y along path CC′ of Model B1R2U (unbonded) for average pressure increasing from 2 to 7 MPa in increments of 0.5 MPa and (b) ε_y response curves along CC′ of Model B1R2B (bonded) corresponding to average pressure of 2 and 7 MPa

It is observed in Figure 2.6(a),(b) that the vertical coordinate values of the local minima are nearly constant and *almost* coincide with the mid-height locations of the laminates, regardless of the applied pressure. Therefore, the local minima of the ε_y field on the surface of the bearing can reveal the mid-height locations of interior steel laminates. The reason why the local minima and the mid-height locations of the laminates do not coincide exactly is because the distribution of ε_y is mapped on the surfaces of the bearing where unequal rubber layer thicknesses cause uneven bulging, and thus the local minima there are slightly skewed from where they would appear if the mapping could be done on a plane tangent to the laminate edges. To reconcile for the fact that the ε_y local minima at the surface of the bearing do not perfectly coincide with the laminate mid-height locations, an error correction procedure is introduced, as discussed next.

2.2.3 Error Correction Procedure

Although the vertical distance (i.e., the error) between each local minimum and the mid-height of the adjacent laminate, denoted as δy, is quite small (e.g., in Figure 2.5(b), smaller than 0.2 mm and 0.6 mm under average pressures of 2 and 7 MPa, respectively), a

correction can be introduced in the approach to account for this error and improve the inference of the location of the mid-height of the steel laminate based on readings of ε_y on the surface of the bearing.

Figure 2.6(b) suggests that the error δy at a given steel laminate depends on the difference between the local maximum of ε_y in the rubber layer above the steel laminate and that in rubber layer below; that difference is herein denoted as $\Delta\varepsilon_{yo}$ (see Figure 2.6(b)). It is also observed that, as the average pressure increases from 2 to 7 MPa, the $\Delta\varepsilon_{yo}$ corresponding to the top steel laminate increases, and this is also accompanied by its local minimum shifting vertically farther from the mid-height of the steel laminate, toward the smaller of the two adjacent local peaks. This error δy can be computed based on $\Delta\varepsilon_{yo}$ corresponding to that local minimum.

FEA results of the seven bearing models listed in Table 2.1 were considered to establish a relationship between δy and $\Delta\varepsilon_{yo}$. Figure 2.7 shows the values of δy and corresponding $\Delta\varepsilon_{yo}$ for all local minima of ε_y along three line paths, AA′, BB′, and CC′ (see Figure 2.7(a)), on the surface of the considered models at various average pressures up to 7 MPa. Note that the step-like appearance of the data is due to the fact that δy attains discrete values with a resolution as fine as the height of the finite elements in the mesh. Figure 2.7(a) shows the data points corresponding to top and bottom local minima, while Figure 2.7(b) shows the data points corresponding to interior local minima. This distinction is drawn because the observed relationship between δy and $\Delta\varepsilon_{yo}$ for top and bottom steel laminates is slightly different from that for interior laminates. In contrast, inspection of the data suggested that the bonded and unbonded results were close enough to not warrant separate relationships.

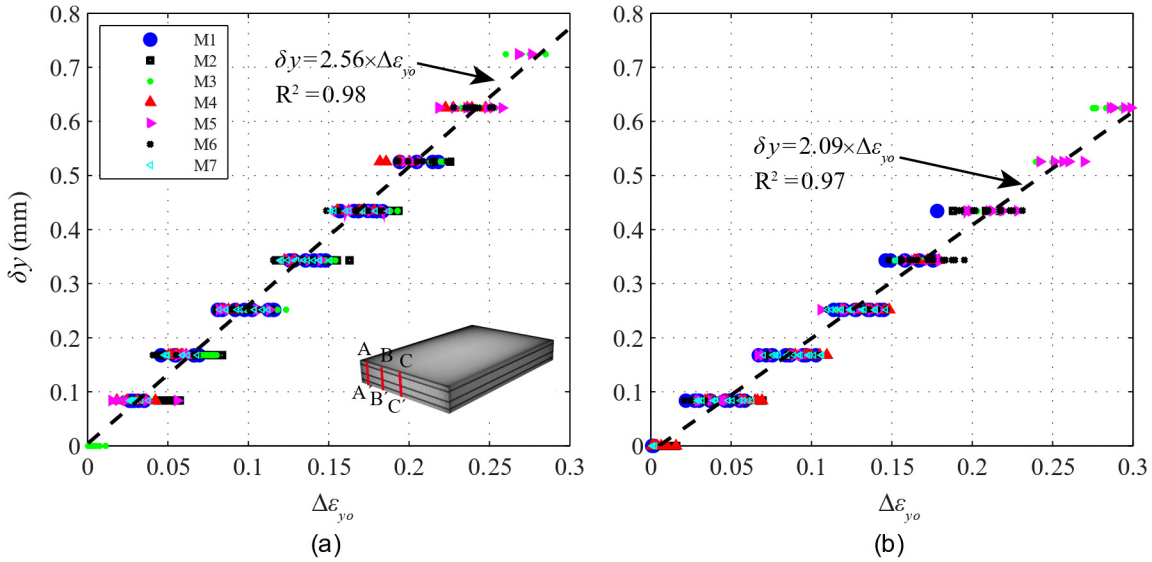

Figure 2.7 δy of (a) top and bottom local minima versus $\Delta\varepsilon_{yo}$ and (b) interior local minima versus $\Delta\varepsilon_{yo}$

Linear relationships between δy and $\Delta\varepsilon_{yo}$ were observed for both the top/bottom (Figure 2.7(a)) and interior (Figure 2.7(b)) local minima, regardless of the bearing characteristics and the considered line paths:

$$\delta y = \begin{cases} 2.56\,\Delta\varepsilon_{yo}, & \text{for the top and bottom steel laminates} \\ 2.09\,\Delta\varepsilon_{yo}, & \text{for the interior steel laminates} \end{cases} \tag{2.2}$$

where δy is in mm. These formulas can be used in the vision-based assessment of elastomeric bearings for inferring the mid-height locations of steel laminates. The actual location of the mid-height of a steel laminate would be at a distance δy from the ε_y local minimum, toward the larger of the local maximum above and the local maximum below.

A large number of reports from destructive tests on elastomeric bridge bearings (B. Huh, personal communication, 2019) show that the difference between the specified and measured thickness of the steel laminates is negligible. Therefore, once the mid-height location of steel laminates is determined using the approach introduced above, the locations of top and bottom edges of the interior steel laminates are determined, and then rubber layers thicknesses are calculated. Although some scattering exists in the data around the

fitted curves, the maximum reading error in δy (i.e., the maximum vertical distance of actual data points from the fitted curves) resulting from the use of these curves is limited to 0.1 mm. To provide some context, this level of error would translate into a mismeasurement of rubber layer thickness that, for Model B1R2U, would in turn correspond to a 1.7% error in the compression modulus of the rubber layer, obtained using analytical expressions (e.g., Kelly and Konstantinidis (2011)) for the compression modulus of rectangular bearings. Thus, the presented approach offers a robust identification of the thicknesses of rubber layers along a desired vertical line on the surface of the bearing.

2.2.4 Determination of the Thickness of Side Covers

Current quality control testing procedures also require the measurement of the thickness of the side covers (OPSS 2017; AASHTO 2018). For instance, AASHTO (2018) specifies lower and upper design tolerances for the thickness of side covers to be -0 mm and +3 mm. An alternative, nondestructive approach is presented in this section to approximately quantify the thickness of side covers. An investigation of surface displacements and strains in different bearing models was conducted, and it was observed that the horizontal displacement pattern parallel to a free surface (e.g., U_X on Surface A in Figure 2.2(d)) and close to the edge of a bearing can help identify the thickness of the side cover in that direction. Figure 2.8(a) shows U_X along the line path DD′ in Model B1R2U as the average pressure is increased from 0 to 7 MPa in increments of 0.5 MPa. Figure 2.8(a) indicates that a local minimum forms in the U_X response curve close to the edge of the bearing. This feature in the U_X pattern occurs because of the transition from the segment of the side cover behind which there is a steel laminate to the segment behind which there is no laminate. The local minima in Figure 2.8(a) are always forming at a horizontal distance of 5 mm from the right edge of the bearing, regardless of the applied pressure, while the exact thickness of the right side cover is equal to 6 mm. Therefore, the local minimum in the U_X response curve seems to be approximately indicative of the end of the steel laminates and thus the thickness of the side cover at the bearing edge along the considered line path. Figure 2.8(b) shows the U_X response curves along the three line paths shown (the mid-

height of the three steel laminates) in Model B1R2U under an average pressure of 7 MPa. Figure 2.8(c) shows the U_X response curves along similar line paths in Model B2R2U, in which there is a 4-mm vertical misalignment of the middle steel laminate toward the bottom edge of the bearing. Model B2R2U represents a bearing with an extreme misalignment of one interior laminate (equal to 4 mm). Comparing the locations of local minima in Figure 2.8(b) and (c) shows that the thickness of the rubber layers above and below the line path affect the location of the formed local minima. However, the formed local minimum on the U_X response curve can reveal the thickness of the side cover with an error of less than 1 mm in most cases. Also, the thickness average of the side covers close to each end (determined using this approach) is even closer to the exact thickness of the side cover (i.e., 6 mm).

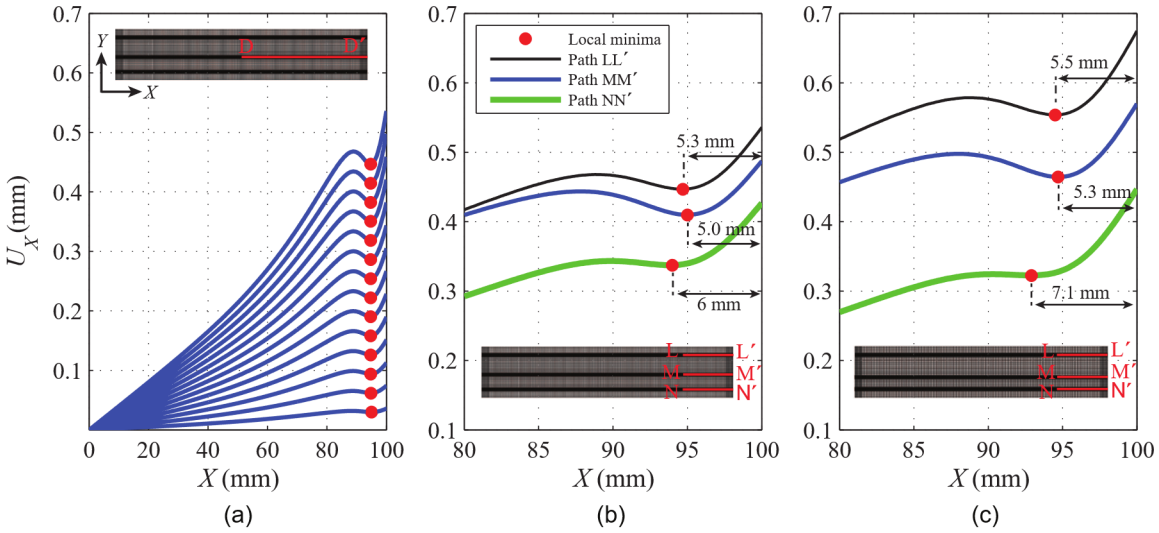

Figure 2.8 (a) U_X along the mid-height of the interior steel laminate (path DD′) in Model B1R2U (b) U_X along three paths (LL′, MM′, and NN′) in Model B1R2U, and (c) U_X along three paths (LL′, MM′, and NN′) in Model B2R2U

It is noted here that the thickness of the side cover around a bearing can be also determined by inserting a needle-like object at the determined steel laminate elevations until it comes in contact with the edges of the laminates. This allows for a straightforward corroboration of the side cover thickness values inferred by 3D-DIC. The tiny holes created by the

insertion of the needle-like object will be filled in by rubber when the bearing is loaded in service, and thus there is no concern of corrosion of the steel laminates.

In passing, it is noted that the error in the side cover thickness measurements is of significance from the corrosion protection standpoint rather than that of structural performance. For instance, Yura et al. (2001) showed that the thickness of the side cover does not have a significant effect on the structural behavior and integrity of bearings.

2.3 Experimental Testing of Laminated Elastomeric Bearings Using Digital Image Correlation

This section presents an experimental investigation conducted to benchmark the proposed vision-based methodology for determining the internal structural of manufactured laminated elastomeric bearings. First, a brief overview of the DIC optical method is presented, followed by a description of the experimental tests.

2.3.1 Digital Image Correlation: an Overview

DIC measurements involve tracking the subsets of pixels (facets) on digital photographs of an object's surface at two different deformation states. Prior to image acquisition, it is necessary to apply a suitable speckle pattern on the surface so that facets can be identified unambiguously after deformation. A calibrated stereo-camera system consisting of two cameras is required to output the 3D surface displacement and strain fields precisely (Pan et al. 2009). Stereo-camera calibration involves characterizing of the intrinsic parameters (i.e., principle point and skew, distortion parameters, optical scale factor) of each camera and extrinsic parameters (i.e., orientation and spacing of the cameras to one another). Intrinsic and extrinsic parameters are computed from a series of images of a target panel based on the pinhole model (Born and Wolf 1965) and using a bundle adjustment calibration algorithm (Triggs et al. 1999). Then, the 3D position of a scene point is computed with a triangulation technique (Hartley and Sturm 1997), and the full 3D surface of the object is reconstructed by employing this process for each stereo pair of images (see Figure 2.9). When the specimen is loaded, its surface is deformed. Then, the 3D

displacement field of the surface is computed by tracking the grayscale value patterns of many facets using stereo-correlation algorithms (Orteu 2009). Finally, surface strains are calculated by numerical differentiation of the displacement fields together with smoothing techniques according to the evolution of defined facets (Sutton et al. 2009).

Figure 2.9 3D reconstruction of a compressed bearing surface using 3D-DIC

2.3.2 Bearing Specimens and DIC Test Setup

The specimens tested in compression were two elastomeric bridge bearings without steel end plates, both having plan dimensions of 300×200 mm but different overall design thicknesses of 40 mm and 100 mm. Thus, the two bearings are hereinafter referred to as the "40-mm bearing" and the "100-mm bearing". Table 2.3 lists details of the bearing designs.

Table 2.3 Geometric characteristics of the tested bearings

Property	Test specimen	
	40-mm bearing	100-mm bearing
Plan dimensions (mm)	300×200	300×200
Height (mm)	40	100
Interior rubber layer thickness (mm)	10.5	9.4
Steel laminate thickness (mm)	3	3
Number of steel laminates	3	8
Cover rubber layer thickness (mm)	5	5
Side cover thickness (mm)	6	6

The DIC setup included four cameras, which were arranged into two synchronized 2-camera stereo-camera systems, as depicted in Figure 2.10 (a), (b), and (c), viewing two opposite sides of the bearing. Camera Set I included two 12-megapixel (MP) digital cameras [Manufacturer: IO Industries, model: Flare 12M180MCX-F] equipped with lenses of fixed 35-mm focal distance. Camera Set II system included two 5-MP digital cameras

[Manufacturer: Fastec Imaging, model: IL5-Q QSXGA] equipped with lenses of fixed 35-mm focal distance. Each camera set was mounted on a rigid cross bar so that their spacing and orientation with respect to each other was fixed during each test. Each cross bar was secured on a tripod setting to level the centerline heights of the lenses and bearings. LED lights were used for each stereo-camera system to provide consistent and uniform lighting on the area of interest, i.e., the vertical faces of the specimens. These lights were mounted at relatively low angles from the vertical faces of the bearing to reduce light reflections on the camera lenses (see Figure 2.10).

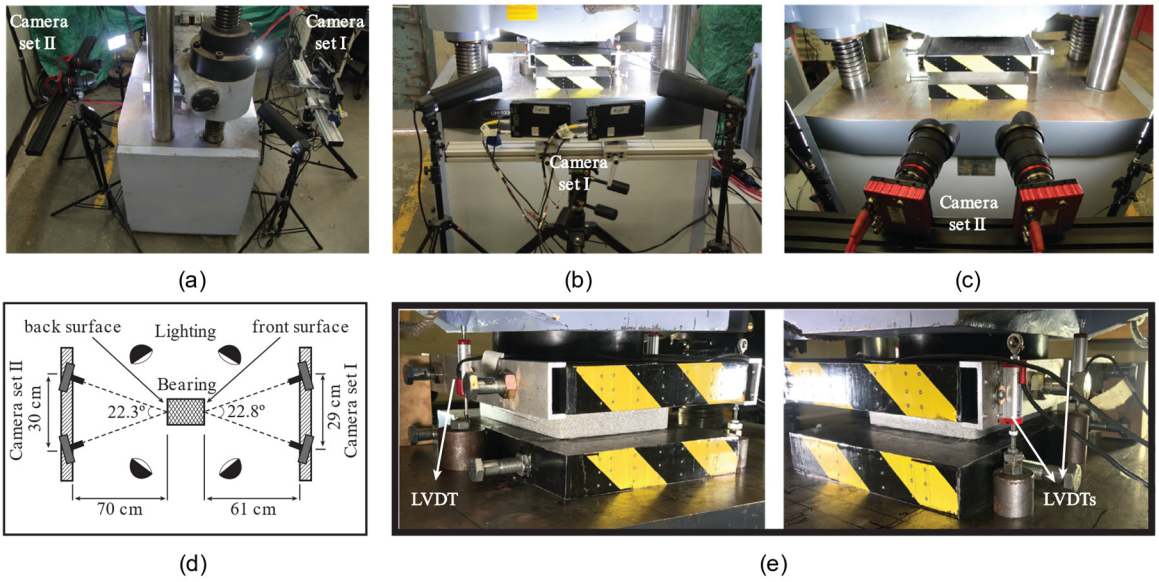

Figure 2.10 (a) DIC setup, (b) Camera set I (c) Camera set II (d) Plan view schematic (e) LVDT Transducer

The working distance of the cameras was selected such that their field of view would cover the entire area of interest throughout the experiments. The stereo angle between the cameras' optical axes was fixed at approximately 23°, which is within the recommended range of 20°–25° for DIC measurements, as angles below 20° decrease the precision of triangulation and thus the out-of-plane coordinates and displacements (Freddi et al. 2015), and angles above 25° create problems related to the bias and loss of contrast (Sutton 2013). Figure 2.10(d) shows the selected testing configuration for Camera Sets I and II. Besides the stereo-camera systems, three linear variable differential transformer (LVDT)

displacement sensors, with 0.01 mm resolution, were used in the positions shown in Figure 2.10(e) to identify any rotation in the loading plates, which would result in nonuniform compression of the bearings. The arrangement of LVDTs shown in Figure 2.10(e) enabled a comparison between the relative rotations of the top and bottom loading plates measured by the LVDT sensors and the stereo-camera systems.

Prior to the experimental testing, the stereo-camera systems were calibrated. A calibration grid target with 23×18 dots uniformly spaced at 8.3 mm on-center was used to compute the needed projection parameters, including the intrinsic and extrinsic parameters. Each stereo-camera system was calibrated separately by capturing 17 images of this target at various locations and orientations within a calibration volume. Once these calibration images were captured, the automatically recognized dots used by the 3D-DIC software were utilized to compute the projection parameters for DIC measurements in the compression tests.

2.3.3 Specimen Surface Preparation

The applied speckle pattern on the surface of the specimen plays a key role in uniquely identifying the facets on the digital images after deformation. In addition, an appropriately created pattern improves both accuracy and precision of the DIC computations because it enhances the interpolation of the grayscale values in the images and enables displacement measurements with sub-pixel accuracy (Birolini 2013). Sutton et al. (2009) recommended that the speckle pattern should be non-periodic, isotropic, of high contrast, and that the speckle granules should not vary too much in size, i.e. speckle granules of 3–5 pixels diameter or slightly larger (Freddi et al. 2015), with a density of 45-55% (Lane et al. 2008), are recommended.

Given the scale factor of 10.2 pixels/mm for both stereo-camera systems and chosen speckle granule of 4.5-pixel diameter on the digital images, in this study, the bearing surfaces were patterned with speckle granules of 0.44 mm with 55% density and overall randomness of 60%. Figure 2.11(a) shows a representative sample of a speckle pattern used in the experiments. The field of view of Camera Set II was set 1.6 times larger than the

field of view of Camera Set I in order to get almost identical scale factors in both systems (i.e., similar speckle sizes in both systems).

In this study, a *water-transfer printing* technique was employed for patterning the surfaces of the bearings. This technique, which enables transferring computer-generated patterns on the specimen surface, has been shown to produce high-quality patterns with relatively small speckles (Chen et al. 2015). The technique involves printing a suitable pattern (see Figure 2.11(a)) on a transfer paper, which is then transferred to the specimen surface. A transfer paper consists of two main components: the prefabricated decal and printed speckle pattern, as shown in Figure 2.11(b). The prefabricated decal part is composed of an absorptive paper (base layer), a water-soluble slip layer, and a transparent elastic layer on which the speckle pattern is printed. The transparent elastic layer is easily separated from the base layer once the water permeates the base layer.

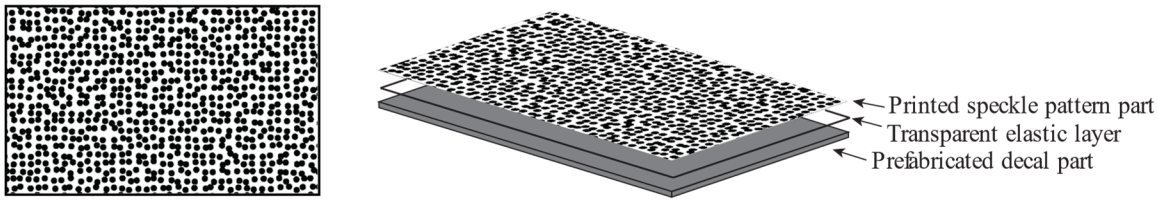

Figure 2.11 (a) Printed speckle pattern (b) decal transfer paper

The following procedure was used to generate the speckle pattern on the bearing surfaces. The bearing surface was sprayed with white matte paint to act both as an adhesion promoter and a high-contrast carrier of the printed pattern. The speckle pattern, generated on the computer, was printed on the side of the transfer paper with the transparent elastic layer. When the white spray paint on the bearing surface became tacky, the printed side of the transfer paper was affixed onto the bearing surface. This was done while the dots were still damp, which allowed them to mix a little with the white paint. Then the base layer was moistened with a brush uniformly to loosen the base layer and detach it from the transparent elastic layer, which remained affixed onto the specimen surface. The transparent layer was then gently peeled off, leaving the speckles attached to the white paint. The resulting pattern on the front side of the 40-mm bearing is shown in Figure 2.12.

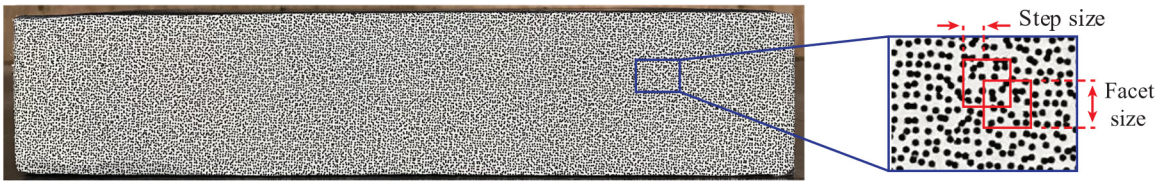

Figure 2.12 Applied speckle pattern on 40-mm bearing with enlarged view of bearing showing two adjacent facets

2.3.4 Loading Protocol and Acquisition

The experimental program included a quasi-static displacement-controlled compression test for each specimen. The displacement rates for the 40- and 100-mm bearings were 0.25 and 0.6 mm/min, respectively, corresponding to the average vertical stress rate of roughly 0.8 MPa/min. Image pairs were captured by the stereo-camera systems at increments of 0.5 MPa. Cameras in Camera Set I and Camera Set II were synchronized using the Fastec FasMotion Controller software (Fastec Imaging 2014) and Express CoreView software (IO Industries 2016), respectively, and the image pairs were captured by the two systems simultaneously.

2.3.5 Processing of Stereovision Data

Facet size and step size are important parameters in DIC (Ahmadi et al. 2020). The facet size defines the square pixel-based area (see Figure 2.12) over which the facet matching algorithm is applied, and each facet is affiliated with a center point for which position and displacement are computed. Although a larger facet makes it easier to track the given facet and improve accuracy by reducing errors related to noise effects, speckle pattern quality, lighting conditions, and image distortion, it may result in loss of information associated with high displacement and strain gradients. As a rule, the facet size should be small enough to enable observing local effects and gradients but not so small to compromise the facet matching between deformation states. This is typically done by selecting the facet size, such that each facet contains at least 3 speckle granules (Sutton et al. 2009). The step size, measured in pixels, defines the center-to-center distance between facets and determines the amount of overlap between them (see Figure 2.12). A smaller step size results in larger measurement point density and thus higher spatial resolution.

The DIC software GOM Correlate Professional (GOM 2018) was used to produce full-field displacements and strains on two opposite sides of the bearings [see Figure 2.10(d)]. The in-plane strains at a point on the bearing's surface were computed in GOM over an equilateral hexagon around the respective point. This equilateral hexagon consists of triangles, the corner points of which are the facet centers, and the size of such a hexagonal neighborhood is defined in GOM based on the user-defined strain tensor neighborhood. It is noted that the logarithmic definition of strain was used for the 3D-DIC computations of ε_y, as with the FEA computations of ε_y.

The effects of facet size and step size on the random errors were investigated by processing 40 still images of each bearing surface. The first image pair from each stereo-camera system was chosen as the reference for that system, and the statistics of U_Z and ε_y (e.g., their median, standard deviation, quartiles, and most extreme values) were examined. These statistics were computed for each bearing surface based on measurements at 35 points from different regions of that surface (e.g., top, bottom, middle, left, right, etc.). It is noted that the directions of the coordinate axes were the same as those in the FEA discussed above.

The step size was found to have no notable effect on the statistics of U_Z and ε_y. Therefore, a small step size of 3 pixels was adopted to accurately quantify displacement and strain gradients while keeping computation time manageable. Figure 2.13 presents box-and-whisker plots of U_Z and ε_y obtained with a step size of 3 and with different facet sizes for the front surfaces of the tested bearings. On each box, the central mark indicates the median, and the bottom and top edges of the box indicate the 25th and 75th percentiles, respectively. The whiskers extend to the most extreme data points. Also, trend lines have been drawn in Figure 2.13 over the average of the 40-mm and 100-mm bearing extreme data points. It is observed in Figure 2.13(a),(b) that the statistics of U_Z and ε_y are fairly constant while the facet size decreases from 26 to 16. However, the statistics of ε_y get worse abruptly as the facet size decreases from 16 to 14. For instance, the trend lines drawn over

the extreme data points in Figure 2.13(b) clearly shows considerable increases of the most extreme U_Z and ε_y values as the facet size decreases from 16 to 14. Therefore, a facet size of 16×16 pixels for both surfaces was selected in order to achieve a balance between precision and accuracy (which is higher for larger facets) and spatial resolution (which is higher for smaller facets). The chosen facet size ensured the encompassment of at least three speckle granules in each facet on all surfaces. Also, standard deviations of U_Z and ε_y (which quantify the overall precision of the systems) for all data points (except the points very close to the left and right edges), on all assessed surfaces, were less than 0.008 mm and 100 μm/m, respectively. The readings of U_Z and ε_y in the target regions of the bearing surfaces were expected to be higher than these standard deviation values by many orders of magnitude during the compression tests.

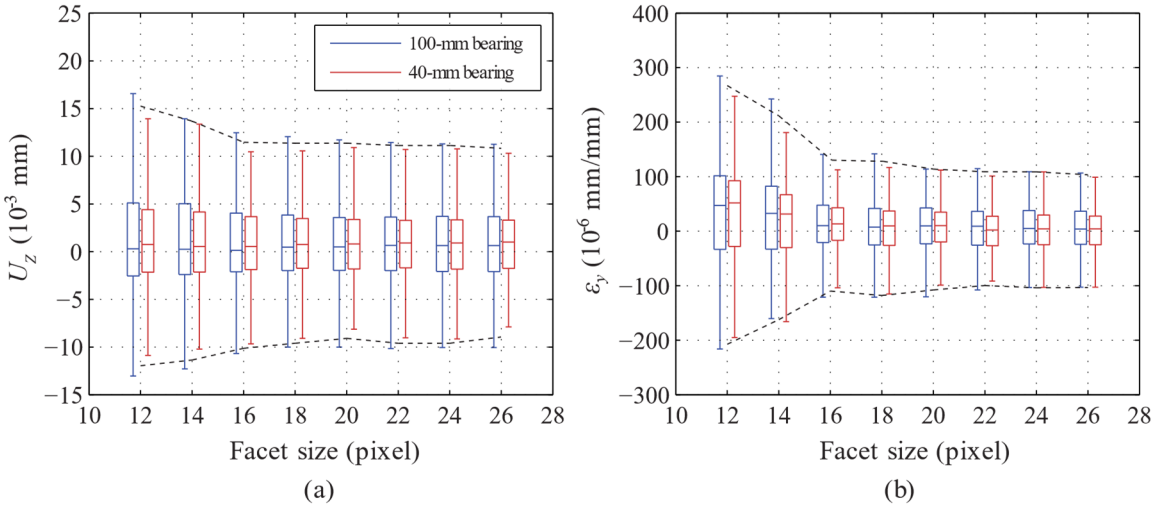

Figure 2.13 (a) $\overline{U}_Z$ and σ_{U_Z} and (b) $\bar{\varepsilon}_y$ and σ_{ε_y} as functions of facet size based on measurements on the front surfaces of bearings with a constant step size of 3

2.4 Experimental Results and Discussion

2.4.1 DIC-Based Measurements of UZ and ε_y on the Bearing's Vertical Surfaces

Figure 2.14 depicts the U_Z contours on the front and back surfaces (see Figure 2.10(d)) of the 40-mm bearing under 7 MPa average pressure, superimposed on the image of the bearing taken from the left camera, which due to the viewing perspective makes the left

vertical edge of the bearing appear taller than the right vertical edge. Note that the *Z*-direction in each image is the outward-pointing normal direction to the undeformed vertical surface of the bearing. Similar to the FEA results presented previously, it is observed that U_Z undulates along the vertical direction, attaining high values in the RLC regions (yellow and red contours) and low values in the SLC regions (green contours). The maximum lateral bulging (i.e., maximum U_Z values) occurs in similar regions of the front and back surfaces. Similar to the FEA contours in Figure 2.5(a), the contours of Figure 2.14 reveal that interior rubber layer 2 is thicker than interior rubber layer 1. Also, U_Z values near the top and bottom edges and far from corners are relatively large compared to other regions. This occurs because, in addition to bulging, the top and bottom cover rubber layers experience slip at the interfaces between the rubber and the supports (Kelly and Konstantinidis 2009; Konstantinidis and Moghadam 2016).

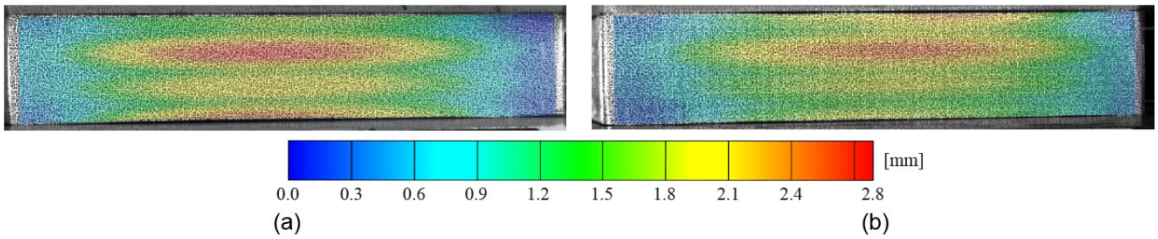

Figure 2.14 U_Z contour maps obtained through 3D-DIC; (a) Front surface (b) Back surface of the 40-mm bearing

Figure 2.15 shows ε_y contours on the front and back surfaces of the two bearings under 7 MPa average pressure. The strains in these contours are based on computations using a strain tensor neighborhood with 0.45-mm length, which is small enough compared to the thickness of the steel laminates and rubber layers to capture gradients of strains. This strain reference length makes the strain results around local peaks of ε_y be comparable to the ε_y results in the FEA in which the height of individual rubber elements around similar regions were 0.45 mm.

Similar to the previously presented FEA results, ε_y in Figure 2.15 undulates from compressive to tensile along the height, and this strain gradient can be analyzed to

determine the number of interior steel laminates. For instance, the ε_y contours exhibit local minima on three and eight horizontal strata (dark blue bands) in the 40-mm and 100-mm bearings, respectively, revealing the presence of three and eight steel laminates.

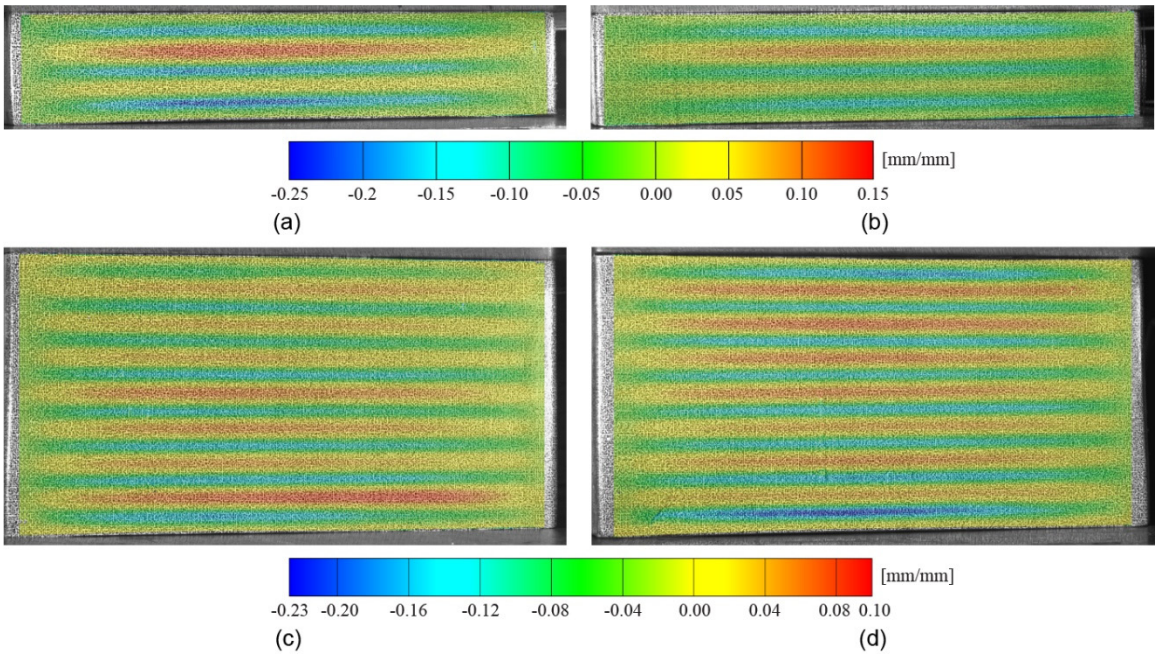

Figure 2.15 ε_y contour maps on (a) front surface (b) back surface of the 40-mm bearing and on (c) front surface (d) back side of the 100-mm bearing

Given that the ε_y local maxima in the RLC regions are proportional to the thicknesses of the corresponding internal rubber layers, Figure 2.15 (a),(b) clearly indicate that interior rubber layer 2 is thicker because of the vertical misalignments of the laminates. Also, rotational misalignments of the steel laminates (tilt) along the *Z*-direction (i.e., from the front to the back surface) can be detected from measuring different ε_y peak values on the RLC regions of two opposite surfaces of a bearing. For instance, Figure 2.15 (c) shows that RLC regions closer to the bottom edge experience higher ε_y peak values on the front surface of the 100-mm bearing, while Figure 2.15 (d) shows more uniform distribution of ε_y on the RLC regions on the back surface. This may happen if the steel laminates are not parallel along the *Z*-direction, but a closer look at the motion of the top and bottom loading plates, which was measured by both stereo-camera systems and the LVDTs, revealed that

the loading plates experienced rotation during the tests. This, in turn, resulted in higher compression of the bearings toward their front sides, and thus in higher ε_y peak values on these sides.

Figure 2.16 shows the U_Z and ε_y profiles along the line path BB′ on the back surface of the 40-mm bearing, as indicated on the bottom-right corner of the figure. The series of curves illustrate the evolutions of U_Z or ε_y when the average pressure is increased from 2 MPa to 7 MPa in increments of 0.5 MPa. As in Figure 2.16, these responses are plotted against the vertical coordinates of material points in the initial configuration. Since machined-surface steel plates were used at the top and bottom of the bearing as loading plates in the compression test, the ε_y profiles exhibit behavior corresponding to unbonded bearings, i.e., similar to Figure 2.16(a). Figure 2.16 demonstrates how the rubber layers of nonuniform thickness affect the evolution of these responses. The U_Z curves indicate that the maximum bulging for the 40-mm bearing occurs at interior rubber layer 2, while the maximum slip occurs at the top cover rubber layer. In contrast, the maximum compressive strains, shown in the ε_y subplots, occur on the portion of the cover between these two layers.

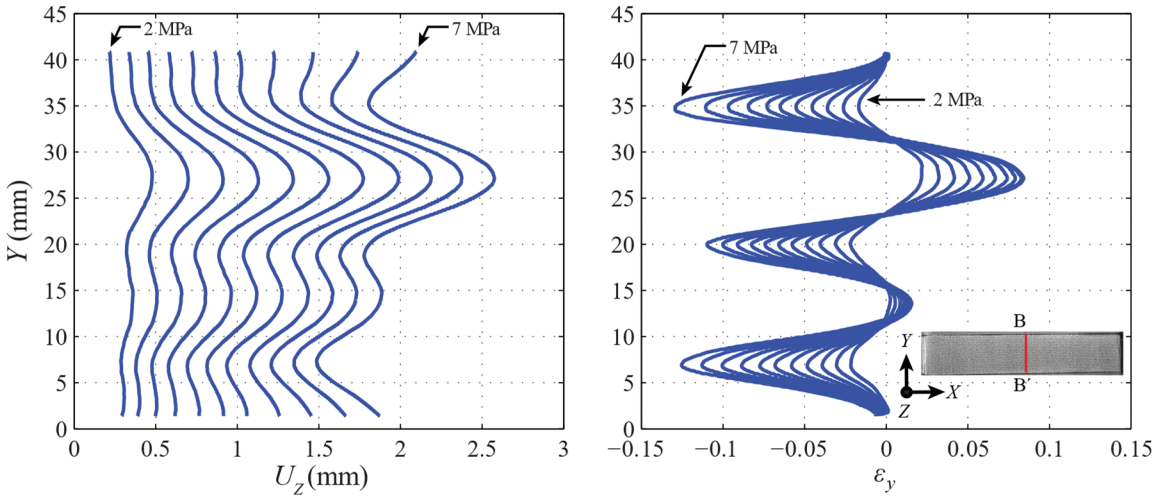

Figure 2.16 Evolution of U_Z and ε_y along the line path BB′ on the back surface of the 40-mm bearing, indicated in the bottom-right corner

2.4.2 Vertical Positions of the Steel Laminates and Rubber Layers: Identification by 3D-DIC and Validation by Destructive Testing

The pictures on the left of Figure 2.17(a) show the two bearings tested nondestructively. The centerlines CC′ and DD′ indicate locations used to identify the vertical positions of the steel laminates by 3D-DIC. Figure 2.17(b),(c) shows the ε_y profiles at 7 MPa average pressure and the formed local minima for two bearings. The error correction procedure described by Eq. (2.2) (or the fitted curves in Figure 2.17) was then used to accurately pinpoint the mid-height position of the steel laminates. From this and knowing that the steel laminates were 3 mm thick (per specification), the edges of the steel laminates were identified across the centerlines CC′ and DD′ for the 40-mm and 100-mm bearings, as shown in Figure 2.17 (b) and (c) with horizontal dashed lines. For instance, the middle local minimum shown in Figure 2.17 (b), at $Y_{\min} = 20$ mm, lies between two local maxima with $\varepsilon_y = 0.08$ and 0.01 in the top and bottom interior rubber layers, respectively. Using the difference of the two, $\Delta\varepsilon_{yo} = 0.07$, in Eq. (2.2) gives $\delta y = 0.25$ mm, which indicates that the expected location of the mid-height of the middle steel laminate is at a distance 0.25 mm from the middle local minimum, toward the larger of the local maximum above and the local maximum below. Therefore, the expected locations of the top edge and the bottom edge of the middle laminate are at $Y = Y_{\min} + t_s/2 + 0.25 = 21.7$ mm and $Y_{\min} - t_s/2 + 0.25 = 18.7$ mm, respectively, where t_s = thickness of the steel laminates. This approach was followed for locating all steel laminate edges of the tested bearings. The interstitial spaces between any two steel laminates, as well as the top/bottom steel laminate and the top/bottom support, were occupied by rubber. The rubber layer thickness values obtained using the nondestructive methodology are shown in the graphs.

To validate the nondestructive methodology and its ability to accurately infer the internal structures of the two laminated rubber bridge bearings using 3D DIC, its predictions were compared against the actual internal structures of the bearings as ascertained by saw cutting in the same fashion as such bearings are currently tested destructively by departments of transportation before acceptance. The right photographs in Figure 2.17(a) show the two

bearings after they were cut. Closeups of these photographs around lines CC′ and DD′ are shown to the right of the graphs in Figure 2.17(b) and (c), together with the actual thicknesses of the rubber layers. A comparison of these measurements to those indicated in the graphs demonstrates that the proposed methodology, based on 3D-DIC, emerges as an accurate nondestructive assessment methodology for laminated elastomeric bridge bearings.

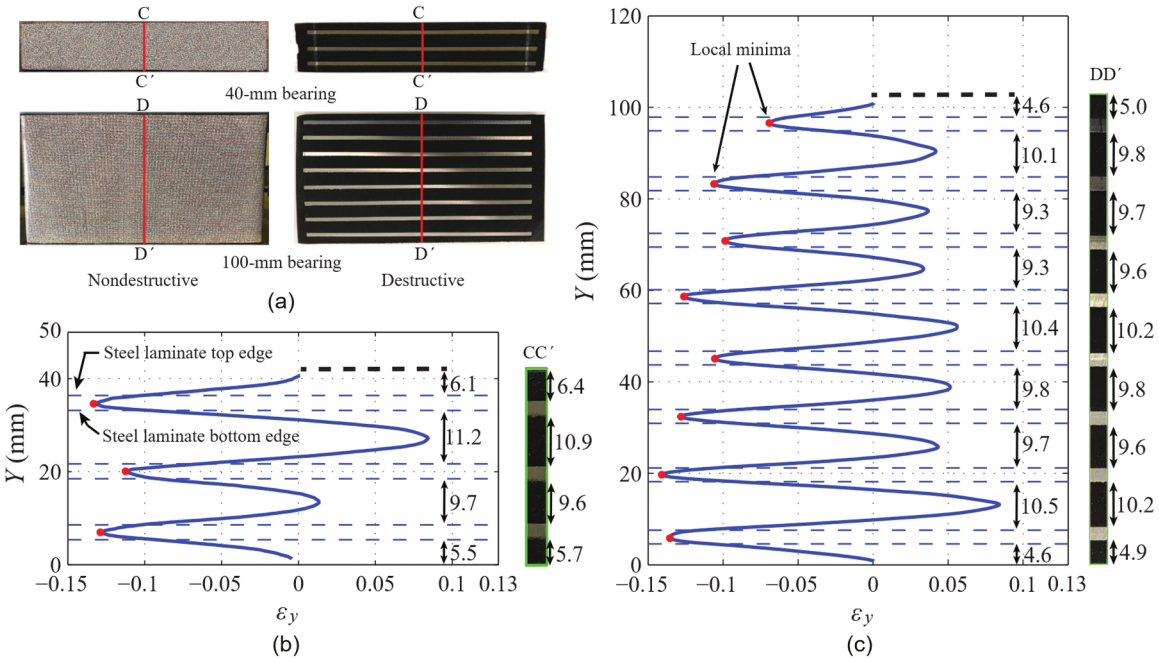

Figure 2.17 (a) Photographs of the two bearings tested nondestructively (left) and destructively (right) indicating the centerlines CC′ and DD′ along which the results of the two approaches are compared. ε_y profiles at 7 MPa indicating the local minima and inferred steel laminate edges compared with actual structure (from destructive tests) of (b) the 40-mm bearing and (c) the 100-mm bearing

AASHTO (2018) specifies that if the thickness of each rubber layer at any point within the bearing is exceeded from general upper and lower limits (i.e., ±3 mm), misalignments of the top and bottom laminates should satisfy $7.5\theta + v/t \leq 0.35$ (provided that $\theta \leq 0.02$ radians) where t = the design thickness of the rubber layer, and v, θ = the relative vertical misalignment (mm) and rotation of associated steel laminates, respectively. Given the geometric characteristics of the tested bearings, as shown in Table 2.3, the measured

thickness of the interior rubber layers (Figure 2.17) meet the tolerance of ±3 mm per AASHTO (2018).

2.4.3 Measuring the Side Cover Thickness Using 3D-DIC

The proposed methodology was also used to predict the thickness of the side cover of the tested bearings. Figure 2.18(a) shows the contour plot of ε_y on the right side of the front surface of the 100-mm bearing at 7 MPa. The blue colors in the ε_y contour plot (eight horizontal strata) revealed the mid-height of interior steel laminates, and thus eight line paths through these horizontal strata were considered for assessing the U_X profiles. Figure 2.18(b) shows the U_X profiles along these line paths together with their local minima, and the distance of each local minimum from the right edge of the bearing. As discussed earlier, the horizontal distance of the local minima from the bearing edge is expected to show the approximate thickness of the side cover adjacent to the right end of each laminate.

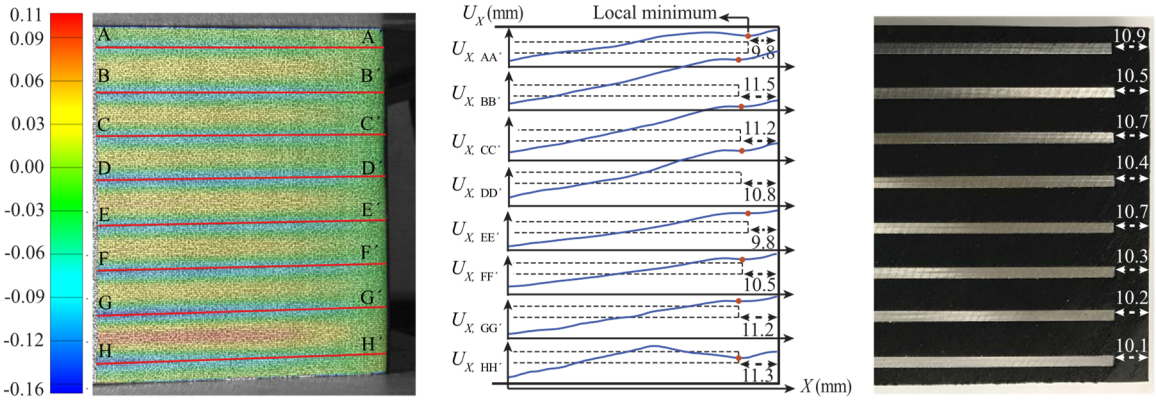

(a) (b) (c)

Figure 2.18 (a) ε_y contour map on the right side of the front surface of the 100-mm bearing, (b) U_X profiles along mid-height of the eight interior laminates (horizontal paths shown in (a)) at 7 MPa indicating the local minima and inferred thickness of side covers, and (c) exact thicknesses of side covers on right side of the front surface of the 100-mm bearing

To validate the methodology for estimating side cover thickness, comparisons were made with results from the destructive tests. Figure 2.18(c) shows the exact thickness of side cover adjacent to the right end of each laminate on the same side of the 100-mm bearing after cutting the bearing. The average of the exact thickness of the side cover adjacent to

laminates in Figure 2.18(c) is equal to 10.47 mm, while the corresponding inferred value in Figure 2.18(b) is equal to 10.76 mm. This demonstrates that the proposed methodology is accurate for also predicting the side cover thickness of bearings.

2.4.4 Complete Internal Structure of Laminated Elastomeric Bridge Bearings Identified by 3D-DIC

The proposed methodology suggests the use of horizontal and vertical line paths along the surfaces of bearings to determine the locations of the steel laminates, the thicknesses of the interior rubber layers, and the thicknesses of the side covers of the bearing without having to destroy it (i.e., cut it) (see Figure 2.19). To this end, each horizontal edge of an interior laminate across the surfaces was estimated by fitting a curve through the data points representing the edge of that laminate along six considered vertical line paths. Figure 2.19 also shows how efficiently the proposed methodology can identify the internal structure of an elastomeric bridge bearing.

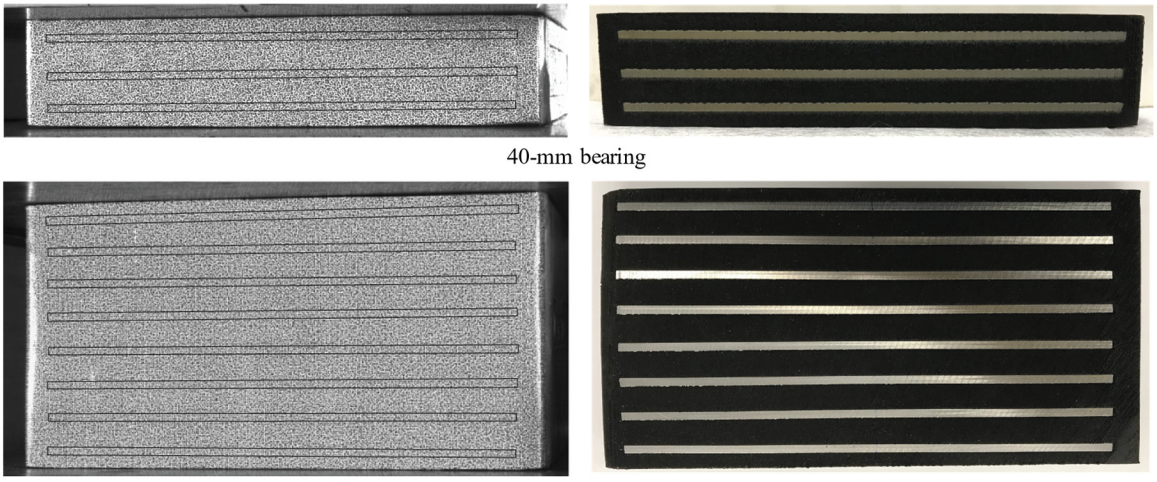

Figure 2.19 Internal structure of the two bearings considered in this study, as determined by the nondestructive, vision-based methodology (left) and by destructive testing (right)

2.5 Conclusions

This paper presented a nondestructive, vision-based methodology for assessing the internal structure of laminated elastomeric bridge bearings during compression tests. The presented

methodology enables the quantification of important geometrical properties of elastomeric bearings including the thickness of interior rubber layers, the thickness of side covers, and any potential steel laminate misalignment and bending. The methodology is based on gradients of displacements and in-plane strains on the vertical surfaces of compressed bearings and requires knowing the thickness of steel laminates. It was developed using FEA and was benchmarked in an experimental investigation involving the application of 3D-DIC in compression tests of two bearings. The paper discusses the test procedure with an emphasis on elements of 3D-DIC, including the application of the speckle pattern on the specimen surface, lighting conditions, and image processing. The procedure for determining the vertical positions of the steel laminates and side cover thickness from 3D-DIC measurements of displacement and strain was described. The methodology was validated by comparing its predictions against the actual internal structure of the two bearings, determined by destructive testing (cutting the bearings open). In summary, the methodology requires only the application of 3D-DIC to measure fields of displacement and in-plane strain on the surface of compressed bearings and post-processing data using the approach described in Section 2.2 of this paper. Using this methodology, the thickness of each interior rubber layer and the thickness of the side covers of the bearing was determined with a high level of accuracy.

Future studies can focus on nondestructive testing of circular elastomeric bearings, for which the curved vertical surfaces would present new challenges. Additionally, the vision-based measurement technique seems to be promising for studying the effects of steel laminate misalignment and bending on the onset and propagation of elastomer debonding from steel laminates, which are the most common modes of failure in elastomeric bridge bearings. Its application can be also extended to support the validation and calibration of numerical and analytical models.

Data Availability Statement

All data, models, and code generated or used during the study appear in the submitted article.

Acknowledgments

This research was supported by the Ministry of Transportation of Ontario (MTO) through the Highway Infrastructure Innovation Funding Program (HIIFP), Award No. 9017-R-0022. The authors are grateful to Kris Mermigas, Head Engineer, Bridge Design Office, MTO, and Jennifer Astle-Tranmer, Senior Materials Officer, Materials Engineering & Research Office, MTO, for their committed support during this work. Any opinions, findings, and conclusions or recommendations expressed in this paper are those of the authors and do not necessarily reflect the views of the sponsor.

References

AASHTO. (American Association of State Highway and Transportation Officials). 2018. *Standard specification for plain and laminated elastomeric bridge bearings*. Washington, DC.

Ahmadi Soleimani, S., D. Konstantinidis, and G. P. Balomenos. 2020. "Vision-Based Quality Control Testing of Elastomeric Bridge Bearings." In *Proc., Structures Congress,* 651-664. Reston, VA: ASCE.

Belivanis, K. V. 2017. "Expanding the use of elastomeric bearings for higher demand applications." Ph.D. thesis, Dept. of Civil, Architectural and Environmental Engineering, The Univ. of Texas at Austin.

Birolini, A. 2013. *Reliability engineering: theory and practice*. Springer Science & Business Media.

Bolhassani, M., S. Rajaram, A. A. Hamid, A. Kontsos, and I. Bartoli. 2016. "Damage detection of concrete masonry structures by enhancing deformation measurement using DIC." In *Proc., Nondestructive Characterization and Monitoring of Advanced Materials, Aerospace, and Civil Infrastructure 2016,* 980411. Las Vegas, Nevada: International Society for Optics and Photonics.

Born, M., and E. Wolf. 1965. *Principles of Optics, 3rd (revised) edition*. London, UK: Pergamon Press Ltd.

Chen, Z., C. Quan, F. Zhu, and X. He. 2015. "A method to transfer speckle patterns for digital image correlation." *Measurement science and technology*, 26 (9), 1-10. https://doi.org/10.1088/0957-0233/26/9/095201.

Dassault Systemes. 2019. "ABAQUS 2019 Theory manual." *Dassault Systemes Simulia Corp., Providence, Rhode Island*.

De Wilder, K., G. De Roeck, and L. Vandewalle. 2016. "The use of advanced optical measurement methods for the mechanical analysis of shear deficient prestressed concrete members." *Int. J. Concr. Struct. Mater.*, 10 (2), 189-203. https://doi.org/10.1007/s40069-016-0135-x.

Doyle, J. F. 2004. *Modern experimental stress analysis: completing the solution of partially specified problems*. Chichester, UK: John Wiley & Sons.

Dutton, M., W. A. Take, and N. A. Hoult. 2013. "Curvature monitoring of beams using digital image correlation." *J. Bridge Eng.*, 19 (3), 1-13. https://doi.org/10.1061/(ASCE)BE.1943-5592.0000538.

ECS. (European Commission for Standardization). 2005. *Structural Bearings-Part 3: Elastomeric Bearings*. Brussels, Belgium.

Fastec Imaging. 2014. *Fastec FasMotion Controller software,* San Diego, CA 92127, USA. <https://www.fastecimaging.com/>.

Forni, M., A. Martelli, and A. Dusi. "Implementation and validation of hyperelastic finite element models of high damping rubber bearings." In *Proc., Constitutive models for rubber,* 237-247. Rotterdam, Netherlands: A. A. Balkema.

Freddi, A., G. Olmi, and L. Cristofolini. 2015. *Experimental stress analysis for materials and structures*. New York, US: Springer.

Ghorbani, R., F. Matta, and M. A. Sutton. 2015. "Full-field deformation measurement and crack mapping on confined masonry walls using digital image correlation." *Exp. Mech.*, 55 (1), 227-243. https://doi.org/10.1007/s11340-014-9906-y.

GOM. 2018. *Gom Correlate Professional Software,* GOM mbH, Braunschweig, Germany <http://www.gom.com/>.

Grediac, M. 2004. "The use of full-field measurement methods in composite material characterization: interest and limitations." *Composites Part A*, 35 (7-8), 751-761. https://doi.org/10.1016/j.compositesa.2004.01.019.

Hartley, R. I., and P. Sturm. 1997. "Triangulation." *Comput. Vision Image Understanding*, 68 (2), 146-157. https://doi.org/10.1006/cviu.1997.0547.

Iadicola, M. A. 2012. *Digital image correlation measurements during gusset plate connection testing to structural failure*. *Report NIST Technical Note 1752*, National Institute of Standards and Technology (NIST), U.S. Department of Commerce.

IO Industries. 2016. *DVR Express CoreView.* 15940 Robin's Hill Rd, London, Ontario, CANADA, <http://www.ioindustries.com/core2max.html>.

Kelly, J. M., and D. Konstantinidis. 2009. "Effect of friction on unbonded elastomeric bearings." *J. Eng. Mech.*, 135 (9), 953-960. https://doi.org/10.1061/(ASCE)EM.1943-7889.0000019.

Kelly, J. M., and D. Konstantinidis. 2011. *Mechanics of rubber bearings for seismic and vibration isolation*. Chichester, UK: John Wiley & Sons.

Kelly, J. M., and N. C. Van Engelen. 2015. *Single series solution for the rectangular fiber-reinforced elastomeric isolator compression modulus*. *Report PEER 2015/03*, Pacific Earthquake Engineering Research (PEER) Center, University of California, Berkeley.

Konstantinidis, D., J. M. Kelly, and N. Makris. 2008. *Experimental investigation on the seismic response of bridge bearings*. *Report EERC-2008/02*, Earthquake Engineering Research Center, University of California, Berkeley.

Konstantinidis, D., and S. R. Moghadam. 2016. "Compression of unbonded rubber layers taking into account bulk compressibility and contact slip at the supports." *Int. J. Solids. Struct.*, 87, 206-221. http://dx.doi.org/10.1016/j.ijsolstr.2016.02.008.

Lane, C., R. L. Burguete, and A. Shterenlikht. 2008. "An objective criterion for the selection of an optimum DIC pattern and subset size." In *Proc., XIth international congress and exposition,* 1-9. Bethel, Conn: Society for Experimental Mechanics, Inc.

Mayinger, F. 2013. *Optical measurements: techniques and applications*. New York, US: Springer Science & Business Media.

McGinnis, M. J., B. Smith, M. Holloman, M. Lisk, A. O'Donnell, and Y. C. Kurama. 2012. "3-D digital image correlation—an underused asset for structural testing." In *Proc., Structures Congress,* 1958-1969. Chicago, Ilinois.

Moghadam, S. R., and D. Konstantinidis. 2017a. "Finite element study of the effect of support rotation on the horizontal behavior of elastomeric bearings." *Compos. Struct.*, 163, 474-490. http://dx.doi.org/10.1016/j.compstruct.2016.12.013.

Mojsilović, N., and A. H. Salmanpour. 2016. "Masonry walls subjected to in-plane cyclic loading: application of digital image correlation for deformation field measurement." *International Journal of Masonry Research and Innovation*, 1 (2), 165-187. http://dx.doi.org/10.1504/IJMRI.2016.077473.

Muscarella, J. V., and J. Yura. 1995. "An experimental study of elastomeric bridge bearings with design recommendations." Ph.D. thesis, Center for Transportation Research, The University of Texas at Austin.

OPSS. (Ontario Provincial Standard Specification). 2017. *Material specification for bearings - elastomeric plain and steel laminated*.

Orteu, J.-J. 2009. "3-D computer vision in experimental mechanics." *Opt. Lasers Eng.*, 47 (3-4), 282-291. http://dx.doi.org/10.1016/j.optlaseng.2007.11.009.

Osgooei, P. M., M. J. Tait, and D. Konstantinidis. 2014. "Three-dimensional finite element analysis of circular fiber-reinforced elastomeric bearings under compression." *Compos. Struct.*, 108, 191-204. http://dx.doi.org/10.1016/j.compstruct.2013.09.008.

Pan, B., K. Qian, H. Xie, and A. Asundi. 2009. "Two-dimensional digital image correlation for in-plane displacement and strain measurement: a review." *Meas. Sci. Technol.*, 20 (6), 062001. https://doi.org/10.1088/0957-0233/20/6/062001.

Roeder, C. W., J. F. Stanton, and T. Feller. 1989. *Low temperature behavior and acceptance criteria for elastomeric bridge bearings*. Washington, DC: Transportation Research Board.

Sieffert, Y., F. Vieux-Champagne, S. Grange, P. Garnier, J. Duccini, and L. Daudeville. 2016. "Full-field measurement with a digital image correlation analysis of a shake table test on a timber-framed structure filled with stones and earth." *Eng. Struct.*, 123, 451-472. http://dx.doi.org/10.1016/j.engstruct.2016.06.009.

Sokoli, D., W. Shekarchi, E. Buenrostro, and W. M. Ghannoum. 2014. "Advancing behavioral understanding and damage evaluation of concrete members using high-

resolution digital image correlation data." *Earthquakes Struct.*, 7 (5), 609-626. http://dx.doi.org/10.12989/eas.2014.7.5.609.

Stanton, J. F., C. W. Roeder, P. Mackenzie-Helnwein, C. White, C. Kuester, and B. Craig. 2008. *Rotation limits for elastomeric bearings*. *Report 596*, National Cooperative Highway Research Program (NCHRP), Washington, DC: Transportation Research Board.

Sun, C. 2015. "Material study of the steel reinforced elastomeric bridge bearings." Ph.D. thesis, Dept. of Civil, Architectural and Environmental Engineering, The Univ. of Texas at Austin.

Sutton, M., W. Wolters, W. Peters, W. Ranson, and S. McNeill. 1983. "Determination of displacements using an improved digital correlation method." *Image Vision Comput.*, 1 (3), 133-139. https://doi.org/10.1016/0262-8856(83)90064-1.

Sutton, M. A. 2013. "Computer vision-based, noncontacting deformation measurements in mechanics: a generational transformation." *Appl. Mech. Rev.*, 65 (5), 050802 (050823 pages). https://doi.org/10.1115/1.4024984.

Sutton, M. A., H. Schreier, and J.-J. Orteu. 2009. *Image correlation for shape, motion and deformation measurements*. New York, US: Springer.

Triggs, B., P. F. McLauchlan, R. I. Hartley, and A. W. Fitzgibbon. 1999. "Bundle adjustment—a modern synthesis." *International workshop on vision algorithms*, 298-372.

Yakut, A., and J. A. Yura. 2002. "Parameters influencing performance of elastomeric bearings at low temperatures." *J. Struct. Eng.*, 128 (8), 986-994. https://doi.org/10.1061/(ASCE)0733-9445(2002)128:8(986).

Yeoh, O. H. 1993. "Some forms of the strain energy function for rubber." *Rubber Chemistry and technology*, 66 (5), 754-771. https://doi.org/10.5254/1.3538343.

Yura, J., A. Kumar, A. Yakut, C. Topkaya, E. Becker, and J. Collingwood. 2001. *Elastomeric bridge bearings: Recommended test methods*. *Report NCHRP 449*, National Cooperative Highway Research Program (NCHRP), Washington, DC: Transportation Research Board.

3 Effect of Manufacturing Imperfections on the Service-level Performance of Elastomeric Bridge Bearings

Soleimani S.A., Konstantinidis D., and Balomenos G.P. (2021). Effect of Manufacturing Imperfections on the Service-level Performance of Elastomeric Bridge Bearings. Accepted for publication in the *Journal of Structural Engineering* (in-press as of the submission date of this thesis).

Abstract

During the vulcanization process of steel-laminated elastomeric bridge bearings, unavoidable flow of elastomer occurs inside the mold under high pressure and nonuniform heating. This may cause the interior steel laminates to misalign or distort in the finished bearing. There has been limited research to understand and quantify the effects of manufacturing imperfections, such as vertically shifted, rotated, and bent steel laminates, on the mechanical behavior of elastomeric bearings. This paper presents a finite element investigation on the effects of manufacturing imperfections on the performance of elastomeric bridge bearings subjected to service-level loads. It is observed that such imperfections have a negligible effect on the maximum shear strain induced in the elastomer. The strain hardening behavior of the elastomer under relatively large shear strains limits the maximum shear strains to values lower than those predicted by the pressure solution. In one cycle of loading, the vertical deflection of bearings is affected slightly by these imperfections. However, manufacturing imperfections can increase the tensile stresses in the steel laminates causing plastic damage. The spread of plastic damage in the steel laminates with repeated cycling may affect the long-term performance of the bearings.

Keywords: Laminated Elastomeric Bridge Bearings, Manufacturing Imperfections, Shear Strain, Plastic Damage, Vertical Deflection, Finite Element Analysis

3.1 Introduction

Elastomeric bridge bearings were first manufactured commercially in the late 1950s and are now the most widely used bridge bearings in areas of low-to-moderate seismicity (Stanton et al. 2008). They are composed of horizontal layers of either natural rubber or neoprene and steel reinforcement laminates bonded together and surrounded by a protective elastomer cover all around. The role of these bearings is to accommodate translations and rotations mainly caused by gravity and wind loads, daily traffic, creep, thermal expansion and contraction of the superstructure, and beam rotation. Elastomeric bridge bearings are sometimes classified as *bonded* (with vulcanized end plates) and *unbonded* (without vulcanized end plates). In bonded bearings, the end plates are bolted to the substructure/superstructure, while unbonded bearings are held in place by the frictional resistance that develops along their top and bottom surfaces.

The poor performance or failure of elastomeric bearings can cause damage to the bridge superstructure and substructure. For instance, excessive vertical deflection of bearings may damage deck joints and seals, increase the impact loading from traffic (Roeder et al. 1989), and cause differential deflection of the superstructure and excessive stresses in girders (Yura et al. 2001). Elastomeric bearings can fail as a result of debonding of the elastomer from the steel laminates, fatigue of the elastomer, yielding or rupture of the steel laminates, and buckling of the bearing (Stanton and Roeder 1982). The most common mode of failure in these bearings is shear delamination, i.e., the propagation of horizontal shear cracks at steel–elastomer interfaces (Stanton et al. 2008). This failure mode results in a severe reduction of the bearing's vertical stiffness, unpredictable horizontal forces, and serious degradation of its serviceability. Kumar (2001) and Khaloo et al. (2020) noted that the steel laminates in bearings subjected to shear loading experience flexural deformations, which may induce excessive tensile stresses in the steel laminates. Kalfas et al. (2020) observed laminate yielding and consequent permanent deformations in bearings subjected to shear and rotation.

Well-designed and manufactured elastomeric bridge bearings are expected to perform satisfactorily throughout the lifespan of a bridge. However, during vulcanization, the unavoidable flow of elastomer under high pressure and temperature, together with the malfunction of seats when used by the manufacturer (to prevent the movements of laminates inside the mold), may lead to misaligned or distorted laminates in the finished bearing (Kumar 2001). Such manufacturing imperfections alter stress and strain distributions and may trigger the aforementioned modes of failure and poor performance of elastomeric bearings (Yura et al. 2001).

Studies on the effects of imperfections in rubber bearings are scarce. To the best of the authors' knowledge, the finite element (FE) studies by Kumar (2001) and Belivanis (2017) are the only works on the subject. Kumar (2001) investigated the effects of horizontal, vertical, and rotational misalignments of the steel laminates on the stiffness properties and stress and strain distributions in bonded bearings. They concluded that the horizontal misalignment of laminates has a negligible influence on the bearing performance. They also proposed a simplified interaction equation that defines acceptable imperfection tolerances for steel laminates such that the performance and structural integrity of the bearing is not compromised. The equation proposed by Kumar (2001) has been adopted by AASHTO (2018) as an acceptance criterion for laminate tolerances. Belivanis (2017) numerically investigated the effect of bent steel laminates on the vertical stiffness of a specific bearing and noted that this imperfection can be one of the main reasons for the discrepancy between the experimental measurements and theoretical predictions of the vertical stiffness.

The loads and deformations that Kumar (2001) applied on the examined bearings (i.e., compression, rotation, and shear) were relatively low compared to what current bridge specifications (e.g., AASHTO (2017) and CSA (2019)) permit as the maximum service-level loads in the design of elastomeric bridge bearings. AASHTO's (2011) design Method B for elastomeric bearings specifies that the maximum shear strain induced in the elastomer by static and cyclic loads, with the latter multiplied by an amplification factor, should be

limited to 5. FE analyses under such relatively large deformations require FE models with highly refined meshes to control mesh distortion and obtain reliable results. Also, the shear strain referred to for the design of elastomeric bearings, i.e., twice the shear component of the Green-Lagrange strain tensor, was not investigated by Kumar (2001). Some other important gaps with regards to imperfections include their effects on the performance of unbonded bearings, especially with bent steel laminates and bearings with relatively thin steel laminates (e.g., 2-mm-thick laminates).

This paper presents a numerical study on the effects of manufacturing imperfections on the performance of bearings under service-level conditions. Specifically, the effects of vertically shifted, rotated, and bent steel laminates are investigated. Three-dimensional finite element analyses (FEA) are conducted on models of bearings with and without imperfections. The study considers both bonded and unbonded bearings with various characteristics in terms of shape factor [defined for an elastomer layer as the ratio of loaded plan area to area free to bulge], steel laminate thicknesses, and elastomer material properties. Initially, stress and strain distributions are studied for bearings subjected to combined actions that include maximum allowable compression, rotation, and shear displacement, under service-level conditions. The study evaluates performance based on the shear strains induced in the elastomer, the tensile stresses in the steel laminates, and the bond stresses at the steel–elastomer interfaces. Finally, the vertical stiffness and deflection of bearings with and without imperfections are assessed.

3.2 Analysis Approach and Considerations

This section provides the details of the examined bearings related to geometry, imperfections, material properties, and loading demands.

3.2.1 Geometry of Bearings Without Imperfections

Table 3.1 lists the geometric characteristics of the examined bearings without imperfections. They are based on bearings used in the Province of Ontario, Canada, and were provided by the Ministry of Transportation of Ontario (MTO). Existing elastomeric

bridge bearings in this region vary between having three and eight steel laminates. The shape factor usually lies in the 6 to 12 range but is typically closer to 6. In Table 3.1, bearings B1 to B7 do not have imperfections and were used as benchmarks for comparing the effects of imperfections introduced in the next section. Bearings B1, B2, and B3 differ only in terms of the steel laminate thickness. The minimum thickness required by AASHTO (2017), ECS (2005), and CSA (2019) is 1.6 mm, 2 mm, and 3 mm, respectively. AASHTO (2017) also specifies additional formulas expressing the minimum thickness as a function of steel yield stress and fatigue threshold, with specific safety factors, to prevent yielding and fatigue failure, respectively. Such formulas are based on an analytical solution expressing the maximum tensile stress induced in inextensible steel laminates of a thin strip bearing under compression (Stanton and Roeder 1982). Bearings B1, B2, and B3 are used in this study to investigate the effects of imperfections on the stress and strain distributions. The reason for selecting these rather small bearings for this purpose is that such FE investigations require models with very fine meshes, which increases the computational cost. In addition, bearings B1, B2, and B3 have three steel laminates, which suffice for introducing the imperfection configurations mentioned earlier. Finally, bearings B1, B2, and B3 have a relatively low shape factor, and thus represent most bearings in use. Bearings B1, B4, B5, B6, and B7 serve as benchmarks to investigate the effects of imperfections on the vertical stiffnesses and deflections of bearings. These designs cover a wide range of characteristics, including low shape factors (all except B5), high shape factors (B5), thick bearings (B7), and thin bearings (B1 or B5).

Table 3.1 Geometric parameters of the bearings without manufacturing imperfections (unit: mm)

Bearing	Plan dimensions	Total thickness	Rubber layer thickness	Steel laminate thickness	Number of steel laminates	Cover rubber layer thickness	Side cover thickness	Shape factor
B1	350×250	45	12	3	3	6	6	6.1
B2	350×250	42	12	2	3	6	6	6.1
B3	350×250	48	12	4	3	6	6	6.1
B4	350×250	128	12	4	8	6	6	6.1
B5	350×250	30	6.5	3	3	4	6	11.2
B6	700×450	70	23	4	3	6	6	5.9
B7	700×450	205	23	4	8	6	6	5.9

3.2.2 Imperfection Configurations and Considered Intensities

The MTO completes quality assurance testing of one bearing per lot of laminated elastomeric bearings in a bridge (representing up to 20 bearings in a bridge), including destructive testing to measure the exact manufactured internal geometry of the steel lamina and elastomer layers. An analysis of 50 destructive test reports on manufactured elastomeric bridge bearings (provided by the MTO to illustrate imperfections in bearings over the last decade) identified four types of imperfections. The first three involved misalignment of the steel laminates, specifically, horizontally shifted, vertically shifted, and rotated laminates. The fourth involved distortion, specifically, bent laminates. This study investigates the effects of the following three imperfection types: vertically shifted, rotated, and bent laminates. Horizontally shifted steel laminates are not considered because this imperfection type was found by Yura et al. (2001) to have a negligible effect on the performance of elastomeric bridge bearings. Figure 3.1 shows the photographs of cut bearings (extracted from the MTO destructive test reports) having three different imperfection types examined in this study.

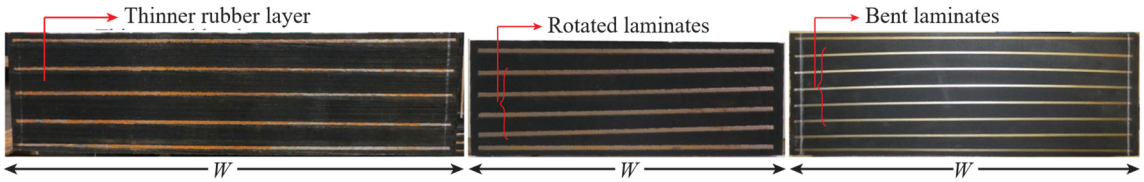

(a) $L \times W \times H$=500×400×100 mm (b) $L \times W \times H$=320×250×90 mm (c) $L \times W \times H$=400×300×100 mm

Figure 3.1 Photographs of cut elastomeric bearings with imperfections; (a) vertically misaligned, (b) rotated, and (c) bent steel laminates [reproduced with permission from Ministry of Transportation of Ontario]

The reports of bearings with imperfections indicated that the top and bottom steel laminates are usually less misaligned or distorted compared to other laminates, while the rest of the laminates were observed to experience the same type of imperfection and with approximately the same intensity. Because of these observations, in the present study, rotated or bent laminates are introduced simultaneously in all the steel laminates except the top and bottom ones. The vertical shift and rotation of steel laminates are denoted by v and θ, respectively, as shown in Figure 3.2(a),(b) only for a single laminate. Based on

observations from the MTO reports and from Belivanis (2017), the shape of bent steel laminates can be approximated well by a half-sine curve with amplitude ρ, as shown in Figure 3.2 (c) only for a single laminate. The amplitude of the imperfection is constant for all X. Because of the directions of loading and the fact that the long side of the bearings, L, is parallel to the Z-axis, the largest lateral bulging of the rubber layers always occurs on the surfaces with normal pointing in the positive X-axis. The lateral bulging of a rubber layer is also proportional to its thickness. The imperfections are considered such that the thickness increase of one interior rubber layer (with respect to its thickness in bearings without imperfections) occurs close to the side of bearings with the positive surface normal in X-axis. This would maximize the peak stress and strain demands on the steel reinforcement and rubber.

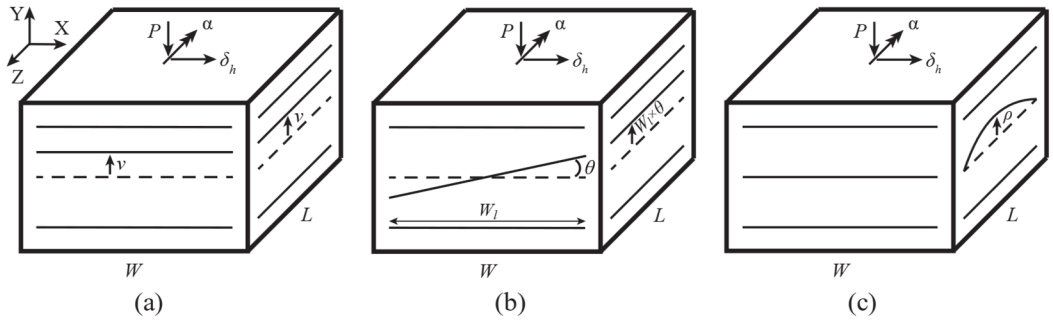

Figure 3.2 Imperfection configurations; (a) vertical misalignment, (b) rotational misalignment, and (c) bending of interior steel laminates in three-laminate bearing

The maximum values of v, θ, and ρ recorded in the MTO reports were approximately 3.5 mm, 0.03 rad, and 4.5 mm, which are close to those observed by Yura et al. (2001). Thus, this study uses these values for the bearings with imperfections. Table 3.2 lists the configurations of the imperfections considered. Stresses and strains are studied in the bearings with two interior rubber layers for the first three configurations in Table 3.2, i.e., v, θ, and ρ, while the vertical stiffness and deflection of bearings are assessed in both two- and seven-interior-rubber-layer bearings with all imperfection configurations listed in Table 3.2. The imperfection configuration labels v, θ, ρ, $\theta\theta$, and $\rho\rho$ are used later as part of the nomenclature used to identify FE models with imperfections. The letters v, θ, ρ, $\theta\theta$, and $\rho\rho$ are also used as variables to denote the intensities of imperfections. For instance, $\theta\theta$ =

0.03 denotes the imperfection configuration in which all steel laminates except the top and bottom ones have the rotational misalignment of 0.03 rad.

Table 3.2 Configurations of examined imperfections and assessment goals

Imperfection Configuration	Misaligned or deformed laminates	Assessment goals
v	One interior laminate	Stress, strain, stiffness, and deflection
θ	One interior laminate	Stress, strain, stiffness, and deflection
ρ	One interior laminate	Stress, strain, stiffness, and deflection
$\theta\theta$	All laminates except the top and bottom	Stiffness and deflection
$\rho\rho$	All laminates except the top and bottom	Stiffness and deflection

3.2.3 Material Properties of Elastomer and Steel Reinforcement

Table 3.3 shows material properties of the elastomer types, i.e., natural rubber (Sokoli et al.) and neoprene (NEO), and the steel considered in this study. The NR was tested at the Akron Rubber Development Laboratory, Barberton, OH. Simple shear and volumetric compression test results are shown in Figure 3.3(a,b). NEO refers to the neoprene used by Kumar (2001) [labelled "CR70" therein]. Simple shear test results from Kumar (2001) are also shown in Figure 3.3(a). The graph indicates that the NEO is a high-shear-modulus elastomer compared to the NR, and it has a high rate of strain hardening. For the steel reinforcement, steel grade A36 is selected with data for the uniaxial stress–strain curve from El-Reedy (2016) [see Figure 3.3(c)].

Table 3.3 Material properties of the natural rubber, neoprene, and steel reinforcement

Material	Reference	Property	Symbol	Value
Natural rubber [NR]	This study	Shear modulus	G_{NR}	0.996 MPa
		Poisson's ratio	v_{NR}	0.4996
Neoprene [NEO]	(Kumar 2001)	Shear modulus	G_{NEO}	1.38 MPa
		Poisson's ratio	v_{NEO}	0.4998
Steel reinforcement	(El-Reedy 2016)	Young's modulus	E_s	200 GPa
		Yield stress	σ_{ys}	248 MPa
		Poisson's ratio	v_s	0.3

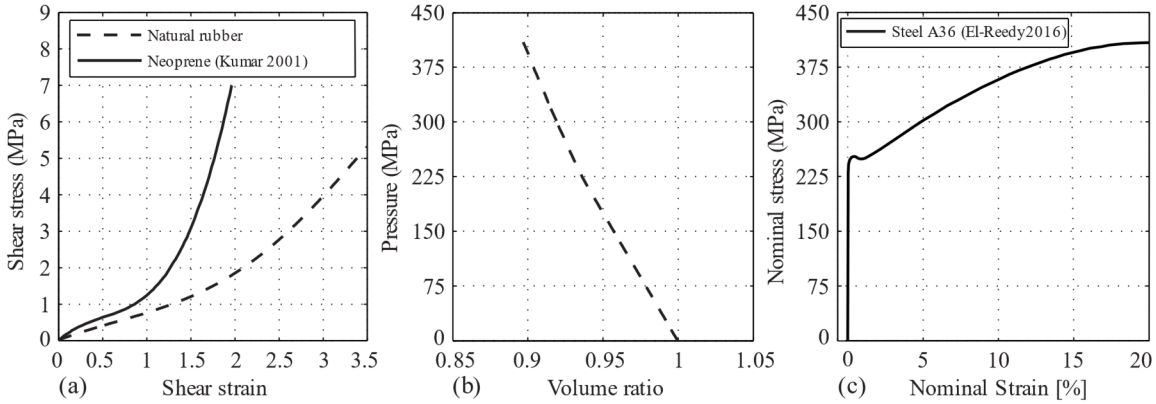

Figure 3.3 (a) Simple shear test data of the natural rubber and neoprene, (b) Volumetric compression test data of natural rubber, and (c) Steel grade A36 stress–strain data

3.2.4 Loading Demands on the Considered Bearings

The examined bearings are subjected to axial load, support rotation, and shear displacement. As mentioned earlier, according to AASHTO's Method B (2017), the maximum effective shear strain at the steel–elastomer interfaces of the bearing under combined service loads should be limited to 5, i.e.,

$$(\gamma_{a,\,st} + \gamma_{r,\,st} + \gamma_{s,\,st}) + 1.75 \times (\gamma_{a,\,cy} + \gamma_{r,\,cy} + \gamma_{s,\,cy}) \leq 5 \qquad (3.1)$$

where $\gamma_{a,\,st}, \gamma_{r,\,st}, \gamma_{s,\,st}$ = the maximum interfacial shear strains caused by static axial load, static rotation, and static shear displacement, respectively; Shear strains $\gamma_{a,\,cy}, \gamma_{r,\,cy}, \gamma_{s,\,cy}$ = the maximum interfacial shear strains caused by cyclic axial load, cyclic rotation, and cyclic shear displacement, respectively. The amplification factor of 1.75 for the cyclic strains is based on experimental tests by Stanton et al. (2008), which revealed that more damaging effects are caused by cyclic loads on the elastomer-to-steel bond compared to static loads. The shear strain limit of 5 is also based on experimental tests by Stanton et al. (2008) and represents the effective shear strain (as predicted by analytical solutions assuming linear theory) at which the bearings are expected to experience shear delamination at the 50-year service life of a bridge. In Eq. 3.1, the sum $\gamma_{a,\,st} + \gamma_{r,\,st} + \gamma_{s,\,st}$ will be referred to as γ_{st} = the maximum *static* interfacial shear strain, and the sum $\gamma_{a,\,cy} + \gamma_{r,\,cy} + \gamma_{s,\,cy}$ will be referred to as γ_{cy} = the maximum *cyclic* interfacial shear strain. Then,

$\gamma_{st} + \gamma_{cy}$ gives the maximum *combined* interfacial shear strain (referred to as γ_{st+cy}), and $\gamma_{st} + 1.75\gamma_{cy}$ (i.e., the left-hand side of Eq. 3.1) gives the maximum *effective* interfacial shear strain (referred to as γ_{eff}).

In this study, the maximum effective shear strain demand is assumed to be 5, and the following assumptions are adopted to determine the loading demands. The only cyclic strains considered are those caused by traffic, as suggested by AASHTO (2017). Shear strains $\gamma_{a,\,cy}$ and $\gamma_{r,\,cy}$ are assumed to be caused by truck passage with $\gamma_{a,\,cy}/\gamma_{r,\,cy} = 8.8$, which lies within $5 \leq \gamma_{a,\,cy}/\gamma_{r,\,cy} \leq 10$, the range reported by Stanton et al. (2008). The value of $\gamma_{r,\,st}$ corresponds to a girder rotation of 0.006 rad due to thermal gradient and beam misalignment (Stanton et al. 2008).

The static and cyclic axial loads are assumed to cause a total shear strain of 2.95 (meeting the AASHTO (2017) limit for the shear strain caused by axial loads) with realistic contributions of 1.8 and 1.15 for $\gamma_{a,\,st}$ and $\gamma_{a,\,cy}$, respectively, according to illustrative examples in Stanton et al. (2008), NYSDOT (2010), and CDOT (2018). Shear strain $\gamma_{s,\,st}$ is assumed to be induced by temperature variations and taken as 0.5, which is the maximum value allowed by AASHTO (2017). Shear strain $\gamma_{s,\,cy}$ due to traffic loading is too small to be of much consequence (Stanton et al. 2008) and thus assumed to be zero in this study. Table 3.4 lists the static and cyclic axial load, rotation, and shear displacement applied to bearings B1, B2, and B3.

Table 3.4 Service-level demands on bearings B1, B2, and B3 according to the elastomer type

Elastomer type	Component	Contribution	
		Static	Cyclic
NR	Average vertical stress	7.8 MPa ($\gamma_{a,\,st}$ = 1.8)	5.0 MPa ($\gamma_{a,\,cy}$ = 1.15)
	Rotation	0.006 rad ($\gamma_{r,\,st}$ = 0.44)	0.0017 ($\gamma_{r,\,cy}$ = 0.13)
	Shear displacement	18 mm ($\gamma_{s,\,st}$ = 0.5)	0.0 mm
NEO	Average vertical stress	10.3 MPa ($\gamma_{a,\,st}$ = 1.8)	6.5 MPa ($\gamma_{a,\,cy}$ = 1.15)
	Rotation	0.006 rad ($\gamma_{r,\,st}$ = 0.44)	0.0017 ($\gamma_{r,\,cy}$ = 0.13)
	Shear displacement	18 mm ($\gamma_{s,\,st}$ = 0.5)	0.0 mm

Table 3.5 lists the static and cyclic axial loads applied to bearings B4, B5, B6, and B7 for assessing their vertical deflections. It is noted that these applied loads were backcalculated from the corresponding target strain demands using relevant analytical solutions in AASHTO (2017). The bearings are assumed to be oriented such that the longer sides of the bearings are parallel to the bridge's transverse axis (i.e., Z-axis in Figure 3.2), and rotation α is applied about the bridge's transverse axis. The shear displacement is applied along the shorter sides of the bearings, i.e., the X-axis in Figure 3.2.

Table 3.5 Axial loads (presented as average vertical stress) applied on natural rubber bearings B4, B5, B6, and B7 for vertical deflection assessment

Bearing	Component	Contribution	
		Static	Cyclic
B4	Average vertical stress	7.8 MPa ($\gamma_{a,\,st}$ = 1.8)	5.0 MPa ($\gamma_{a,\,cy}$ = 1.15)
B5	Average vertical stress	14.4 MPa ($\gamma_{a,\,st}$ = 1.8)	9.2 MPa ($\gamma_{a,\,cy}$ = 1.15)
B6 or B7	Average vertical stress	7.6 MPa ($\gamma_{a,\,st}$ = 1.8)	4.9 MPa ($\gamma_{a,\,cy}$ = 1.15)

3.2.5 Bearings Considered

The examined bearings feature different geometric characteristics, elastomer type, contact conditions, and steel laminate thicknesses. The study focuses on the stresses and strains induced in the elastomer and steel laminates, and the vertical stiffness and deflection of the bearings. Different bearings are analyzed depending on what aspect of behavior is of interest. The geometry of bearing B1 is chosen to assess the effect of each imperfection configuration on the stresses and strains in the elastomer. Table 3.6 lists the bearings considered for this behavior aspect. They include different combinations of imperfection configuration, contact condition, and elastomer type. The label for a bearing consists of either three or four groups of alphanumeric characters: the first two characters identify the bearing geometry, the third and fourth the elastomer type, the fifth the contact condition, and the last two or three the imperfection configuration (if any) and its intensity. For example, B1NRBθ3 denotes B1 geometry, natural rubber, bonded conditions, and rotation of one laminate by 0.03 rad.

Table 3.6 Bearings considered for assessing stresses and strains induced in their elastomer

Category	Bearing	Bearing geometry	Elastomer type	Contact condition	Imperfection configuration	Imperfection intensity
Bearings without imperfections	B1NRB	B1	NR	Bonded (B)	——	——
	B1NRU	B1	NR	Unbonded (U)	——	——
	B1NEU	B1	NEO	Unbonded (U)	——	——
Bearings with imperfections	B1NRBθ3	B1	NR	Bonded (B)	θ	0.03 rad
	B1NRUθ3	B1	NR	Unbonded (U)	θ	0.03 rad
	B1NRBρ45	B1	NR	Bonded (B)	ρ	4.5 mm
	B1NRUρ45	B1	NR	Unbonded (U)	ρ	4.5 mm
	B1NRBν35	B1	NR	Bonded (B)	ν	3.5 mm
	B1NRUν35	B1	NR	Unbonded (U)	ν	3.5 mm
	B1NEUν35	B1	NEO	Unbonded (U)	ν	3.5 mm

The geometries of bearings B1, B2, and B3 are examined to assess the extent of damage in misaligned or distorted steel laminates. Table 3.7 lists the bearings considered to study this aspect of behavior, and they include the bearings listed in Table 3.6. They cover different combinations of steel laminate thickness, imperfection configuration, contact condition, and elastomer type.

Table 3.7 Bearings considered for assessing stresses induced in their steel laminates

Category	Bearing	Bearing geometry	Elastomer type	Contact condition	Imperfection configuration	Imperfection intensity
Bearings without imperfections	B1NRB	B1	NR	Bonded (B)	——	——
	B1NRU	B1	NR	Unbonded (U)	——	——
	B1NEU	B1	NEO	Unbonded (U)	——	——
	B2NRU	B2	NR	Unbonded (U)	——	——
	B3NRU	B3	NR	Unbonded (U)	——	——
Bearings with imperfections	B1NRBθ3	B1	NR	Bonded (B)	θ	0.03 rad
	B1NRUθ3	B1	NR	Unbonded (U)	θ	0.03 rad
	B1NRBρ45	B1	NR	Bonded (B)	ρ	4.5 mm
	B1NRUρ45	B1	NR	Unbonded (U)	ρ	4.5 mm
	B1NRBν35	B1	NR	Bonded (B)	ν	3.5 mm
	B1NRUν35	B1	NR	Unbonded (U)	ν	3.5 mm
	B1NEUν35	B1	NEO	Unbonded (U)	ν	3.5 mm
	B1NEUθ3	B1	NEO	Unbonded (U)	θ	0.03 rad
	B1NEUρ45	B1	NEO	Unbonded (U)	ρ	4.5 mm
	B2NRUν35	B2	NR	Unbonded (U)	ν	3.5 mm
	B3NRUν35	B3	NR	Unbonded (U)	ν	3.5 mm

Table 3.8 lists the bearings used to investigate the effect of different imperfections on the vertical stiffness. All bearings for this purpose are unbonded natural rubber bearings, and

the label for each bearing consists of three groups of alphanumeric characters: the first group identifies the bearing geometry based on its long side, the second the shape factor, and the third the number of steel laminates, with "A" indicating whether all (vs a single) laminates except the top and bottom ones have imperfections. For instance, 35-6-8A denotes 350 mm length, shape factor of 6, and 8 steel laminates all (except the top and bottom) with imperfections. According to Table 3.2 and Table 3.8, only one steel laminate of bearings 35-6-3, 35-11-3, 35-6-8, 70-6-3, and 70-6-8 has an imperfection, the configuration and intensity of which are denoted with one of the variables v, θ, and ρ. Similarly, the variables $\theta\theta$ and $\rho\rho$ denote the configuration and intensity of the simultaneous imperfection in six laminates (except the top and bottom ones) of bearings 35-6-8A and 70-6-8A.

Table 3.8 Bearings considered for assessing their vertical stiffnesses and deflections

Bearing	Bearing geometry	Imperfection configurations and intensities		
		1	2	3
35-6-3	B1	θ (0.0 to 0.03 rad)	ρ (0.0 to 5.0 mm)	v (0.0 to 4.0 mm)
35-11-3	B5	θ (0.0 to 0.03 rad)	ρ (0.0 to 5.0 mm)	v (0.0 to 4.0 mm)
35-6-8	B4	θ (0.0 to 0.03 rad)	ρ (0.0 to 5.0 mm)	v (0.0 to 4.0 mm)
35-6-8A	B4	$\theta\theta$ (0.0 to 0.03 rad)	$\rho\rho$ (0.0 to 5.0 mm)	——
70-6-3	B6	θ (0.0 to 0.03 rad)	ρ (0.0 to 5.0 mm)	v (0.0 to 4.0 mm)
70-6-8A	B7	$\theta\theta$ (0.0 to 0.03 rad)	$\rho\rho$ (0.0 to 5.0 mm)	——
70-6-8	B7	——	——	v (0.0 to 4.0 mm)

3.3 Finite Element Modeling

The bearing FE models are developed and analyzed in the software Abaqus (Dassault Systemes 2019) using the Abaqus Python Development Environment (PDE). Abaqus PDE allows combining its Graphical User Interface functionality with the Python programming language. For example, the Abaqus PDE was used for the FE model of flat-slabs susceptible to punching shear (Balomenos et al. 2015) and for the FE model of nuclear containment wall segments susceptible to prestressing losses (Balomenos and Pandey 2017). In the present study, Abaqus PDE enabled superefficient modeling and analysis of 97 FE models. Because of the symmetry of the problem, only half of each bearing is

modeled, as shown in Figure 3.4(a). At nodes on the plane of symmetry, the displacement in the Z direction and rotations about the X- and Y-axes are fixed. As shown in Figure 3.4(c), the steel laminate edges are rounded, with a radius of 0.5 mm, which is representative of the laminates in bearings tested by Ahmadi Soleimani et al. (2020) and consistent with specification requirements that the steel laminates be deburred.

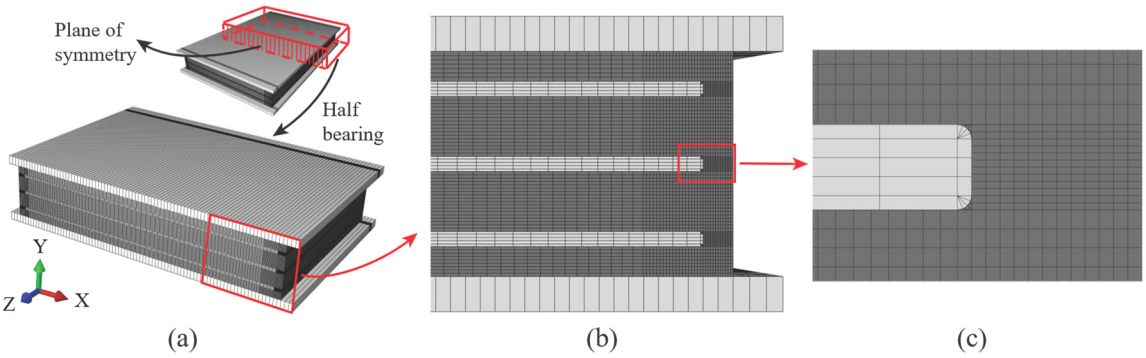

Figure 3.4 (a) 3D mesh of half bearing B1NRB, (b) close-up of the right side of the bearing on the plane of symmetry, and (c) mesh detail of the steel laminate ends

A sensitivity analysis was conducted with respect to convergence rate and computational time to identify the most suitable element types and mesh size in different regions of the bearings. The quality of the deformed mesh, the shear strains in the elastomer, and tensile stresses in the steel laminates were evaluated for this purpose. Based on the results, six-node triangular prism, hybrid elements (C3D6H) were selected to discretize the small elastomer cover in contact with the laminate edges (Figure 3.4(c)) and 8-node linear brick, hybrid, reduced integration elements with hourglass control (C3D8RH) for the remaining elastomer. The hybrid-type elements are necessary to avoid ill-conditioning and volumetric-mesh-locking issues in nearly incompressible rubber elements (Moghadam and Konstantinidis 2017a). The reduced integration elements with the hourglass control decrease the computational time while preventing the hour-glassing mode of distortion. Similarly, six-node linear triangular prism elements (C3D6) and 8-node linear brick, reduced integration, hourglass control elements (C3D8R) are used to mesh small steel regions close to rounded-shape edges of the laminate (Figure 3.4(c)) and the remaining steel components, respectively. The mesh in steel and elastomer components is refined

closer to the bearing sides due to the higher distortion in those regions compared to the middle regions of the bearings. Mesh convergence was considered when the relative difference of the peak of the responses of interest became less than 1% between two consecutive mesh refinements. All in all, steel laminates are discretized using 60, 50, and 5 elements along the X, Z, and Y axes, respectively; interior rubber layers and cover layers at top and bottom are meshed with 120 and 80 elements along the X and Z axes, respectively; the elastomer element size along the bearing height ranges from 0.43 mm to the maximum of 0.6 mm. This refined mesh resulted in models with a number of elements varying from 0.8 to 2.6 million, depending on the bearing geometry.

The top and bottom plates in the models represent the bridge girder and abutments or piers in unbonded bearings and the end plates in bonded bearings. In either case, the plates are modeled as rigid blocks in Abaqus (Dassault Systemes 2019). In unbonded bearings, the frictional contact between the bearing and its supports is defined using *Coulomb friction* with a penalty-based contact method. A Coulomb model used to describe the frictional behavior of concrete-to-rubber or steel-to-rubber (i.e., a hard material in contact with a soft material) is perhaps not the most accurate representation of the true mechanical behavior (Konstantinidis et al. 2008), but it is simple to implement in FEA and it provides a reasonable representation of the friction behavior at the bearing-support interfaces (Han 2016; Huang et al. 2018; Khaloo et al. 2020; Ahmadi Soleimani et al. 2021). The adopted penalty-based contact constraint enforcement method is chosen because of its increased numerical stability for the range of contact pressures that exists in bearings. Friction coefficient values ranging from 0.2 to 0.4 are suggested for elastomer–steel interfaces (Caltrans 1994; Muscarella and Yura 1995; Yakut and Yura 2002). The response of the unbonded bearings considered in this study is found to be insensitive within the 0.2 to 0.4 friction coefficient range under the applied shear deformations; therefore, the average value of 0.3 is considered in the simulations. For other steel-elastomer interfaces (e.g., interior steel-elastomer interfaces), the tangential and normal interactions are modeled using “rough” friction formulation and “hard contact”, respectively. Such a definition of the

contact interaction works well in Abaqus (Dassault Systemes 2019) for simulating the bond at these interfaces.

The Yeoh hyperelastic material model is used to describe the elastomer because of its ability to accurately characterize hardening under large shear strains (Sun 2015; Van Engelen et al. 2015; Moghadam and Konstantinidis 2017a). The reader is referred to Moghadam and Konstantinidis (2017a) for the form of the Yeoh model used. The Yeoh parameters $\{C_{10}, C_{20}, C_{10}\}$ and $\{D_1, D_2, D_3\}$ are $\{350, 15.7, 0.07\}\times10^{-3}$ MPa and $\{0.578, 0.354, 156\}\times10^{-3}$ MPa^{-1} for the natural rubber and $\{527, 31.3, 23.2\}\times10^{-3}$ MPa and $\{1.00, 0, 0\}\times10^{-3}$ MPa^{-1} for the neoprene. The A36 steel is modeled as an isotropic, elastic–plastic material using the stress–strain relationship in Figure 3.3(c).

The analyses are performed monotonically in three stages: first, the static components of the axial loads and rotations, representing the permanent loads and deformations, are applied; second, the static shear displacement, caused by temperature changes, is applied; third, the cyclic components of axial loads and rotations, caused by traffic loading, are applied. This sequence is meant to replicate real-world conditions. Also, it allows determining γ_{st} at the end of the second stage, and γ_{st+cy} at the end of the third stage. The difference between the two gives γ_{cy}, which then is multiplied by 1.75 and added to γ_{st} to give γ_{eff}. It is noted that the FEA include both geometric and material nonlinearities and are conducted in small increments using a Lagrangian formulation and Newton-Raphson iteration method.

3.4 General Observations on the Deformed Shapes of Bearings

This section discusses the deformation patterns in bearings with and without imperfections under the loading presented in Table 3.4. As an illustrative example, Figure 3.5(a) shows the deformed shape of bearing B1NRU on its critical section, i.e., the plane of symmetry, together with a close-up view of its right side, highlighting the bulge patterns that develop. Figure 3.5(b-d) show the same close-up region but for bearings B1NRUθ3, B1NRUρ45, and B1NRUν35. As can be seen, the top-right corners of the unbonded bearings roll off the

loading surfaces when the bearing is sheared. The roll-off in unbonded bearings significantly reduces the tensile stresses in the rolled-off regions and the bond stress demands at the steel laminate–elastomer interfaces (Konstantinidis et al. 2008). Comparing the cases with and without imperfections reveals excessive bulging in the bottom interior elastomeric layer of the bearings with imperfections. This occurs because the bulging of elastomeric layers is proportional to their thickness, and the introduced imperfections result in increased thickness of the bottom interior layer. Figure 3.5(c) also reveals that the bent middle steel laminate in bearing B1NRUρ45 causes bulging that varies along the Z-direction, which was also noted in the experimental study by Belivanis (2017).

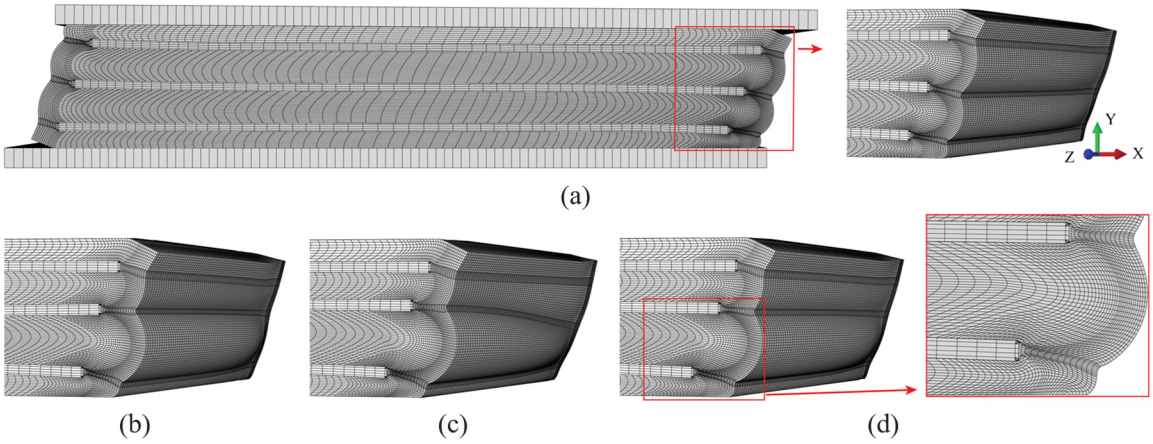

Figure 3.5 Formed bulge patterns on the right sides of bearings (a) B1NRU, (b) B1NRUθ3, (c) B1NRUρ45, and (d) B1NRUv35 when they are subjected to the corresponding service-level demands in Table 3.4

Figure 3.5(d) shows a magnified view of the deformation pattern in the bottom interior rubber layer of bearing B1NRUv35. The bulging pattern through the elastomer thickness close to the laminate edges differs from the parabolic bulging assumption due to compressive load postulated by theoretical approaches (Gent and Lindley 1959a; Gent and Meinecke 1970; Kelly 1993), especially under relatively large axial loads and rotations. This non-parabolic displacement pattern (which became more apparent in the third loading stage) can be related to different factors, including the strain hardening of rubber under relatively large shear strains (discussed later), effects of combined loading, and laminate flexing.

FEA results show that steel laminates close to their ends flex by different amounts, depending on their thickness, the thickness difference between two adjacent rubber layers, and the extent of roll-off. In this regard, the bulging of each rubber layer causes flexing of its adjacent laminates, while the shearing of the unbonded bearing causes additional flexing of all laminates conforming to the roll-off. The steel laminates of bearing B2NRUv35 flex more compared to other examined bearings; Figure 3.6(a),(b) highlights the flexing directions before and after the shear displacement is applied. The bulging of two rubber layers above/below a laminate has opposing effects on laminate flexing, and thus the flexural deformation becomes larger when the thickness of one rubber layer is more than the other, as shown in Figure 3.6(a). It is also observed in Figure 3.6(b) that the roll-off causes a different form of flexing (warping) in all steel laminates.

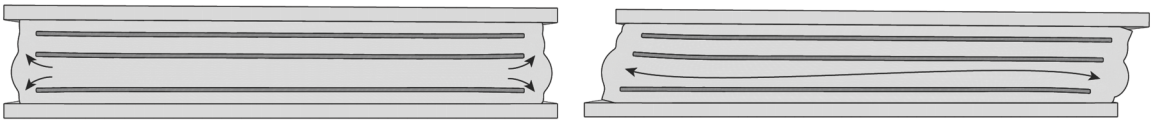

Figure 3.6 Flexing directions close to laminate edges of B2NRUv35 under compression and (a) before and (b) after shearing

3.5 Induced Shear Strains in the Elastomer

The shear strain specified in bridge specifications (e.g., AASHTO (2017), CSA (2019)) for designing elastomeric bridge bearings is twice the shear component of the Green-Lagrange strain tensor. Therefore, in this study, the XY component of the Green-Lagrange strain tensor (which is recorded in FEAs using a developed UVARM subroutine in Abaqus), multiplied by two, was used to assess the shear stain, γ_{XY}, in the elastomer. Figure 3.7(a),(b) shows the contour plots of γ_{XY} at the end of the analyses (i.e., for static+1.0×cyclic load) on the planes of symmetry of bearings B1NRU and B1NRB. As can be seen in the contour plots, the absolute value of γ_{XY} increases from near the center toward the ends of the steel laminates. According to theoretical approaches, the induced interfacial shear strains in a rubber layer due to combined actions of axial load, rotation, and shear displacement reach their maxima at the edge of the steel laminate adjacent to that layer (Gent and Meinecke

1970; Stanton and Roeder 1982; Kelly 1993; Van Engelen et al. 2017). However, theoretical approaches do not consider the rubber cover. The FEA results in this study show that the γ_{XY} along each steel–elastomer interface reaches its maximum at approximately 2.8 mm from the right edge of the steel laminate rather than at exactly the end. This phenomenon, also noticed by others (Stanton et al. 2008; Belivanis et al. 2015), is attributed to highly localized stress concentrations and mesh distortions at the edge of the laminates. Stanton et al. (2008) deemed FEA interfacial shear strain values within 6.35 mm (0.25 in.) from the laminate ends to be unreliable in their analyses.

The contour plots of Figure 3.7(a),(b) show that the small regions of the side cover adjacent to the laminate ends also experience very large values of γ_{XY}. Under lower-level loading (not shown), the maximum value of γ_{XY} at a horizontal steel–elastomer interface is higher than in the adjacent side covers. However, as the applied loading increases, particularly at the end of the third loading stage (shown), the maximum value of γ_{XY} in the side cover grows larger than at the interfaces. For instance, the maximum at the steel–elastomer interfaces of bearing B1NRU is 2.92, while the corresponding value in the side cover is 4.67. However, it is noted that maximum shear strain value at the steel–elastomer interfaces is more important because it is indicative of potential shear delamination, which is the most common failure mode in laminated bearings.

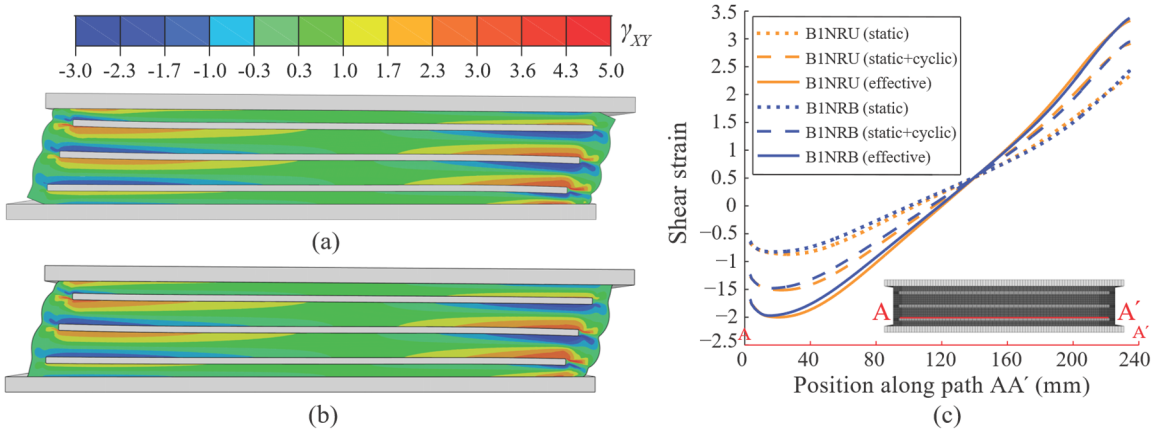

Figure 3.7 γ_{XY} contours under combined static+cyclic loading on the plane of symmetry of bearings (a) B1NRU and (b) B1NRB. (c) γ_{XY} profiles along the line path AA′ in bearings B1NRU and B1NRB under static, combined static+cyclic, and combined effective loading

Figure 3.7(c) shows the profiles of γ_{XY} under static, combined static+1.0×cyclic, and combined effective (i.e., static + 1.75×cyclic) loading, along the considered line path AA′ on the plane of symmetry of bearings B1NRU and B1NRB. The line path AA′ is located at the interface of the bottom interior rubber layer with the bottom steel laminate along which γ_{XY} attains its maximum value. The three γ_{XY} profiles of bearings B1NRB and B1NRU are very close to each other, indicating that the contact conditions at the top and bottom surfaces do not play a key role in the induced interfacial shear strains. Also, the maximum values of the curves corresponding to combined static+cyclic and combined effective loading along the examined line path are smaller compared to the expected values from Table 3.4, i.e., $\gamma_{st+cy} = 4$ and $\gamma_{eff} = 5$, suggesting that the superposition of shear strains computed using linear analytical solutions can give combined shear strains that are significantly different from the true shear strains induced in the rubber. For instance, the computed maximum values of γ_{XY} under combined effective loading in both bearings are 3.38 according to Figure 3.7(c). This difference between the FEA results of maximum interfacial shear strains and their expected values from analytical solutions are attributed to the following: (i) Analytical solutions specified in the bridge specifications (e.g., AASHTO (2017)) assume linear behavior of the elastomer; however, the instantaneous shear modulus at large shear strains is much higher than the initial shear modulus for both examined elastomers (see Figure 3.3). Under large loading, the elastomer near the steel–elastomer interfaces, and particularly close to the laminate ends, experiences large shear strains, while the elastomer close to the mid-height of the rubber layers experiences low shear strains. This, in turn, results in high instantaneous shear modulus near the interfaces and laminate edges, and thus further deformations are concentrated in less stiff portions of the layer, i.e., at the mid-height of the layers. The magnified view of the horizontal displacement pattern in the bottom interior rubber layer in Figure 3.5(d) confirms this observation. (ii) The linear superposition assumption of the shear strain components caused by different loading actions appears to not be very accurate. (iii) Analytical solutions do not account for the effects of the side cover. However, the FEA results in this study show that the portions of the side cover very close to the steel laminates are under hydrostatic

tension, and they are a source of resistance against the lateral bulging of the interior rubber layers. Such portions of the side cover are subjected to tensile stresses caused by the lateral bulging of the rubber layers at their top and bottom. Given the inextensibility of the steel laminates and incompressibility of the elastomer, these portions of the side covers limit the lateral bulging of rubber layers to some extent, and thus affect the shear strains values in the elastomer. Finally, as mentioned earlier, the effective shear strain capacity of 5 specified in bridge specifications (e.g., in design Method B in AASHTO (2017)) is based on experimental tests (Stanton et al. 2008) in conjunction with linear analytical solutions. Therefore, the smaller values of shear strains computed by FEA (compared to those predicted by the linear analytical solutions) does not necessarily mean that the bearings are safer than implied by bridge specifications (e.g., AASHTO (2017)).

Figure 3.8 shows the γ_{XY} contour plots for combined static+cyclic loading on section B, which passes through the plane of symmetry, of bearings B1NRU, B1NRUθ3, B1NRUρ45, and B1NRUν35. To facilitate comparison, the contour colors and the legend in Figure 3.8 are set such that γ_{XY} values higher than the maximum γ_{XY} and lower than the minimum γ_{XY} at all steel laminate-rubber interfaces are distinguished with dark red and dark blue, respectively. The maximum γ_{XY} values in bearings B1NRU, B1NEUθ3, B1NRUρ45, and B1NRUν35 are 2.92, 3.01, 3.10, and 3.12, respectively, suggesting that imperfections in unbonded bearings have a negligible effect on the maximum induced shear strains. Also, Figure 3.8 shows that the induced shear strains in the rubber close to the mid-height of the layers are larger when the bearing has imperfections. This observation agrees with the earlier point about the induced deformations in bearings concentrating more in less stiff portions of the elastomer in shear.

Figure 3.9 shows the γ_{st}, γ_{st+cy}, and γ_{eff} of the examined bearings. A comparison of the values of γ_{st} and γ_{st+cy} in Figure 3.9(a),(b) indicates that the cyclic loading does not cause a considerable increase in the maximum induced shear strain in the elastomer. It is also observed that bearings with ν = 3.5 mm may experience slightly higher shear strains compared to bearings with θ = 0.03 rad and ρ = 4.5 mm. More importantly, Figure 3.9(c)

shows that the differences between the γ_{eff} values of bearings with and without imperfections are negligible. Therefore, if these γ_{eff} values [computed by FEA using the 1.75 cyclic factor proposed by Stanton et al. (2008) based on experimental results and linear analytical solutions] are representative of the long-term effective shear strain demands, imperfections can be concluded to have negligible effects on the fatigue-induced failure of bearings.

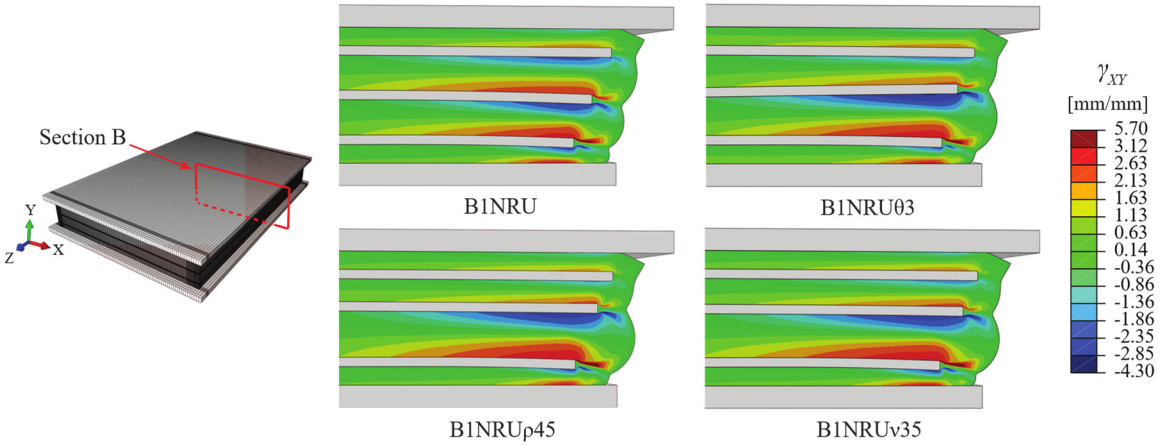

Figure 3.8 γ_{XY} contours on section B (the plane of symmetry) of four bearings under combined static+cyclic loading

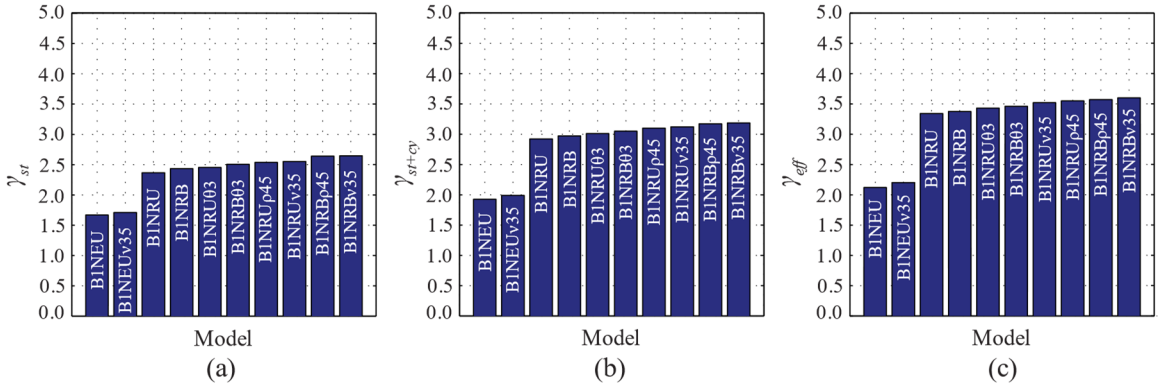

Figure 3.9 (a) γ_{st}, (b) γ_{st+cy}, and (c) γ_{eff} in the examined bearings

Bearings made of neoprene (i.e., B1NEU and B1NEUv35) experience much lower shear strains (see Figure 3.9). This difference is attributed to the higher hardening rate of the neoprene under shear, compared to the natural rubber, as illustrated in Figure 3.3(a).

Finally, Figure 3.9 shows that the bonded bearings experience slightly higher shear strains than the unbonded bearings.

3.6 Stresses at or Close to the Interfaces Between the Elastomer and Steel Laminates

The bond integrity at a horizontal steel–elastomer interface depends on the resultant tangential contact stress, σ_t, and the normal contact stress, σ_n, acting there. A compressive normal stress at these horizontal interfaces increases the steel–elastomer bond strength, while a tensile normal stress decreases it (Yura et al. 2001). For the examined bearings, the normal contact stresses at the interfaces of the interior elastomeric layers with steel laminates are always compressive. Thus, the normal contact stress is neglected in the assessment of the bond stress, and the bond stress is defined as the resultant tangential contact stress, or resultant shear stress carried at the interface nodes of the steel and elastomer (i.e., $\sigma_{bond} = \sigma_t$). σ_t is computed in Abaqus (Dassault Systemes 2019) as the resultant of two tangential shear stresses acting at each node (τ_{Cx} and τ_{Cz}) in the deformed configuration (i.e., $\sigma_t = \sqrt{\tau_{Cx}^2 + \tau_{Cz}^2}$).

Figure 3.10(a) shows the interface *I* between the bottom laminate and bottom rubber layer of bearing B1NRU, and Figure 3.10 (b),(c),(d) show the contour plots of τ_{Cx}, τ_{Cz}, and σ_t, respectively, at this interface, at the end of the third stage of the analysis. A 2.8-mm wide band along each laminate edge is disregarded to avoid unreliable results. The contour plots in Figure 3.10(b),(c) indicate that the maximum value of τ_{Cx} occurs near the right edge, whereas that of τ_{Cz} occurs near the top edge, which is expected based on linear analytical solutions (Kelly and Konstantinidis 2011). The τ_{Cx} are higher than the τ_{Cz} values because the largest bulging of rubber occurs in the X-direction (i.e., perpendicular to the long sides of the complete bearing). In fact, comparison of σ_t with τ_{Cx} and τ_{Cz} shows that the extreme values of σ_t close to each laminate edge are approximately equal to the component of tangential contact stress that dominates along that edge. Also, the contour plots indicate that the debonding of the rubber layers from the steel laminates starts from the right edge of laminates where σ_t is maximum.

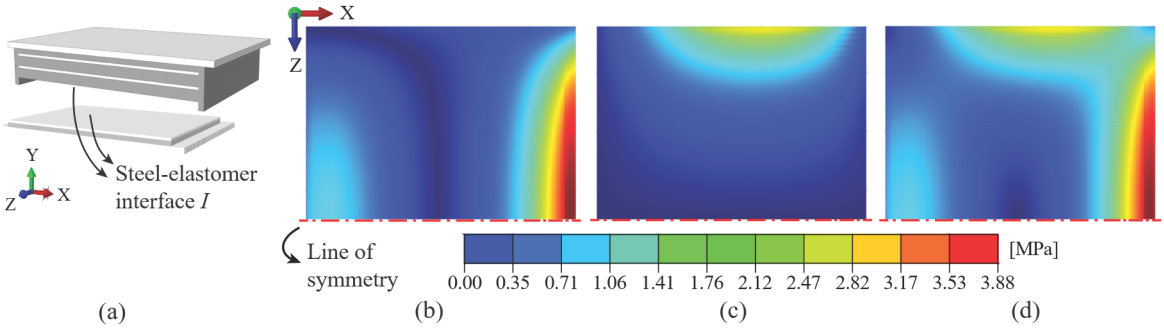

Figure 3.10 (a) Interface *I* between bottom laminate and bottom rubber layer and induced (b) τ_{Cx}, (c) τ_{Cz}, and (d) σ_t at this interface of the bearing B1NRU

Figure 3.11 shows the peak values of σ_t in different bearings. As can be seen, the laminate imperfections have a negligible effect on the peak values of σ_t. Also, bearings composed of NEO experience higher values of σ_t even though these bearings experience substantially lower interfacial shear strains compared to bearings with NR, as shown in Figure 3.9. This higher value of σ_t is due to the higher shear modulus of NEO and perhaps also due to its more aggressive hardening, and this highlights the need for a stronger bond in such bearings. Given the above observation, the shear strain demand used in the design of elastomeric bearings is by itself not sufficient to ensure a bearing's safety.

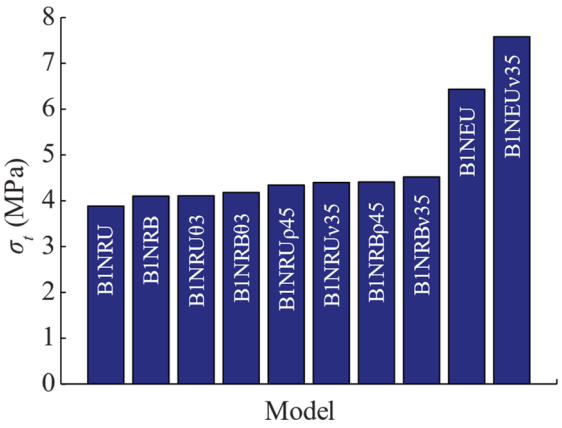

Figure 3.11 Peak values of σ_t in the bearings

The lateral bulging of the interior rubber layers pushes the cover rubber outwards. This deformation mechanism (see Figure 3.12) induces high tensile stresses (in a stress state close to a hydrostatic condition) in the vicinity of the vertical edges of the laminates. Stanton et al. (2008) concluded that the separation of the side cover from the vertical edge

of the laminates is initiated by either failure of the adhesive bond there or internal rupture of the rubber in close proximity of the interfaces. Stanton et al. (2008) also observed that such local failures spread at these interfaces as deformation increases, and they are distinguished on the bearing surface with the partial merging of two bulges into one larger bulge. Such local failures also finally lead to shear delamination.

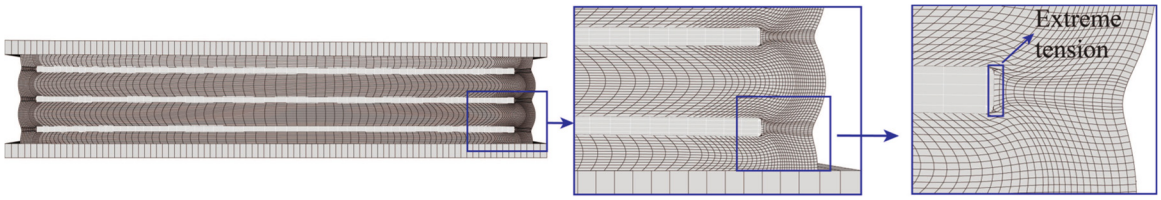

Figure 3.12 Deformation of the portion of the side cover close to the bottom interior steel laminate in bearing B1NRU under the static components of axial load and rotation

The numerical study of such local failures (the debonding and internal rupture) in elastomeric bearings involves three significant challenges. First, the steel–elastomer bond strength at vertical interfaces is difficult to measure or determine due to the complex state of stress there, and it cannot be assumed to be the steel–elastomer bond strength measured in standard tests, such as a peel test (ASTM 2014). Second, the initiation of internal rupture in the elastomer is dependent on several factors. Previous studies have estimated that the internal rupture of the elastomer may initiate at negative pressures of approximately 2.8G (Gent and Lindley 1959b) or 2.5G (Gent and Tompkins 1969; Dorfmann and Burtscher 2000). These negative pressure values correspond to incipient cavitation, i.e., expansion of existing microscopic voids to visible cavities, in incompressible rubber. However, this may not be always the case because the initial size of voids may be submicroscopic. Also, cavitation will occur at larger negative pressure values when the stress state is not completely hydrostatic or if shear stresses disturb the condition (Hang-Sheng and Abeyaratne 1992). Finally, severe distortion in rubber elements very close to those interfaces makes numerical investigation results in that region unreliable. Stanton et al. (2008) noted that the initial coalescence of the bulge patterns on the surface of bearings (caused by the spread of abovementioned local failures) occurred under monotonic loads producing maximum induced interfacial shear strain of approximately 6.7 based on

analytical solutions. However, the maximum induced shear strains in the examined bearings (based on analytical solutions and without involving the cyclic amplification factor) are expected to be much less than 6.7. For instance, for bearings B1NRU and B1NEU, these values are approximately 4 according to the formulas in AASHTO (2017), which are based on linear theory. Therefore, the examined bearings are not expected to experience such local failures in an influential extent under the monotonically applied loads and displacements in this study.

3.7 Damage in the Steel Laminates

Damage in the steel laminates of the bearings listed in Table 3.7 is assessed based on von Mises stress and plastic strain, which are considered effective measures for a ductile material like steel. This section initially discusses the distribution of the von Mises stress in the steel laminates. Then, a stress-based demand-to-capacity ratio (DCR) and strain-based ductility factor are used to assess the safety of the laminates against yielding or the extent of damage in them. For bearings without yielded steel laminates, the DCR, r_σ, is defined here as

$$r_\sigma = \frac{\sigma_{max}}{\sigma_{ys}} \tag{3.2}$$

where σ_{max} = maximum von Mises stress induced in the steel laminates, and σ_{ys} = yield stress of the steel (i.e., 248 MPa). For bearings with yielded steel laminates, a strain-based ductility, μ_ε, is used, which is defined as

$$\mu_\varepsilon = \frac{\varepsilon_{max}}{\varepsilon_{ys}} \tag{3.3}$$

where ε_{max} = maximum total (i.e., plastic plus yield strain) principal strain in the steel laminate, and ε_{ys} = yield strain of steel (i.e., 0.0012). The extent of yielding is also quantified using a plastic area ratio, $\bar{A}_p = A_p/A_s$, where A_p = yielded area of the laminate, and A_s = plan area of the laminate; and the plastic length ratio, $\bar{L}_p = L_p/L_s$, where L_p = yielded length of the laminate, and L_s = length of the laminate.

Figure 3.13(a),(b),(c) show contour plots of the von Mises stress on the top and bottom surfaces of the three steel laminates of bearings B3NRU, B1NRU, and B2NRU. As can be seen, the extreme values occur close to the edges of the steel laminates due to the flexural stresses that develop. It is noted that the steel laminates in bearings B1NRU and B2NRU experience yielding, while the maximum von Mises stress in the laminates of bearing B3NRU is 211 MPa. Yielding of the steel laminates in bearings B1NRU and B2NRU reveals that the minimum thickness values specified by the current bridge specifications (AASHTO 2017; CSA 2019) do not necessarily prevent the yielding of steel laminates in elastomeric bearings when designed according to the total shear strain design approach discussed earlier. Figure 3.13(d) shows contour plots of the maximum principal plastic strain, $\varepsilon_{pl,\,max}$, on the surfaces of the two steel laminates of bearing B2NRU that yield. The type of localized yielding observed in Figure 3.13(d) may not affect the short-term performance of bearings substantially and is generally not considered a failure; however, yielding is expected to spread in the long term due to repeated cycles from live loads. For example, Kalfas et al. (2020) observed that both the intensity and extent of damage in the steel laminates of seismic isolation elastomeric bearings increase when they are subjected to subsequent cycles of the same rotation and shear magnitudes. Assuming a single expansion/contraction cycle per day due to daily temperature changes, an elastomeric bearing experiences a total of 18,250 horizontal-displacement cycles in the 50-year service life of the bridge. The accumulated plasticity in the steel laminates may eventually lead to loss of axial load capacity of the bearing.

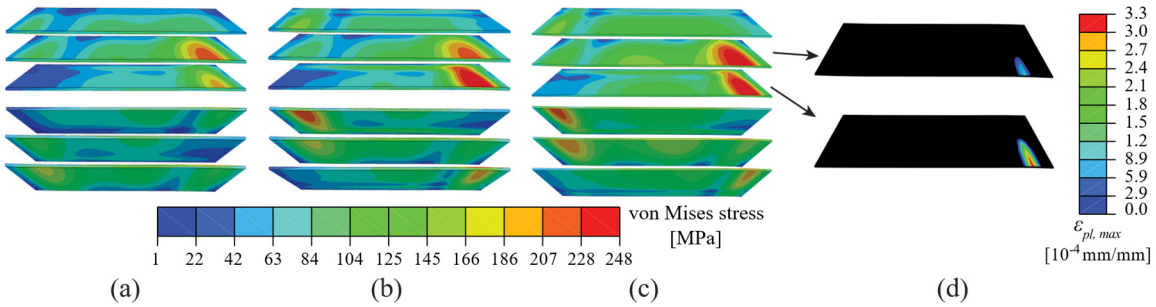

Figure 3.13 Von Mises stress contours in steel laminates of bearings (a) B3NRU, (b) B1NRU, and (c) B2NRU. (d) Plastic strain contours in steel laminates of bearing B2NRU

Figure 3.14 illustrates contour plots of the von Mises stress on the top surface of steel laminates and the yielded regions on the top surface of the bottom steel laminate in bearings B1NRUθ3, B1NRUρ45, B1NRUv35, and B1NEUv35. Bearing B1NEUv35 represents a bearing with an identical geometry to B1NRUv35 but made of neoprene instead of natural rubber. Several observations can be made by comparing the contour plots. When steel laminates yield, the yielding always occurs close to their edges, regardless of the imperfection configuration. The vertical misalignment of the laminates (e.g., in bearings B1NRUv35 and B1NEUv35) results in larger yielded regions in the critical steel laminate compared to the extent caused by the other imperfection configurations. Steel laminates in bearings made of the elastomer with higher shear modulus or more aggressive strain hardening (i.e., elastomer NE in bearing B1NEUv35) experience more widespread plasticity. The bottom steel laminate in bearing B1NEUv35 (Figure 3.14(d)) has yielded over a length equal to almost 81% of its whole length. Also, comparing the contour plots of Figure 3.13 and Figure 3.14 indicates that the elastomer type and steel laminate thickness play significant roles on the extent of damage in the steel laminates.

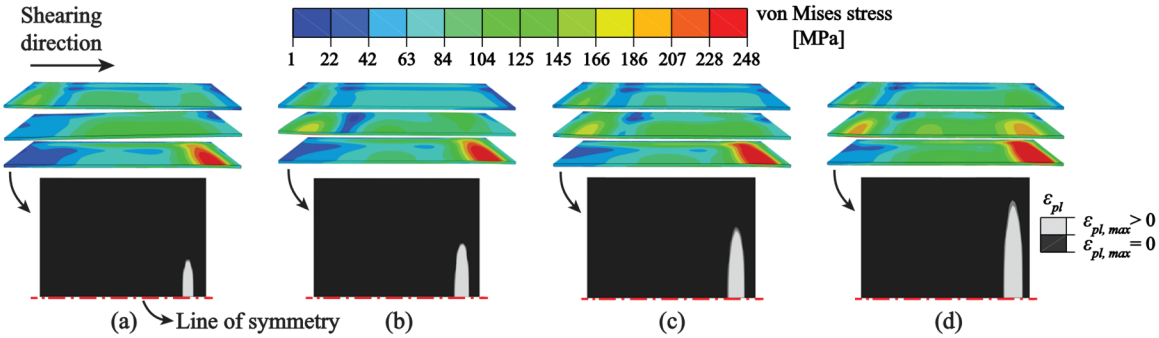

Figure 3.14 Contour plots of von Mises stress on the top surfaces of steel laminates and the yielded regions on the top surface of the bottom steel laminate in bearings (a) B1NRUθ3, (b) B1NRUρ45, (c) B1NRUv35, and (d) B1NEUv35

Figure 3.15 shows r_σ in bearings without yielded laminates and μ_ε in bearings with yielded laminates. Figure 3.15(a) shows that none of the laminates of bonded bearings (B1NRB, B1NRBθ3, B1NRBρ45, and B1NRBv35) yields, although their r_σ values are close to 1. For the unbonded bearings, B3NRU is the only one in which the laminates do not yield. Comparing the r_σ values in bearings with and without imperfections reveals that

imperfections could increase the peak von Mises stress by up to 14% in laminates when these do not yield. Also, comparing the range of μ_ε in Figure 3.15(b) with the ductility of mild steel at fracture reveals that the steel laminates in bearings subjected to service-level loads are very far from experiencing local fracture.

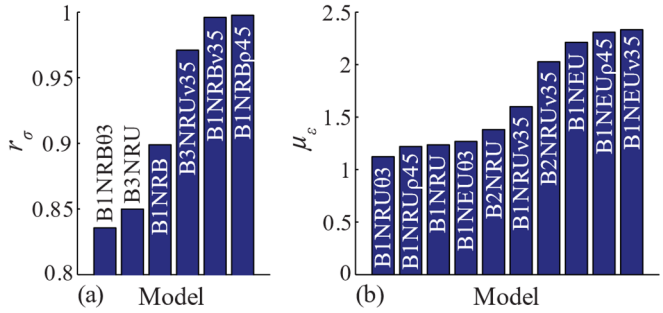

Figure 3.15 (a) Demand-to-capacity ratio, r_σ, in bearings without yielded steel laminates, and (b) ductility, μ_ε, in bearings with yielded steel laminates

The horizontal axes of Figure 3.16 show the percentage values of $\overline{A}_p$ and $\overline{L}_p$ for the three steel laminates of all bearings considered in this section; when a value is not plotted for a particular laminate of a bearing, that laminate does not experience any yielding. The vertical axis indicates the laminates, numbered from the bottom up. It is observed that larger portions of the bottom and middle laminates yield compared to the top laminates, which is attributed to the fact that the maximum bulging always happens in the bottom interior rubber layer of the bearings with the examined imperfections. It is also observed that the maximum $\overline{A}_p$ and $\overline{L}_p$ values are approximately 7% and 79%, respectively, both of which occur in the bottom 3-mm-thick laminate of bearing B1NEUv35. Given the ranges of $\overline{A}_p$ and $\overline{L}_p$ values in Figure 3.16, it is concluded that the yielding of the laminates spreads along the length of the bearings more than their widths. For the bearings without imperfections, the maximum $\overline{A}_p$ and $\overline{L}_p$ values are 6% and 72%, respectively, both of which occur in the bottom laminate of bearing B1NEU. Comparison of the extent of damage in the laminates of bearings with and without imperfections shows that the imperfections could increase the $\overline{A}_p$ value, $\overline{L}_p$ value, and the sum of A_p values of all laminates within a bearing by 109%, 53%, and 70%, respectively. These significant increases in $\overline{A}_p$ and $\overline{L}_p$

correspond to the defective bearings with 2-mm-thick laminates, indicating that the considered imperfections have a notably more damaging effect in thinner steel laminates. Also, although the plastic damage extent observed in the laminates is not expected to have a substantial influence on the short-term behavior of bearings, their long-term behavior is likely to be jeopardized due to the laminate imperfections.

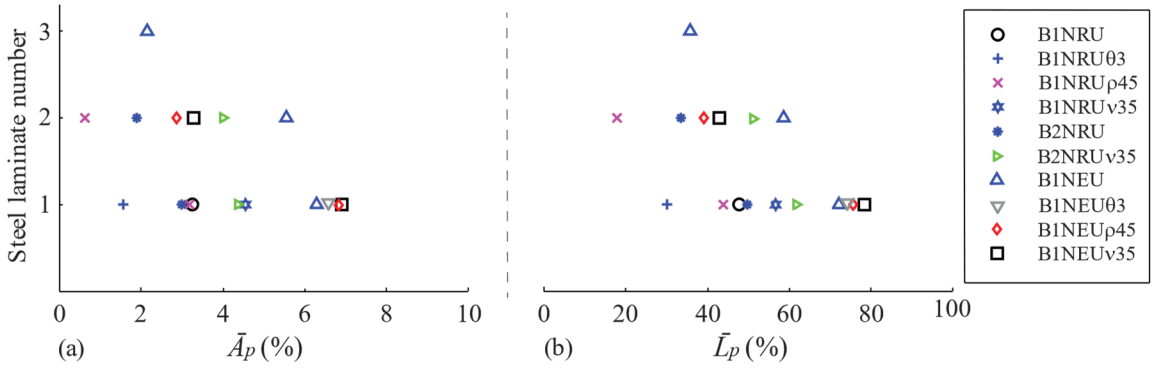

Figure 3.16 (a) $\bar{A}_p$ and (b) $\bar{L}_p$ in yielded steel laminates of different bearings

3.8 Vertical Stiffness and Deflection

Figure 3.17 shows the sensitivity of the vertical stiffness, K_v, and total vertical deflection [i.e., caused by total axial load], Δ, of the bearings listed in Table 3.8 for the examined imperfection configurations. The vertical axis of the top-row graphs shows the percentage change in K_v with respect to bearings without imperfections, i.e., $\delta K_v/K_{v0} = (K_v - K_{v0})/K_{v0}$, where K_{v0} = vertical stiffness of bearing without imperfections. Similarly, the bottom-row graphs show the percentage change in Δ, i.e., $\delta\Delta/\Delta_0 = (\Delta - \Delta_0)/\Delta_0$, where Δ_0 = total vertical deflection of bearing without imperfections. The vertical stiffness of each bearing is calculated as the slope of the straight line fitted to the vertical force–deflection curve of the bearing up to 4 MPa average pressure. As can be seen, the examined geometric imperfections always result in a decrease in K_v and in an increase in Δ, and K_v and Δ are respectively inversely proportional and directly proportional to the intensity of each imperfection. Comparing the percent changes of K_v and Δ in each bearing with imperfections indicates that both parameters are affected to a similar extent by the imperfections.

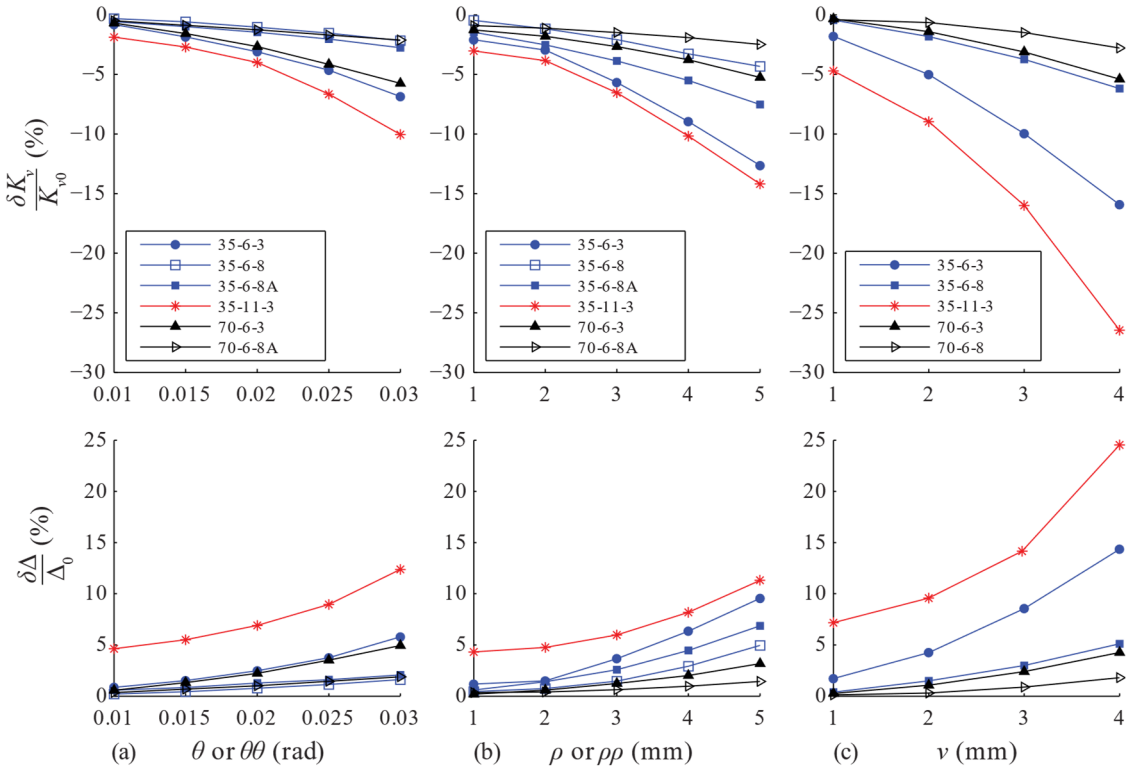

Figure 3.17 Sensitivity of K_v and Δ of bearings to (a) θ, (b) ρ, and (c) v

Figure 3.17 shows that the reduction in K_v and increase in Δ when all the laminates (except the top and bottom ones) are rotated or bent (e.g., bearing 35-6-8A) are not much different than when only a single laminate is rotated or bent (e.g., 35-6-8). For instance, the vertical stiffnesses of bearings 35-6-8A-ρ5 and 35-6-8-ρ5 are, respectively, 7% and 4% lower than that of the same bearing but without imperfections. Comparing the $\delta K_v/K_{v0}$ and $\delta\Delta/\Delta_0$ ranges for different bearings with imperfections shows that the K_v and Δ of bearings with higher shape factors and fewer rubber layers (e.g., 35-11-3) are affected more by the potential imperfection; the K_v and Δ of bearings 35-6-8 and 70-6-8 may change up to 6% by the imperfections, while K_v and Δ of bearing 35-11-3 may change up to 27%. Figure 3.17 also shows that K_v and Δ are affected more by v than θ and ρ. Finally, rotated laminates, bent laminates, and vertically misaligned laminates can decrease the K_v of bearings by up to 12%, 15%, and 27%, respectively. All in all, the examined laminate imperfections may cause changes to the K_v and Δ of bearings by up to 27% in the short-

term depending on the imperfection type and intensity, the shape factor of bearing, and the number of rubber layers.

Figure 3.18(a),(b) show the total deflection, Δ, and the live-load deflection caused by traffic, Δ_{LL}, of the bearings without an imperfection and the bearings with the imperfection kind that produces the largest increase of vertical deflection. Although, from Figure 3.17(c), the Δ of bearing 35-11-3-ν4 is 27% more than that of the same bearing without imperfections (i.e., 35-11-3), it is observed in Figure 3.18 that the Δ and Δ_{LL} of these bearings are very small (less than 2 mm). Therefore, although imperfections in bearings with higher shape factors and fewer laminates have more relative contribution to the total deflection of the bearings, the magnitude of the total deflection is very small. The Δ and Δ_{LL} of bearings influence the distribution of stresses in continuous bridges and may cause damage to joints and seals, respectively (Stanton and Roeder 1982). Therefore, the Δ and Δ_{LL} of thicker bearings (e.g., 70-6-8) can potentially cause damage to other bridge components. However, it is observed in Figure 3.18 that imperfections can play a minor role in the Δ and Δ_{LL} of bearings with relatively low shape factors and many laminates. AASHTO (2017) suggests that Δ_{LL} across a bridge joint be limited to 3.175 mm (0.125 inches) to avoid damage to expansion joints and also control the impact loading caused by the passage of vehicles across a stepped road surface at these joints (Roeder et al. 1989). In Figure 3.18(b), this limit has been denoted with a horizontal line. As can be seen, only bearings 70-6-8 and 70-6-8-ρ4 experience Δ_{LL} values exceeding the limit. However, imperfections have a very minor contribution to the Δ_{LL} of the bearing 70-6-8M4 compared to the contribution of parameters like the shape factor and the number of interior rubber layers. All in all, the short-term vertical deflection of bearings is not affected considerably by the examined imperfections. However, in the long term, imperfections may have considerable effects on the vertical deflections considering the spread of plasticity in the laminates.

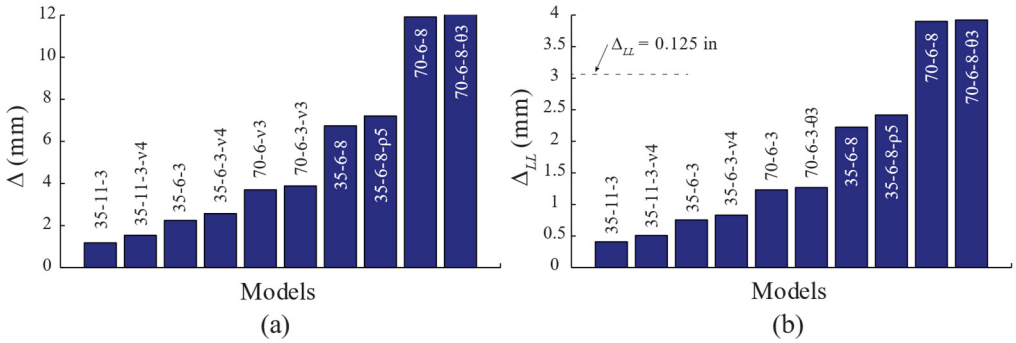

Figure 3.18 (a) Total deflection, Δ, and (b) live-load deflection, Δ_{LL}, of examined bearings

3.9 Conclusion

This paper investigated the potential effects of manufacturing imperfections on the service-level performance of the elastomeric bearings. The examined imperfections included vertically shifted, rotated, and bent steel laminates in bearings with different characteristics in terms of the elastomer type, contact description, shape factor, and number and thickness of steel laminates. The bearings were subjected to maximum loads and deformations permitted by bridge specifications (AASHTO 2017; CSA 2019). 3D finite element models of the bearings were modeled and analyzed in Abaqus. The study focused on shear strains of the elastomer, the contact stresses at steel–elastomer interfaces, the von Mises stresses and plastic strains of the steel laminates, and the vertical deflections of the bearings. The salient findings are summarized below:

- The peak interfacial shear strain demand on bearings subjected to maximum service loading gets limited mainly due to strain hardening of the elastomer near the laminate edges. The peak interfacial bond stress demands on bearings designed for a relatively high shear strain (e.g., 5) according to the bridge specifications (AASHTO 2017; CSA 2019) can be substantially different depending on the elastomer's shear modulus and strain hardening rate. Although imperfections increase the overall bulging of the critical rubber layers, they have negligible effects on the maximum interfacial shear strain and bond stress demands. In all cases, the maximum interfacial shear strain values in bearings with or without imperfections did not get close to the shear strain values expected based on the linear analytical solutions.

- The steel laminates flexed close to their edges, and in most of the examined unbonded bearings without imperfections, at least one laminate yielded. Thus, the minimum laminate thickness in bridge specifications (e.g., AASHTO (2017)) may not be sufficient to prevent yielding. However, the yielded laminates experienced very modest levels of ductility, far below the fracture limit. Also, 4-mm-thick laminates exhibited no yielding for the examined bearings. Therefore, the use of thicker steel laminates can prevent plastic damage in the laminates.
- Vertically misaligned laminates cause more plasticity in laminates compared to bent or rotated laminates. The imperfection configurations examined in this study could increase the peak von Mises stress by up to 14% in laminates when these do not yield, and by up to 70% the yielded area in the yielded laminates. Also, in the most critical case for the bearings considered, the 3-mm-thick laminates experienced plasticity in a region corresponding to almost 7% and 79% of the laminate area and length, respectively. Plastic damage can spread in the laminates in long-term and lead to a substantial reduction of the bearing's vertical stiffness.
- Imperfections almost always decrease the vertical stiffness of the elastomeric bearings. The considered rotational misalignment, bent shape, and vertical misalignment of laminates could decrease the short-term vertical stiffness of bearings by up to 12%, 15%, and 27%. The simultaneous rotation or bending of laminates did not cause a substantial decrease in stiffness compared to what is caused by a single-laminate imperfection. The upper limits mentioned above correspond to thin bearings with two interior rubber layers, the high shape factor of 11, and considerable imperfection intensities. The vertical deflection of bearings seems to be more problematic in thick bearings (i.e., thicker than 100 mm) in which the considered laminate imperfections contribute less than 5% in the total deflection in short-term.

Data Availability Statement

All data, models, and code generated or used during the study appear in the submitted article.

Acknowledgments

This research was supported by the Ministry of Transportation of Ontario (MTO) through the Highway Infrastructure Innovation Funding Program. The authors are grateful to Kris Mermigas (Head Engineer, Structures Office, MTO) and Ben Huh (Lead Engineer, Structures Office, MTO) for their committed support during this work. Any opinions, findings, or recommendations in this paper are those of the authors and do not necessarily reflect the views of the sponsor.

References

AASHTO. (American Association of State Highway and Transportation Officials). 2017. *AASHTO LRFD bridge design specifications*. Washington, DC: AASHTO.

AASHTO. (American Association of State Highway and Transportation Officials). 2018. *Standard specification for plain and laminated elastomeric bridge bearings*. Washington, DC.

Ahmadi Soleimani, S., D. Konstantinidis, and G. P. Balomenos. 2020. "Vision-Based Quality Control Testing of Elastomeric Bridge Bearings." In *Proc., Structures Congress,* 651-664. Reston, VA: ASCE.

Ahmadi Soleimani, S., D. Konstantinidis, and G. P. Balomenos. 2021. "Nondestructive assessment of elastomeric bridge bearings using 3D digital image correlation." *J. Struct. Eng.*, 148 (1), 04021233. https://doi.org/10.1061/(ASCE)ST.1943-541X.0003200.

ASTM. 2014. *Standard test methods for rubber property—Adhesion to Rigid Substrates*. D429-14. West Conshohocken, PA.

Balomenos, G. P., A. S. Genikomsou, M. A. Polak, and M. D. Pandey. 2015. "Efficient method for probabilistic finite element analysis with application to reinforced concrete slabs." *Eng. Struct.*, 103, 85-101. https://doi.org/10.1016/j.engstruct.2015.08.038.

Balomenos, G. P., and M. D. Pandey. 2017. "Probabilistic finite element investigation of prestressing loss in nuclear containment wall segments." *Nucl. Eng. Des.*, 311, 50-59. http://dx.doi.org/10.1016/j.nucengdes.2016.11.018.

Belivanis, K. V. 2017. "Expanding the use of elastomeric bearings for higher demand applications." Ph.D. thesis, Dept. of Civil, Architectural and Environmental Engineering, The Univ. of Texas at Austin.

Belivanis, K. V., L. Han, C. Sun, T. Helwig, M. Engelhardt, J. Tassoulas, and E. Williamson. 2015. *Extending use of steel-laminated elastomeric bearings to higher demand applications*. *Report 0-6785-1*, Center for Transportation Research, The Univ. of Texas at Austin.

Caltrans. 1994. *Bridge Memo to Designers*. Section 7: Bridge Bearings. California Department of Transportation, Sacramento, California.

CDOT. (Colorado Department Of Transportation). 2018. *CDOT Bridge Design Manual*. Appendix A: Design Examples. Denver, Colorado.

CSA. (Canadian Standards Association). 2019. *S6-19 Canadian highway bridge design code*. Section 11: Joints and Bearings. Toronto, Ontario.

Dassault Systemes. 2019. "ABAQUS 2019 Theory manual." *Dassault Systemes Simulia Corp., Providence, Rhode Island*.

Dorfmann, A., and S. L. Burtscher. 2000. "Aspects of cavitation damage in seismic bearings." *J. Struct. Eng.*, 126 (5), 573-579. https://doi.org/10.1061/(ASCE)0733-9445(2000)126:5(573).

ECS. (European Commission for Standardization). 2005. *Structural Bearings-Part 3: Elastomeric Bearings*. Brussels, Belgium.

El-Reedy, M. 2016. *Onshore structural design calculations: Power plant and energy processing facilities*. Butterworth-Heinemann.

Gent, A., and P. Lindley. 1959a. "The compression of bonded rubber blocks." *Proc. Inst. Mech. Eng.*, 173 (1), 111-122. https://doi.org/10.1243/PIME_PROC_1959_173_022_02.

Gent, A., and P. Lindley. 1959b. "Internal rupture of bonded rubber cylinders in tension." *Proc. Roy. Soc. Lond. A*, 249 (1257), 195-205. https://doi.org/10.1098/rspa.1959.0016.

Gent, A., and E. Meinecke. 1970. "Compression, bending, and shear of bonded rubber blocks." *Polym. Eng. Sci.*, 10 (1), 48-53. https://doi.org/10.1002/pen.760100110.

Gent, A., and D. Tompkins. 1969. "Nucleation and growth of gas bubbles in elastomers." *J. Appl. Phys.*, 40 (6), 2520-2525. https://doi.org/10.1063/1.1658026.

Han, L. 2016. "Elastomeric bearings in high demand applications: Numerical study and experimental Validation." Ph.D. thesis, Dept. of Civil, Architectural and Environmental Engineering, The Univ. of Texas at Austin.

Hang-Sheng, H., and R. Abeyaratne. 1992. "Cavitation in elastic and elastic-plastic solids." *J. Mech. Phys. Solids.*, 40 (3), 571-592. https://doi.org/10.1016/0022-5096(92)80004-A.

Huang, W., X. Xu, K. Wang, and W. Liu. 2018. "Numerical Simulation of Steel-Laminated Bearing Considering Friction Slipping." *International Journal of Engineering and Technology*, 10 (2). https://doi.org/10.7763/IJET.2018.V10.1052.

Kalfas, K. N., S. A. Mitoulis, and D. Konstantinidis. 2020. "Influence of Steel Reinforcement on the Performance of Elastomeric Bearings." *J. Struct. Eng.*, 146 (10), 04020195. https://doi.org/10.1061/(ASCE)ST.1943-541X.0002710.

Kelly, J. 1993. *Earthquake Resistant Design with Rubber*. Springer-Verlag, London, UK.

Kelly, J. M., and D. Konstantinidis. 2011. *Mechanics of rubber bearings for seismic and vibration isolation*. Chichester, UK: John Wiley & Sons.

Khaloo, A., A. Maghsoudi-Barmi, and M. E. Moeini. 2020. "Numerical parametric investigation of hysteretic behavior of steel-reinforced elastomeric bearings under large shear deformation." *Structures*, 26, 456-470. https://doi.org/10.1016/j.istruc.2020.04.029.

Konstantinidis, D., J. M. Kelly, and N. Makris. 2008. *Experimental investigation on the seismic response of bridge bearings*. *Report EERC-2008/02*, Earthquake Engineering Research Center, University of California, Berkeley.

Kumar, A. 2001. "Performance related parameters of elastomeric bearings." Ph.D. Dissertation, Dept. of Civil, Architectural and Environmental Engineering, The Univ. of Texas at Austin.

Moghadam, S. R., and D. Konstantinidis. 2017a. "Finite element study of the effect of support rotation on the horizontal behavior of elastomeric bearings." *Compos. Struct.*, 163, 474-490. http://dx.doi.org/10.1016/j.compstruct.2016.12.013.

Muscarella, J. V., and J. Yura. 1995. "An experimental study of elastomeric bridge bearings with design recommendations." Ph.D. thesis, Center for Transportation Research, The University of Texas at Austin.

NYSDOT. (New York State Department of Transportation). 2010. *NYSDOT Bridge Manual*. Section 12: Bridge Bearings. Albany, New York.

Roeder, C. W., J. F. Stanton, and T. Feller. 1989. *Low temperature behavior and acceptance criteria for elastomeric bridge bearings*. Washington, DC: Transportation Research Board.

Sokoli, D., W. Shekarchi, E. Buenrostro, and W. M. Ghannoum. 2014. "Advancing behavioral understanding and damage evaluation of concrete members using high-resolution digital image correlation data." *Earthquakes Struct.*, 7 (5), 609-626. http://dx.doi.org/10.12989/eas.2014.7.5.609.

Stanton, J. F., and C. W. Roeder. 1982. *Elastomeric Bearings Design, Construction, and Materials*. *Report 248*, National Cooperative Highway Research Program (NCHRP), Washington, DC: N. R. C. Transportation Research Board.

Stanton, J. F., C. W. Roeder, P. Mackenzie-Helnwein, C. White, C. Kuester, and B. Craig. 2008. *Rotation limits for elastomeric bearings*. *Report 596*, National Cooperative Highway Research Program (NCHRP), Washington, DC: Transportation Research Board.

Sun, C. 2015. "Material study of the steel reinforced elastomeric bridge bearings." Ph.D. thesis, Dept. of Civil, Architectural and Environmental Engineering, The Univ. of Texas at Austin.

Van Engelen, N. C., D. Konstantinidis, and M. J. Tait. 2017. "Shear strain demands in elastomeric bearings subjected to rotation." *J. Eng. Mech.*, 143 (4), 0733-9399. https://doi.org/10.1061/(ASCE)EM.1943-7889.0001194.

Van Engelen, N. C., P. M. Osgooei, M. J. Tait, and D. Konstantinidis. 2015. "Partially bonded fiber-reinforced elastomeric isolators (PB-FREIs)." *Structural Control and Health Monitoring*, 22 (3), 417-432. https://doi.org/10.1002/stc.1682.

Yakut, A., and J. A. Yura. 2002. "Parameters influencing performance of elastomeric bearings at low temperatures." *J. Struct. Eng.*, 128 (8), 986-994. https://doi.org/10.1061/(ASCE)0733-9445(2002)128:8(986).

Yura, J., A. Kumar, A. Yakut, C. Topkaya, E. Becker, and J. Collingwood. 2001. *Elastomeric bridge bearings: Recommended test methods*. *Report NCHRP 449*,

National Cooperative Highway Research Program (NCHRP), Washington, DC: Transportation Research Board.

4 Effects of Steel Laminate Characteristics and Imperfections on the Behavior of Unbonded Elastomeric Bridge Bearings Subjected to Large Lateral Displacements

Soleimani S.A., Konstantinidis D., and Balomenos G.P. (2022). Effects of Steel Laminate Characteristics and Imperfections on the Performance of Unbonded Elastomeric Bridge Bearings Subjected to Large Lateral Displacement. To be submitted for publication in a peer-reviewed journal.

Abstract

Unbonded laminated elastomeric bridge bearings are designed to accommodate service-level deformations, but during an earthquake they can experience deformation demands that are significantly larger than those for which they were designed. Because these bearings are critical elements of a bridge, they must perform reliably even under seismic-level demands. The effects of the characteristics and condition of the steel laminates on the behavior of these bearings have received limited attention in the literature. Yet, the manufacturing process of these bearings sometimes introduces imperfections. For instance, during vulcanization, the steel laminates might get rotated or bent. In this context, this paper investigates the effects of manufacturing imperfections and thickness properties of the steel laminates on the behavior of unbonded bearings subjected to simultaneous axial loading and five cycles of lateral displacements with increased amplitudes up to 200% equivalent shear strain. The deformation pattern and hysteretic response characteristics of the bearings and the potential damage (in terms of plastic deformations) in their steel laminates are studied using finite element analysis. It is observed that imperfections can increase the roll-off of a bearing and increase its risk of instability. Imperfections can also increase the bearing's effective lateral stiffness and a specific plastic-energy-based damage factor up to 18% and 564%, respectively. Plastic damage in the laminates is found to be appreciably dependent on their thickness. Under cyclic displacement, damage manifests itself more in the form of spreading of the yielded area rather than increased peak strain

ductility. Plastic strains in the steel laminates do not get close to the fracture limit, and all the bearings exhibit fairly stable hysteretic loops under the five-cycle loading protocol.

Keywords: Laminated Elastomeric Bridge Bearings; Steel laminates; Manufacturing Imperfections; Lateral Stiffness; Damping Ratio; Plasticity Ratio; Damage Factor

4.1 Introduction

Elastomeric bridge bearings are composed of alternating thin rubber layers and steel laminates (hereinafter referred to as *laminates*) have been historically used in bridges as reliable and cost-efficient devices for accommodating service-level displacements and rotations caused mainly by thermal, gravity, and traffic loads. These bearings can be classified as *fully unbonded*, *single-side unbonded*, and *fully bonded*, based on their connections to contact surfaces. The fully bonded bearings feature vulcanized end plates at top and bottom, which are bolted to the bridge supports. In contrast, both sides of fully unbonded bearings and one side of the single-side unbonded bearings are in direct frictional contact with support surfaces (Xiang et al. 2021). In single-side unbonded and fully unbonded bearings, hereinafter both referred to as *unbonded bearings*, the transferred lateral forces are limited by the frictional resistance of the contact surfaces.

Under service-level conditions, the lateral displacement of unbonded elastomeric bridge bearings is usually restricted to 0.5-0.7 equivalent shear strain (ESS) [i.e., imposed lateral displacement divided by total rubber thickness] (AASHTO 2017; CSA 2019). However, under strong seismic conditions, retainers of bearings and shear keys might fail, and then bearings might experience large shearing deformation and sliding (Filipov et al. 2013b; Xiang et al. 2021). This could lead to permanent offset or unseating of fully unbonded bearings, as observed during the 1999 Chi-Chi, 2008 Wenchuan, and 2010 Chile earthquakes (Liu et al. 2006; Li et al. 2008; Han et al. 2009; Kawashima et al. 2011) . Several experimental studies (Mori et al. 1999; Konstantinidis et al. 2008; Li et al. 2017; Wu et al. 2018; Khaloo et al. 2020) have investigated the behavior of unbonded bearings subjected to beyond service-level horizontal displacements. As the imposed horizontal displacement on these bearings increases, the unbonded surfaces of the bearings roll off

the support surfaces (Mori et al. 1999). This roll-off is then followed by either rollover (i.e., the deformation state in which the initially vertical sides of the bearings become in full contact with the horizontal surfaces) and then sliding or by sliding without rollover, depending on the thickness of the bearings and laminates and the friction resistances at the bearing-support interfaces (Konstantinidis et al. 2008; Wu et al. 2018). These bearings provide stable hysteretic shear-sliding behavior and undergo large slip travel with minor abrasions under light to moderate axial loads followed by cyclic horizontal displacement equivalent to 3 to 4 ESS (Steelman et al. 2012; Li et al. 2017; Xiang and Li 2017; Wu et al. 2018). In contrast, for bearings with 2-mm thin laminates under relatively high compressive loads (8.3 MPa), Konstantinidis et al. (2008) observed appreciable abrasion as a result of post-rollover sliding that occurred in tests at 3.0 ESS. Li et al. (2017) observed that the energy dissipation capacities of bearings under displacements equivalent to 3 to 4 ESS can even become close to that of a typical seismic isolator (e.g., lead rubber bearings).

Because of their low lateral stiffness and relatively high energy dissipation, some studies have proposed the use of unbonded bearings as *seismic fusing* or *quasi-isolation* devices in areas of moderate seismicity (Filipov et al. 2013a; Filipov et al. 2013b; Luo et al. 2017). In this role, unbonded bearings are permitted to undergo large lateral displacements and to slide at their interfaces with substructures or superstructures, resulting in the period elongation and energy dissipation through friction sliding mechanisms (Filipov et al. 2013b). Several experimental and numerical studies have been conducted in this context in order to assess the seismic performance of bridges equipped with unbonded bearings (Filipov et al. 2013b; Wu et al. 2018; Xiang et al. 2018). These studies demonstrated the improved seismic performance and reduced damage of the bridges equipped with unbonded bearings. However, restraining systems such as shear keys, angle side retainers, and steel dampers and adequate support lengths or seat widths were recommended or found necessary for controlling the peak and residual bearing displacements and avoiding the unseating of the bearings and span loss especially in the transverse direction of bridges and at the hazard level associated with the maximum considered earthquakes.

Research on the effect of laminate thickness on the response and potential damage of elastomeric bearings under large lateral displacement has been scarce. Previous studies (Zhang and Li 2019; Kalfas et al. 2020) have shown that laminate thickness has a minimal effect on the hysteretic response characteristic, including the effective horizontal stiffness and damping ratio, of fully bonded bearings but has a substantial effect on the stress distribution and potential plastic deformations in the laminates. Compared to fully bonded bearings, the lateral behavior of unbonded bearings might be more dependent on the thickness of the laminates, which can promote or suppress roll-off and thus affect the effective shear area. In addition, the manufacturing process of elastomeric bearings involves rubber vulcanization, during which the unavoidable flow of rubber under high pressure and temperature can cause the laminates to rotate and bend (Yura et al. 2001; Ahmadi Soleimani et al. 2020; Ahmadi Soleimani et al. 2021). Under service-level load and displacement demands, such manufacturing imperfections have been found to have small effects on the stresses and strains in the rubber of bearings and moderate effects on the bearings stiffnesses in different directions. However, such imperfections can considerably increase the tensile stresses in laminates and cause plastic damage (Kumar 2001; Belivanis 2017). To the best of the authors' knowledge, no studies have investigated the effects of these types of manufacturing imperfections and of the thickness of laminates on the behavior of unbonded bearings subjected to large lateral displacements.

This paper presents a numerical study on the effects of manufacturing imperfections in the form of rotationally misaligned and bent laminates on the behavior of fully unbonded bearings subjected to large cyclic displacements demands. Of primary focus is how laminate thickness affects the behavior of unbonded bearings with and without imperfections. Three-dimensional finite element analyses (FEA) are conducted on models of bearings with various characteristics in terms of plan dimensions, slenderness, shape factor, laminate thicknesses, and imperfection type and intensity. The analysis considers the combined effects of axial load and cyclic horizontal displacement with increased amplitudes from 0.5 to 2.0 ESS. Initially, the deformation patterns of bearings are studied. Then, the effective horizontal stiffness and equivalent damping ratio of bearings are studied

at different ESS values. Finally, damage in laminates is assessed based on induced von Mises stresses and plastic strain.

4.2 Examined Bearings and Assessment Approach

This section provides details on the characteristics of the examined fully unbonded laminated elastomeric bridge bearings in terms of their material properties, geometry, and displacement and loading demands.

4.2.1 Steel and Rubber Material Properties

The rubber of the examined bearings is assumed to be the scragged neoprene with mechanical properties adopted from the study by Sun (2015), which included tests under cyclic simple shear loading up to a shear strain of 2.0. Figure 4.1(a) shows one full cycle of the stabilized hysteretic loop of the preconditioned neoprene under simple shear loading and unloading. The laminate is considered to be Grade A36 with data for the uniaxial stress–strain curve adopted from El-Reedy (2016) (see Figure 4.1(b)). Table 4.1 shows material properties of the steel and the neoprene considered in this study.

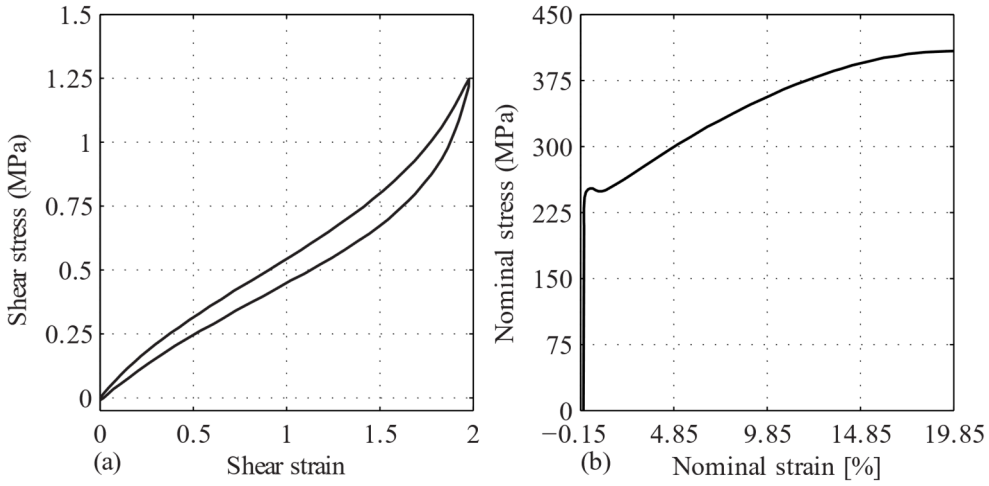

Figure 4.1 (a) Simple shear test data of the neoprene (adopted from Sun (2015)) and (b) Steel grade A36 stress–strain data (El-Reedy (2016))

Table 4.1 Material properties of the neoprene (Sun 2015) and steel (El-Reedy 2016)

Material	Property	Symbol	Value
Neoprene	Shear modulus	G_{NEO}	0.65 MPa
	Poisson's ratio	ν_{NEO}	0.4998
Steel	Young's modulus	E_s	200 GPa
	Yield stress	σ_{vs}	248 MPa
	Poisson's ratio	ν_s	0.3

4.2.2 Geometry of Bearings without Imperfections

The examined bearings without imperfections have three different geometries in terms of plan dimensions and total rubber thickness, as listed in Table 4.2. They were chosen based on bearing designs used in the Province of Ontario, Canada, and feature representative characteristics of typical bearings in practice. The number of laminates in bridge bearings used in Ontario range from three to eight, and the shape factor (defined for a rubber layer as the ratio of plan area to total lateral area free to bulge) usually from 6 to 12. B1, B2, and B3 are referred to as bearing groups because three different laminate thickness values are considered for each (2, 3, and 4 mm). Note that the minimum laminate thickness permitted by AASHTO (2017), ECS (2005), and CSA (2019) is 1.6, 2, and 3 mm, respectively. Bearing group B1 involves small, low-shape-factor bearings with a high width-to-rubber-height ratio. Bearing group B2 involves small, low-shape-factor bearings with almost the minimum width-to-rubber-height ratio permitted in Ontario, respectively. Bearing group B3 involves large, high-shape-factor bearings. All bearing groups B1, B2, and B3 serve as benchmarks to investigate the effects of imperfections on their performance under relatively large lateral displacement demands.

Table 4.2 Geometric properties of the bearings without imperfections (unit: mm)

Bearing Groups	Plan dimensions	Total Rubber thickness	Rubber layer thickness	Laminate thickness	Number of laminates	Cover rubber layer thickness	Side cover thickness	Shape factor
B1	400×300	36	13	2, 3, and 4	3	5	6	6.6
B2	400×300	101	13	2, 3, and 4	8	5	6	6.6
B3	700×500	99	12.75	2, 3, and 4	8	5	6	11.2

4.2.3 Geometry of Bearings with Imperfections

Preliminary FEA showed that the effects of vertically misaligned and horizontally misaligned laminates on the lateral response of bearings are negligible. Therefore, the present study focuses on two other imperfection forms including rotationally misaligned laminates and bent laminates (see Figure 3.1 (b),(c)). Also, considering the imperfections observed in destructive test reports provided by the Ministry of Transportation of Ontario (MTO) (read Section 3.2.2), this study models the top and bottom laminates without imperfections and the internal laminates having equal amount of rotation or bending.

The rotational misalignment of internal laminates is denoted by θ, as shown in Figure 4.2(a),(c) for bearings with three and eight laminates, respectively. Based on the examined destructive test reports and the observations of Belivanis (2017), the shape of bent laminates can be approximated well by a half-sine curve with amplitude ρ, as shown in Figure 4.2(b),(d). Note that the shear load or displacement is applied along the short sides of the bearings, i.e., parallel to the X-axis in Figure 4.2. The maximum values of θ and ρ observed in the examined destructive test reports were approximately 0.03 rad and 4.5 mm, respectively, for a single laminate within the three-laminate bearings, while the maximum of the average values of θ and ρ of the internal laminates within the eight-laminate bearings were approximately 0.025 rad and 3.5 mm, respectively [*average* because of slight differences among the values of the internal laminates]. This study uses these values for the finite element modelling of the three-laminate and eight-laminate bearings with imperfections. Also, the labels θ and ρ are used later as part of the nomenclature used to distinguish finite element (FE) models with imperfections.

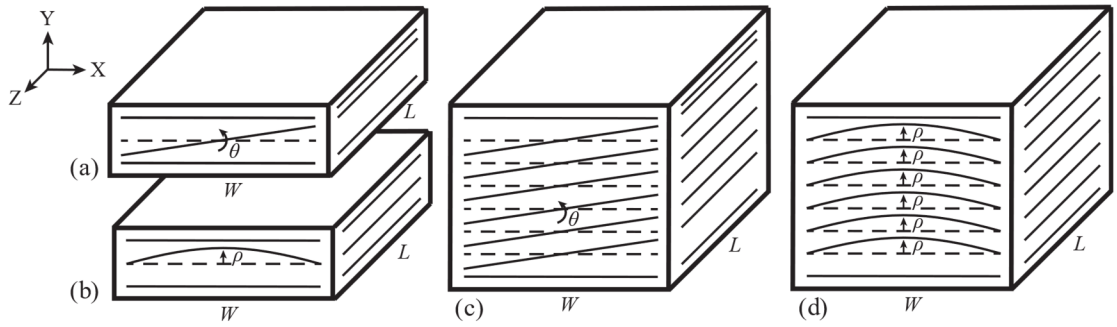

Figure 4.2 Imperfection configurations; (a, c) rotationally misaligned internal laminates and (b, d) bent internal laminates

4.2.4 Examined Bearings

Twenty-seven bearings with and without imperfections are examined in this study (see Table 4.3) considering different bearing geometries (i.e., B1, B2, and B3) and different laminate thicknesses (i.e., 2, 3, and 4 mm). The bearing labels in Table 4.3 comprise either two or three groups of alphanumeric characters according to the naming convention explained in Figure 4.3.

Table 4.3 Bearings considered for assessing the effects of imperfections on their lateral behavior

Bearing Group	Imperfection	Bearings with 2-mm-thick laminates	3-mm-thick laminates	4-mm-thick laminates
B1	——	B1TS2	B1TS3	B1TS4
	θ = 0.03 rad	B1TS2θ3	B1TS3θ3	B1TS4θ3
	ρ = 4.5 mm	B1TS2ρ45	B1TS3ρ45	B1TS4ρ45
B2	——	B2TS2	B2TS3	B2TS4
	θ = 0.025 rad	B2TS2θ25	B2TS3θ25	B2TS4θ25
	ρ = 3.5 mm	B2TS2ρ35	B2TS3ρ35	B2TS4ρ35
B3	——	B3TS2	B3TS3	B3TS4
	θ = 0.025 rad	B3TS2θ25	B3TS3θ25	B3TS4θ25
	ρ = 3.5 mm	B3TS2ρ35	B3TS3ρ35	B3TS4ρ35

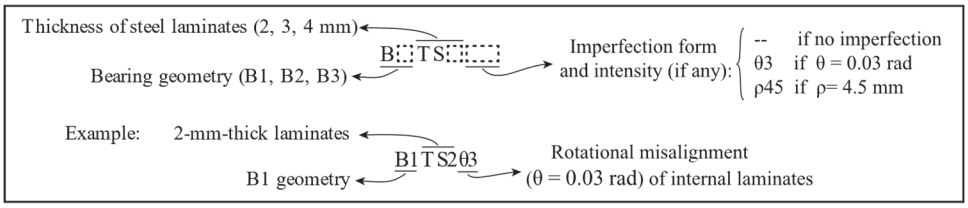

Figure 4.3 Naming convention for bearing FE models

4.2.5 Displacement and Loading Demands

The behavior of the bearings is studied under combined axial load and cyclic lateral displacement. Lateral displacements are imposed on the bearings along their shorter sides (i.e., *W* in Figure 4.2) or parallel to the bridge's longitudinal axis, i.e., the X-axis in Figure 4.2, because according to preliminary analyses, the examined imperfections cause the maximum variations in the bearings' lateral responses under such a displacement scenario. Bridge specifications (IDOT 2012; OPSS 2017; NYSDOT 2019) specify different lower and upper limits for the average pressure on the bearings due to gravity loads, all falling within the 1 to 7 MPa range. Also, ECS (2005), AASHTO's (2017) design Method B, and CSA (2019) permit higher pressure values based on a total shear strain design approach. In general, the lower and upper bound limits of pressure are mainly intended for preventing bearing "walk-out" from the supporting area, and shear delamination, respectively. Based on technical data provided by the MTO (personal correspondence) for bearings used in Ontario bridges, an average pressure of 5.5 MPa due to gravity loads is a reasonable value and is therefore used in the numerical analysis of this study. In addition, the bearings are subjected to a protocol of five lateral displacement cycles of increasing amplitude, from 0.5 to 2.0 ESS (see Figure 4.4). The multiple cycles of lateral displacements are imposed to assess the hysteretic characteristics of the bearings for different ESS values, and to assess the potential spread of damage in their laminates. It is noted that imposing displacements beyond 2.0 ESS caused some preliminary FEAs to abort due to excessive rubber element distortions at the leading edges of the bearing. Also, considering previous experimental studies (e.g., Konstantinidis et al. (2008), Steelman et al. (2012), Xiang and Li (2017), and Wu et al. (2018)), bearings begin to experience full sliding at an ESS value ranging from 1.0 to 2.6 depending on the roughness of contacting surfaces, average pressure, loading rate, and temperature. Therefore, the peak displacement demand of 2.0 ESS considered in this study is suitable for capturing the effects of imperfections on the lateral response of bearings prior to their full sliding after which almost no deformation occur in bearings.

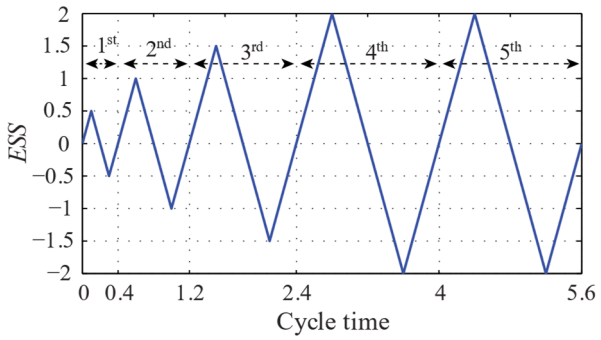

Figure 4.4 Cyclic shear displacement loading protocol

4.3 Finite Element Modeling

The program Abaqus (Dassault Systemes 2019) is used to model the examined bearings. Due to symmetry, only half of each bearing is modelled, and appropriate boundary conditions are imposed at the nodes of the plane of symmetry, i.e., the rotations about the X- and Y-axes and the displacement in the Z direction are constrained. As an example, Figure 4.5(a) shows the full bearing B1TS3 and the corresponding 3D FE model (half bearing).

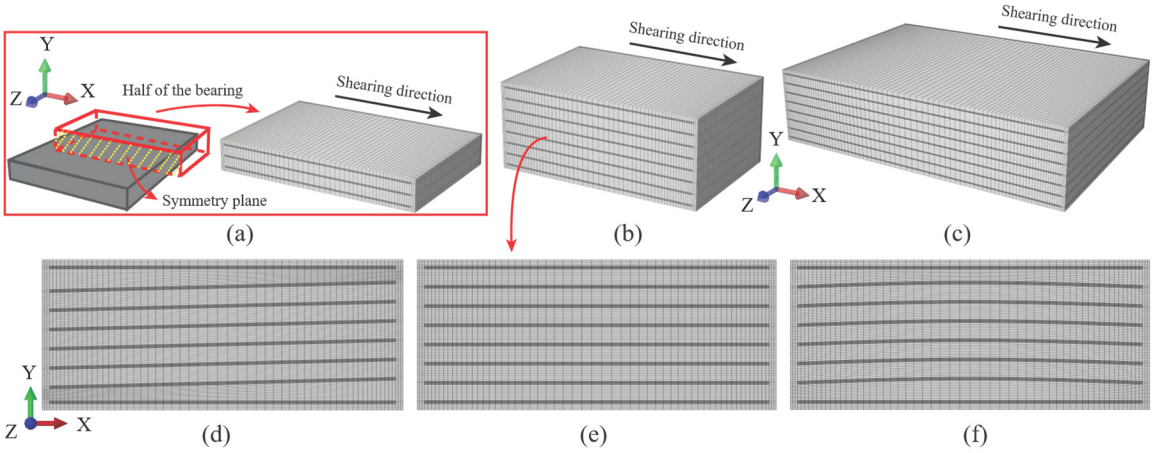

Figure 4.5 (a) 3D FE models of bearing B1TS3 and its half; 3D FE models of the half of the bearings (b) B2TS3; (c) B3TS3; sections on the plane of symmetry of bearings (d) M2T3Sθ25; (e) M2TS3; and (f) M2TS3ρ35

The laminates and the rubber of the bearings are modelled in Abaqus with C3D8I (i.e., 8-node linear continuum element with incompatible modes) elements and C3D8H (i.e., 8-node linear continuum, hybrid element) elements, respectively. These finite element types

are selected given their robust performance in FEA of elastomeric bearings and isolators (Mordini and Strauss 2008; Moghadam and Konstantinidis 2017a; Moghadam and Konstantinidis 2017b; Khaloo et al. 2020; Rastgoo Moghadam and Konstantinidis 2021). For example, hybrid elements are necessary to prevent ill-conditioning and volumetric-mesh-locking issues of the nearly incompressible rubber, and the addition of incompatible modes are necessary to prevent shear locking of the laminates (Dassault Systemes 2019). A mesh sensitivity study was conducted for the output parameters of interest including the total lateral reaction forces of bearings and the peak von Mises stresses and plastic strains in laminates at 2.0 ESS. The results informed mesh size choices. In summary, the FE models of the bearings with B1 and B2 geometries are discretized using 60 and 35 elements along the X and Z axes, respectively; while for the B3 geometry 85 and 50 elements are used in these directions. Finer meshes are used close to the sides of the bearings to handle the increased distortion there compared to the central regions. The element size along the vertical direction is selected to be 1 mm in the laminates, while in the rubber it ranges from 0.8 to 2 mm. The FE models consist of a total number of elements varying from 80,000 to 400,000, depending on the geometry.

Friction is usually the major source for retaining bearings in their position. Experimental studies have shown that: (a) a relatively wide range of potential friction thresholds for these bearings depending on the roughness of the contacting surfaces (Muscarella and Yura 1995) and depending on the compression level and the shearing velocity (Schrage 1981; Steelman et al. 2012; Xiang and Li 2017; Wu et al. 2018), and (b) the friction coefficient, denoted in this paper as μ, is directly proportional to the shearing velocity and inversely proportional to the normal pressure (Schrage 1981; Steelman et al. 2012; Xiang and Li 2017; Wu et al. 2018). Li et al. (2017) conducted quasi-static tests under imposed average pressures of 4–8 MPa to investigate the sliding behavior of bearings in contact with steel interfaces and observed that μ can vary from 0.15 to 0.4 depending on the average pressure. Wu et al. (2018) reported μ values ranging from 0.09 to 0.24 for bearings under testing conditions similar to those of Li et al. (2017). Table 4.4 lists expressions found in the literature for μ that depend on one or two of the following variables: average pressure σ_v,

shearing velocity v_b, and cumulative slip travel δ_{trv} for the unbonded bearing. The first expression in Table 4.4, appears in the European standard ECS (2005) for unbonded bearings subjected to service-level loads. The next three expressions in Table 4.4 have been proposed by Schrage (1981), Magliulo et al. (2011), and Steelman et al. (2012) based on the results of quasi-static tests at low loading rates, while the last expression (by Xiang and Li (2017)) is the only one that considers the combined effects of v_s and σ_v. The expression established by Steelman et al. (2012) accounts for the degradation of μ due to δ_{trv} through the term $\sum \delta_{trv}/100$. For the range of displacements imposed on the examined bearings in the present study, the maximum degradation of μ (due to δ_{trv}) would be negligible. In Table 4.4, the last expression (by Xiang and Li (2017)) is found the most appropriate one because it is the only one that considers the combined effects of v_s and σ_v. According to this relation, μ initially increases rapidly with v_s and levels off and becomes almost independent of v_s for v_s > 20 mm/s. Under such shearing velocities and the average pressure imposed on the bearings in this study, the second part of this expression, i.e., $(1.09\sigma_v^{-0.59} - 1.02\sigma_v^{-0.72}) \times e^{-0.39v_s}$, becomes very close to zero. Therefore, for seismic excitations (featuring high velocities), this expression is reasonably well simplified to $\mu = 1.09\sigma_v^{-0.59}$. For σ_v = 5.5 MPa (i.e., the average pressure on the examined bearings in the present study) to this equation gives μ = 0.4. This constant friction coefficient value is used with the *Coulomb friction* model for the contact definition between the bearing and the loading plates in the FEA. The friction model is used because of its implementation simplicity and its capability in providing reasonable representation of friction behavior at such interfaces (Han 2016; Huang et al. 2018; Khaloo et al. 2020). It is also noted that μ = 0.4 was also reported by Xiang et al. (2018) based on shake table tests on bearings in contact with steel surfaces, and it is close to the μ = 0.35 recommended by Caltrans (1994) for the seismic analysis of elastomeric bearings in contact with steel surfaces. Finally, at the interior steel–rubber interfaces of the bearings, the continuity constraints are imposed by merging the coinciding nodes there. This modeling assumption is made because shear delamination at the rubber-laminate interfaces has not been reported in any studies of unbonded bearings experiencing

moderate monotonic axial loads followed by several lateral displacement cycles with amplitude of 2.0 ESS, or even larger (Mori et al. 1999; Steelman et al. 2012; Wu et al. 2018). In contrast to what occurs in fully bonded bearings, in unbonded bearings, tensile stresses at steel-elastomer interfaces (which are caused by mainly the unbalanced moment arising from P-delta effect due to the simultaneous actions of shear and compression) are limited because of roll-off of their top or bottom surfaces (Kelly and Konstantinidis 2011; Konstantinidis and Kelly 2012).

Table 4.4 Friction coefficients for elastomeric bridge bearings

Friction coefficient, μ	Contact surface	Reference
$0.1 + 0.9/\sigma_v$	Rubber-Concrete	ECS (2005)
$0.05 + 0.4/\sigma_v$	Rubber-Concrete	Schrage (1981)
$0.1 + 0.055/\sigma_v$, for $0.14 \le \sigma_v \le 5$	Rubber-Concrete	Magliulo et al. (2011)
$0.18 + 0.37/\sigma_v - \sum \delta_{trv}/100$	Rubber-Concrete	Steelman et al. (2012)
$1.09\sigma_v^{-0.59} - (1.09\sigma_v^{-0.59} - 1.02\sigma_v^{-0.72}) \times e^{-0.39 v_b}$	Rubber-Steel	Xiang and Li (2017)

σ_v in MPa, δ_{trv} in m, v_b in mm/s

In the FE models of the bearings, the A36 steel is modeled as an isotropic, elastic–plastic material using the stress–strain curve in Figure 4.1(b), and rubber is modeled as a hyperelastic material in conjunction with a hysteresis model. The Yeoh hyperelastic model (Yeoh 1993) is used to characterize the nonlinear elastic response of the neoprene rubber because of its ability to accurately represent hardening under large shear strains (Sun 2015; Moghadam and Konstantinidis 2017a; Ahmadi Soleimani et al. 2021). The 3-term Yeoh model in Abaqus (Dassault Systemes 2019) differs slightly in appearance from that of the original work by (Yeoh 1993) and expresses the strain energy density (stored energy per unit volume) as a function of the material parameters C_{10}, C_{20}, and C_{30}, which are related to the deviatoric part of the Cauchy-Green deformation tensor, and D_1, D_2, and $D3$, which are related to the compressibility. The hysteresis model is based on the model developed by Bergström and Boyce (1998) and has been used in past studies to represent the hysteretic behavior of rubbers (Belivanis 2017; Kalfas et al. 2020; Khaloo et al. 2020). This model is defined in Abaqus by four unitless parameters, namely, the stress scaling factor S_{SF} (the main parameter influencing the damping ratio), the effective stress exponent m, the creep

strain exponent C, and the creep parameter A. More details about the 3-term Yeoh and hysteretic models used can be found in Ahmadi Soleimani et al. (2021) and the Abaqus user manual (Dassault Systemes 2019), respectively. The bulk modulus of the considered neoprene is about 340 ksi (2345 MPa) (Belivanis et al. 2015), which gives the values of D_1 = 0.0008529 MPa^{-1}, D_2 = 0.0 MPa^{-1}, and D_3 = 0.0 MPa^{-1}. A regression analysis was conducted to calibrate parameters pertaining to the deviatoric part of deformation (i.e., C_{10}, C_{20}, C_{30}, S_{SF}, m, C, and A) with the simple shear test data of the neoprene elastomer (see Figure 4.1(a)). Table 4.5 lists the eight calibrated parameters, and Figure 4.6shows how well the calibrated model fits the test data.

Table 4.5 Calibrated parameters of the hysteretic hyperelastic model for neoprene using simple shear test data

Category	Parameter	Value	Unit
Yeoh model constants	C_{10}	0.293	MPa
	C_{20}	-0.0281	MPa
	C_{30}	0.00472	MPa
Hysteretic model	S_{SF}	0.551	-
	A	9.28	-
	m	1.02	-
	C	-0.934	-

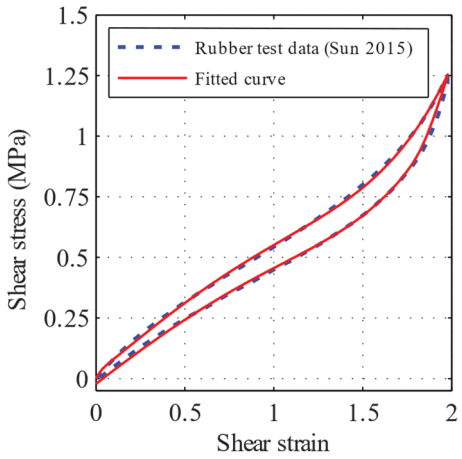

Figure 4.6 Simple shear test data of the neoprene and the fitted curve

The bearings are subjected to axial loads corresponding to the average pressure of 5.5 MPa, followed by the cyclic lateral displacements with the protocol shown in Figure 4.4. In the compression stage, the top loading plate is displaced downward without being allowed to

rotate or displace horizontally while in the shearing stage, the top plate is displaced horizontally without being allowed to rotate. Finally, FEAs are carried out in small increments using a Lagrangian formulation and Newton-Raphson iteration method, and both geometric and material nonlinearities were included.

4.4 Observed Deformation and Displacement Pattern in Elastomeric Bearings

This section discusses the deformation patterns of the examined bearings under compressive loads followed by cyclic lateral displacements. As an illustrative example, Figure 4.7(a) shows the deformed shapes of bearing B2TS2 at four different ESS levels ranging from 0.5 in the first cycle to 2.0 in the fourth and fifth cycles. Similar to the deformed shape of bearing B2TS2 at 0.5 ESS in Figure 4.7(a), all examined bearings experienced mainly shear deformations for ESS ≤ 0.5, essentially acting as bonded bearings. As ESS increased, the corners of the unbonded bearing start to roll off the support surfaces. For bearing B2TS2, this occurs near ESS = 1.0 of the first cycle. At ±2.0 ESS, bearings with B2 and B3 geometries and 2-mm-thick laminates (i.e., B2TS2, B3TS2, B3TS2θ25, and B3TS2ρ35 in Figure 4.7(c,d)) are near the rollover condition. In contrast, the amount of roll-off in bearings with either or both B1 geometry and 4-mm-thick laminates (e.g., B1TS4, B1TS4θ3, B2TS4, and B2TS4ρ45 in Figure 4.7(b,c)) is limited due to either or both their low thickness and the higher flexural resistance of their laminates. Comparison of the deformed shapes of each bearing without imperfection (i.e., B1TS4, B2TS4, and B3TS2) shown in Figure 4.7(b-d) with its corresponding bearings with imperfections shown in Figure 4.7(b-d), indicates that the examined imperfections (i.e. rotationally misaligned or bent laminates) do not cause a notable difference in the overall deformed shapes of the bearings. However, the roll-off amount and subsequently the ESS level at which rollover happens can be affected by imperfections. For instance, at -2.0 ESS, major regions of the vertical sides of bearing B3TS2θ25 contact the support surfaces (see Figure 4.7(d)), while this is not the case at +2.0 ESS. This occurs because in bearing B3TS2θ25, the rotationally misaligned laminates and the resulting lateral bulging of the top and bottom rubber layers makes this bearing roll over easier when it is sheared toward

the left side. This can be considered an undesirable effect because after rollover, further lateral loading on bearings has been observed to cause extensive damage through tearing of the rubber at the their edges if sliding is postponed to ESS values higher than 3.0 (Konstantinidis et al. 2008). Also, it is observed in Figure 4.7(d) that the bent laminates in B2TS2ρ35 makes the initially vertical surfaces in the left and right sides to be deformed slightly differently from each other. Finally, for each examined bearing, the intensities of roll-off in the fourth and fifth cycle at 2.0 ESS differ slightly from each other (e.g., see the differences between the corresponding deformed shapes in Figure 4.7(a)). This is attributed to local slippage happening at the bearing–support interfaces and plastic deformation in the laminates.

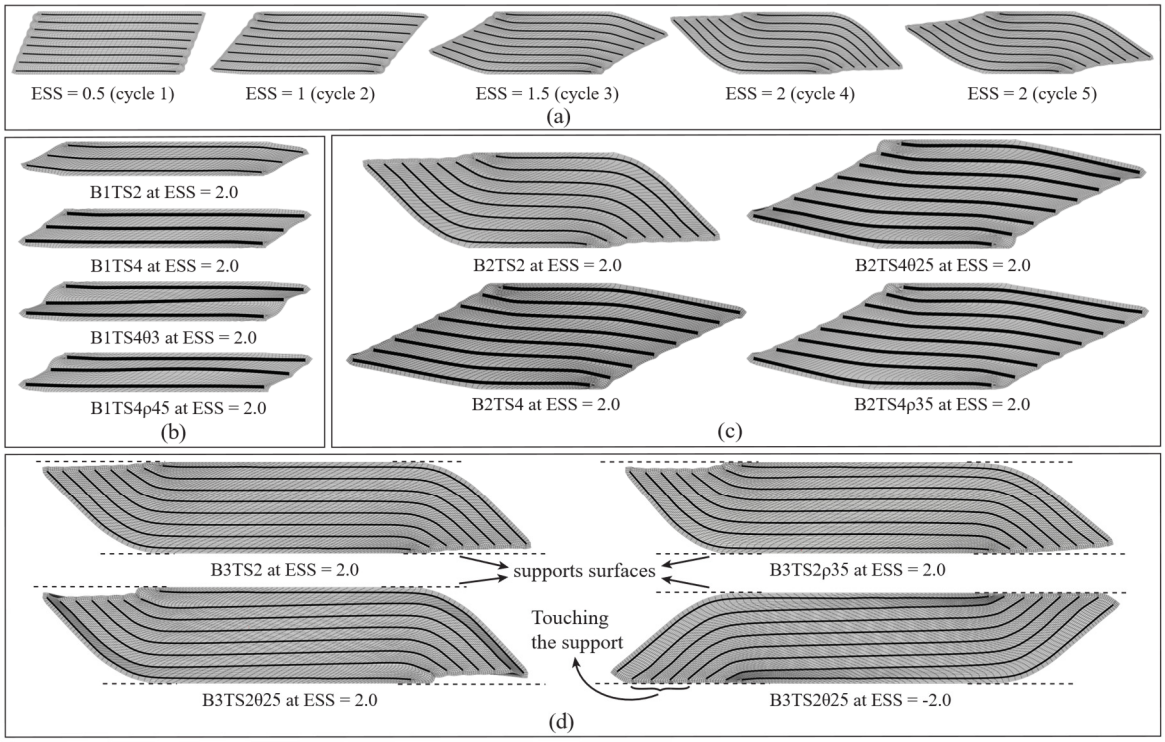

Figure 4.7 Deformed shapes (on XY-plane of symmetry) of (a) bearing B2TS2 and at different ESS levels and (b-d) selected bearings at either ESS = 2.0 or ESS = -2.0

Under average pressures typically allowed in practice (i.e., 1.0 to 7 MPa), bearings have been observed to experience full sliding at ESS values ranging from 1.0 to 2.6 (e.g., Konstantinidis et al. (2008), Steelman et al. (2012), Xiang and Li (2017), and Wu et al.

(2018)) depending on the overall frictional resistance of the contact surfaces relative to the lateral force demand. However, Xiang and Li (2017) noted that prior to full sliding, minor local slippage starts and develops quasi-statically at different portions of the bearing–support interfaces. Such local slippage can result in minor sliding displacements (denoted as *walking displacements*) of the bearing, but the relative displacement between the supports is predominantly accommodated by shearing deformation in the elastomer. In this study, the potential sliding and cumulative slip travel are assessed during the cyclic displacement-controlled FEAs. To achieve this, the positions of four nodes of the examined half bearings and loading plates (Figure 4.8), namely, the bearing's top node (N_{BT}), the bearing's bottom node (N_{BB}), the top loading plate's node (N_{PT}), and bottom loading plate's node (N_{PB}) are recorded during the FE analyses. The slip at each interface is defined as any variation in the horizontal distance between each of the two neighboring nodes close to that interface. Therefore, the cumulative slip travel δ_{trv} from the beginning of the analysis up to analysis time t_i, is computed as $\delta_{trv}(t_i) = \sum_{t=0}^{t=t_i} |dx_B(t_i) - dx_B(t_{i-1})| + |dx_T(t_i) - dx_T(t_{i-1})|)$. As shown in Figure 4.8, $dx_B(t_i)$ and $dx_T(t_i)$ define the horizontal distances between the corresponding two neighboring nodes at t_i.

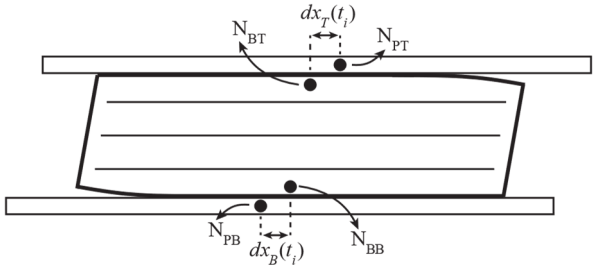

Figure 4.8 Schematic representation of the potential slippage at bearing–support interfaces and at an analysis time

The assessment of δ_{trv} reveals that none of the examined bearings experience full sliding up to ±2.0 ESS, and imperfections have negligible effects on δ_{trv}. The δ_{trv} (which is caused by walking displacements) of all examined bearings except bearings with B2 geometries and 2-mm-thick laminates is limited to 1 mm at the end of 5 cycles. However, the δ_{trv} growth in bearings with B2 geometries and 2-mm-thick laminates is quite different from

those of other bearings. As an illustrative example, Figure 4.9 shows the growth of δ_{trv} for bearing B2TS2 during the five cycles. Figure 4.9 shows that δ_{trv} grows rapidly in two time instances, during each of the last two cycles and at ESS values ranging from 1.39 to 2.0 ESS. For instance, in the first half of the fifth cycle, such a rapid-rate growth of δ_{trv} starts at 1.48 ESS in its loading phase and stops at 1.39 ESS in its unloading phase. These rapid-rate growths of δ_{trv} are mainly attributed to the rapid-rate increase in roll-off amount in this bearing, which eventually leads to the loss of contact at two of the neighboring nodes used for slip measurements during these time periods. Therefore, any further imposed lateral displacement on the top loading plate is then accompanied with marked increase in the horizontal distance between those two neighboring nodes. Through this mechanism, the bearing "walks" on the support surfaces by losing its initial contact with the support surfaces at some regions and contacting some other regions of the support surfaces. Therefore, the growth of δ_{trv} caused by this phenomenon is mainly because of roll-off, and it can be regarded as the walking travel of the bearing. However, it is observed in Figure 4.9, that the δ_{trv} value of about 118 mm at the end of five cycles is still small compared to the total imposed displacements of 2828 mm on bearing B2TS2. In summary, the lack of full sliding up to 2.0 ESS might be considered an undesirable behavior if bearings are intended to provide energy dissipation through friction sliding mechanisms according to the quasi-solation concept (Filipov et al. 2013a).

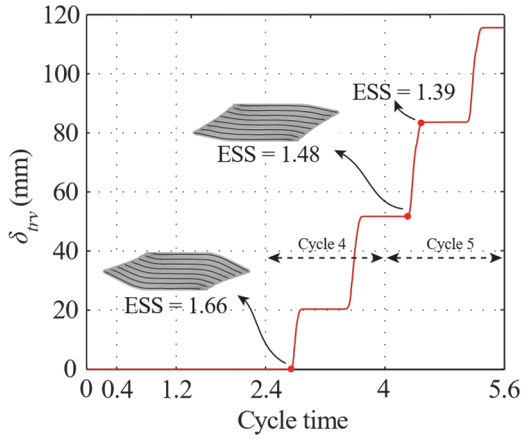

Figure 4.9 The cumulative slip travel, δ_{trv}, of bearing B2TS2 during the cyclic loading

4.5 Hysteretic Responses of the Bearings Without Imperfections

Figure 4.10(a-c) illustrates the 5-cycle shear stress–ESS curves of bearings B1TS2, B2TS2, and B3TS2 (i.e., bearings without imperfections and with 2-mm-thick laminates (TS2) but with different geometry B1, B2, and B3), and Figure 4.10(d-f) illustrates the fifth-cycle shear stress–ESS curves of all the examined bearings without imperfections, in which the shear stress is defined as the ratio of the horizontal force to plan area. From the shear stress–ESS curves shown in Figure 4.10(a-c), the following observations are made: (i) The hysteretic loops maintain their overall shape under multiple displacement cycles, while slight differences exist between the loops of the last two cycles, attributed to the plastic deformation of laminates (which is discussed in Section *Damage in the laminates*), residual walking displacements from the fourth cycle, and differences between the roll-off intensities of the last two cycles. (ii) The bearings without imperfections display relatively narrow hysteretic loops up to ±2.0 ESS, which is attributed to the shear deformation of the (low-damping) neoprene used and the lack of any full sliding at the bearing–support interfaces. The nonlinearity in responses is attributed to both strain-hardening of the rubber and roll-off of the bearings. The strain hardening in the rubber results in increase in the tangent shear stiffness at higher shear strains (Figure 4.10(a)), which is noticeable in short bearings (e.g., bearings with B1 geometry) that experience minimal roll-off. In contrast, the loss of effective shear area (for regions still in contact with the supports) due to roll-off, which is more noticeable in bearings with low second shape factor, i.e., ratio of width to total rubber thickness (e.g., bearings with B2 geometry and 2-mm-thick laminates), results in the degradation of tangent shear modulus at higher ESS values. For instance, the tangent shear modulus of bearing B2TS2 (see Figure 4.10(b)) reaches a low value of 0.15 MPa in cycle 5 at 2.0 ESS, approaching lateral instability. Therefore, bearings with 2-mm thick laminates and second shape factor of 3 (i.e., the minimum allowed in Ontario for the service-level condition) seem to barely avoid instability up to 2.0 ESS. The instability can rapidly move the bearing into an unseated configuration. The graphs in Figure 4.10(d) show that increasing the laminate thickness has almost no effect on the hysteretic response for the B1 bearings without imperfections. This is because the hysteretic response of unbonded

bearings that experience minimal roll-off and slippage is similar to the fully bonded bearings for which the laminate thickness has been also found to have a very small effect on the bearing's hysteretic response (Kalfas et al. 2020). However, in thicker bearings (e.g., B2 and B3 bearings), increasing the laminate thickness can increase the tangent modulus or stiffness at higher ESS values (see Figure 4.10(e,f)). This is attributed to the reduction of roll-off amount in such bearings due to the higher flexural stiffness of the thick laminates that resist the bearing's roll-off. The resulting stiffness increase might promote full sliding in lower shear strains and thus increase their energy dissipation at larger shear strains, which can be suitable for the quasi-isolation purposes (Filipov et al. 2013a). Also, in slender bearings (having low second shape factor), instability might occur before sliding. For instance, Konstantinidis et al. (2008) observed a rapid-rate roll-off of a tested slender bearing with 1.9-mm-thick laminates and a second shape factor of 1.84, which led to instability at approximately 1.5 ESS. Considering the observed effects of laminate thickness on the roll-off of bearings with B2 geometry (Figure 4.7(c)) and on their tangent stiffness (Figure 4.10(e)), it can be concluded that the increase in laminate thickness in slender bearings can effectively prevent their potential instability under large displacements. However, instability is not generally a concern in short bearings, and the roll-off amount in short bearings with even thin laminates (e.g., bearing B1TS2) is already small at 2.0 ESS. Finally, it is noted that for the examined bearings, increasing the laminate thickness could cause only slight increases in the tensile stresses induced in very small regions of the steel-elastomer interfaces, which might potentially lead to local debonding at larger displacement amplitudes.

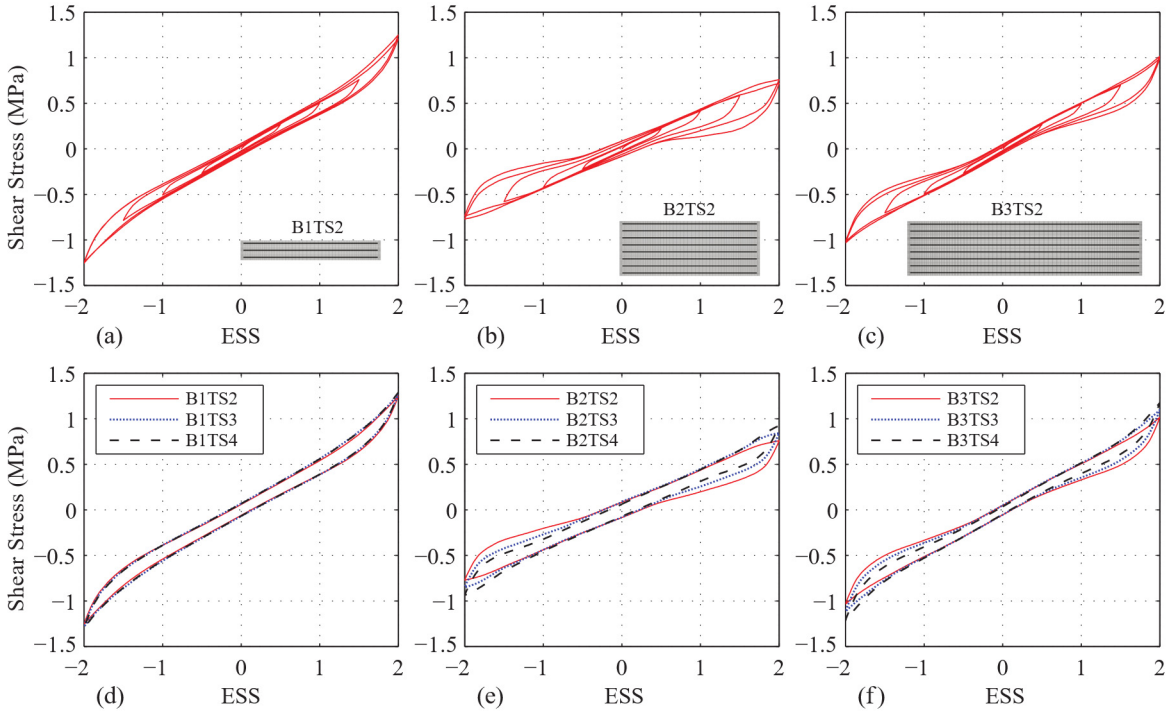

Figure 4.10 (a-c) Hysteretic responses of bearings B1TS2, B2TS2, and B3TS2 subjected to the five-cycle loading protocol; (d-f) fifth-cycle hysteretic loops of all bearings without imperfections and with geometries B1, B2, and B3

4.6 Horizontal Stiffness and Damping Ratio of Bearings without Imperfections

This section focuses on the effective horizontal stiffness and effective damping ratio of the bearings without imperfections to characterize their hysteretic responses and quantify the effects of laminate thickness on their hysteretic responses at different displacement amplitudes. The effective lateral stiffness of these bearings is compared with the nominal horizontal stiffness, $K_h = GA_h/t_r$, where G = shear modulus of the rubber, A_h = bearing's plan area, and t_r = total rubber thickness. The effective lateral stiffness, K_{eff}, hereinafter referred to simply as *stiffness*, and effective damping ratio, ξ_{eff}, are calculated at the displacement amplitude $D = \text{ESS} \times t_r$ as

$$K_{eff} = \frac{F_{max} - F_{min}}{2D} \quad \text{and} \quad \xi_{eff} = \frac{W_D}{2\pi K_{eff} D^2}, \tag{4.1}$$

respectively, where F_{min} = lateral force at -ESS; and F_{max} = lateral force at +ESS; and W_D = hysteretic area (energy dissipated per cycle). The comparison between K_{eff} and K_h values of the bearings is done using the normalized stiffness $\overline{K}_{eff} = K_{eff}/K_h$.

$\overline{K}_{eff}$ and ξ_{eff} of the examined bearings are calculated at ESS levels 0.5, 1.0, 1.5, and 2.0 reflecting cycles 1, 2, 3, and 4 or 5, respectively. Figure 4.11(a) shows graphs of $\overline{K}_{eff}$ against these ESS levels for the bearings without imperfections with 2- and 4-mm-thick laminates. In Figure 4.12(a), each displayed data point at the ESS level 2.0 corresponds to the calculated $\overline{K}_{eff}$ at either cycle 4 or cycle 5 that shows the maximum variation of $\overline{K}_{eff}$ with respect to its corresponding value at the ESS level 1.5. The following observations can be drawn from Figure 4.12(a): (i) For the plotted range of ESS values, the bearings' stiffnesses are always less than their corresponding K_h values, and K_h formula may not provide an accurate stiffness estimation. (ii) The bearings' stiffnesses ranges from about 55% to 100% of their corresponding K_h values depending on the bearing geometry and the target ESS level. This large difference is attributed to various effects, including the roll-off, the flexural deformation in the laminates, the applied axial load, the walking displacements of the bearing, the strain hardening of the rubber, and the presence of side covers all around the bearings. (iii) As the ESS increases from 0.5 to 2.0, bearing B1TS4 and bearing B2TS2 experience the largest stiffness increase by 16% and decrease by 19%, respectively. This is related to the aforementioned fact that roll-off reduces the stiffness (more pronouncedly in tall bearings with thin laminates), while the strain hardening of the rubber increases stiffness (more pronouncedly in short bearings with thick laminates).

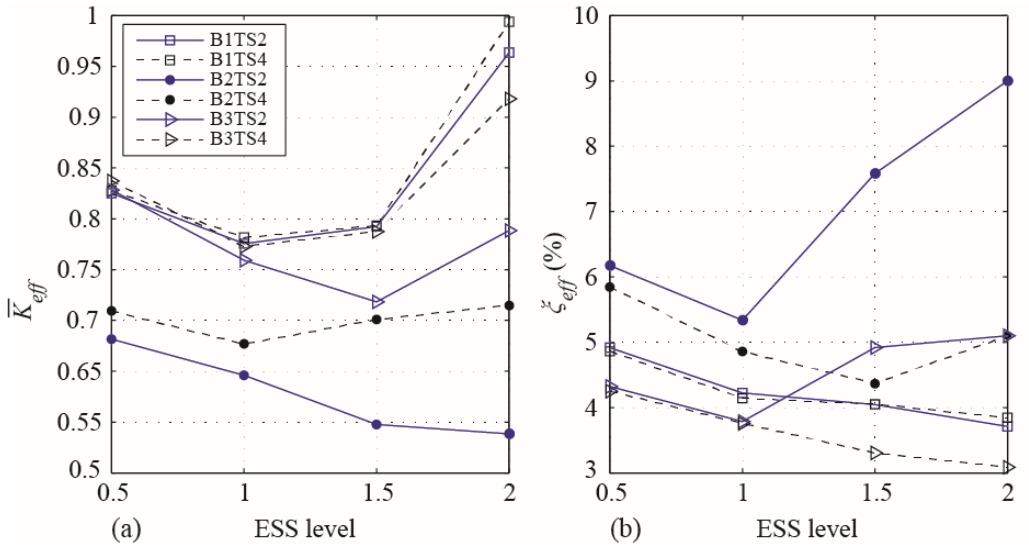

Figure 4.11 (a) $\overline{K}_{eff}$ and (b) ξ_{eff} of examined bearings with imperfections and with 2- and 3-mm-thick laminates at different ESS levels

Similar to Figure 4.12(a), Figure 4.12(b) shows graphs of ξ_{eff} against the ESS levels for the bearings without imperfections and with 2- and 4-mm-thick laminates, from which the following observations can be drawn: (i) For each bearing, the overall relationship between ξ_{eff} and ESS usually contrasts with the overall relationship between $\overline{K}_{eff}$ and ESS, which is expected based on the definition of ξ_{eff}. However, in bearing B2TS2, the rapid increase in ξ_{eff} with the increase in ESS is attributed to not only the stiffness reduction but also the increase in energy dissipation due to extensive plastic deformations in the laminates and walking displacement of the bearing. (ii) ξ_{eff} ranges from 3% for bearing B1TS4 to 9% for bearing B2TS2, both of which corresponds to ξ_{eff} at 2.0 ESS. Therefore, up to 2.0 ESS and before full sliding, ξ_{eff} values can reach 40% below or 80% above the nominal 5% typically assumed in design and evaluation, depending on the characteristics of bearings. Moreover, considering both graphs of Figure 4.12(a,b), it is found that increasing the laminate thickness from 2 to 4 mm increases the stiffness by up to about 31% and decreases the damping by up to about 80%, both for bearings with B2 geometry at 2.0 ESS. All in all, a 5% damping and the lateral stiffness calculated using K_h formula might inaccurately characterize the response of a bearing at a design level before their full sliding, and thus

they may not be accurate enough to be used for the equivalent linear models of bearings in the design and evaluation of a bridge.

4.7 Influence of Imperfections on the Hysteretic Response of Bearings

Figure 4.12 illustrates the 5-cycle shear stress–ESS curves of the bearings with imperfections with 2-mm-thick laminates. The hysteretic response is quite similar for a bearing with (Figure 4.12) and without (Figure 4.10) imperfections. However, it is observed that the hysteretic responses of bearings with rotationally misaligned laminates have positive offsets (see Figure 4.12), which are attributed to the asymmetry of these bearings. This asymmetry leads to the development of reaction shear forces when the top plate is displaced downward without being allowed to rotate or displace horizontally during the compression stage. Also, it is observed in Figure 4.12(c) that the tangent stiffness of bearing B3TS2ρ35 increases rapidly at about -2.0 ESS. This is because major regions of the initially vertical sides of this bearing contact the support surfaces due to roll-off (as shown in Figure 4.7(d)), providing considerable resistance.

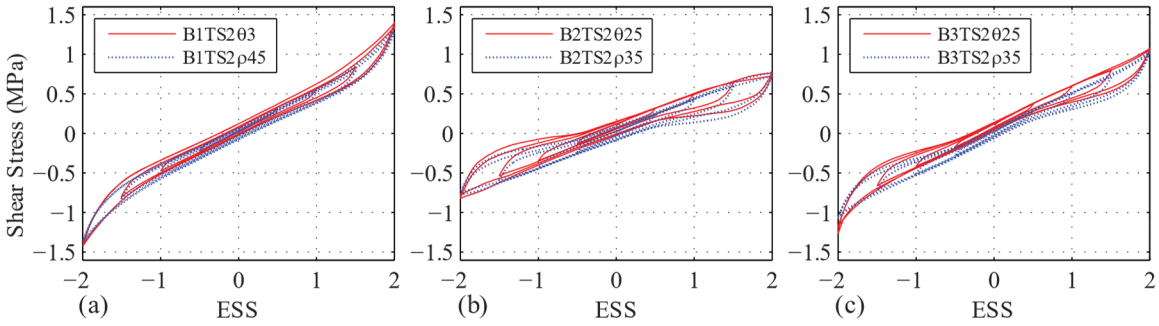

Figure 4.12 5-cycle hysteretic responses of bearings with imperfections and with 2-mm-thick laminates

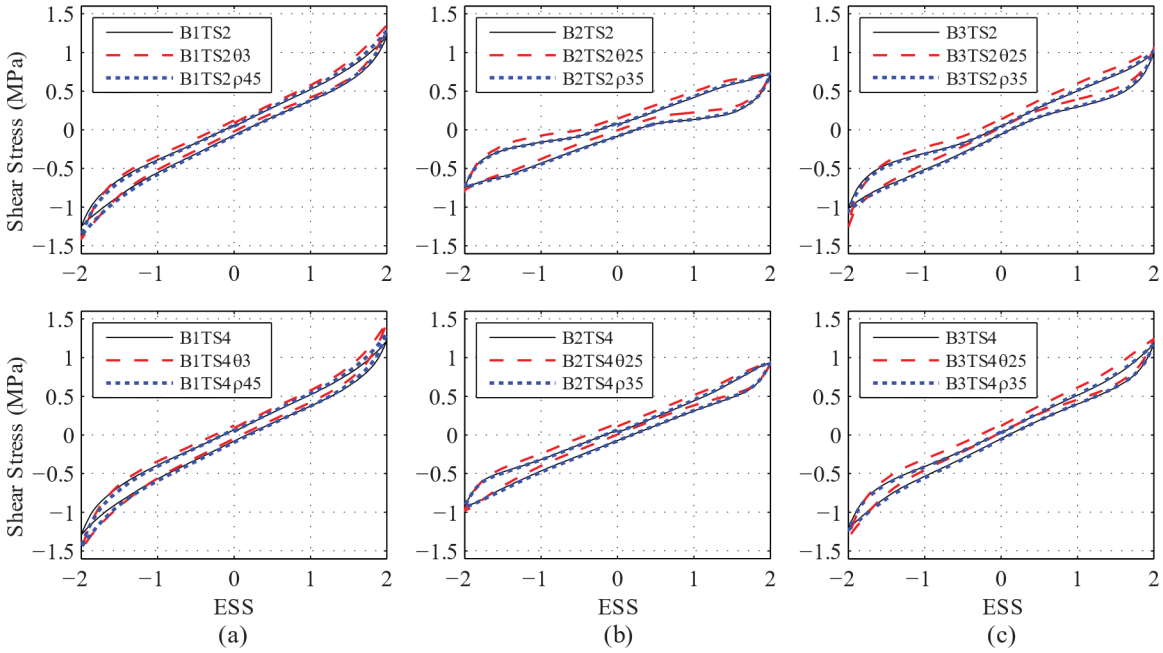

Figure 4.13 Fourth-cycle hysteretic responses of bearings with geometries (a) B1, (b) B2, and (c) B3

To better visualize the influence of imperfections on the hysteretic responses, the fourth-cycle loops of different bearings are illustrated in Figure 4.13. The following observations can be drawn by comparing the graphs in Figure 4.13: (i) As expected from the deformation patterns shown earlier, the laminate imperfection does not cause a considerable difference in the hysteretic responses of bearings but can affect their tangent shear modulus or stiffness specifically at ESS values close to ±2.0. For instance, rotationally misaligned laminates lead to the reduction of tangent stiffness at 2.0 ESS from 0.15 MPa in bearing B2TS2 to 0.07 MPa in bearing B2TS2θ25, increasing the risk of instability. (ii) Imperfections seem to cause the largest increase in tangent stiffness in the short bearings (bearings with B1 geometry). This is because the deformation pattern in short bearings without imperfections is essentially simple shear in the rubber, with entirely negligible deformations in the horizontal laminates, but any laminate imperfection (deviation from being completely horizontal) introduces additional resistance associated with deforming the laminates, which manifests itself in increased tangent stiffness. However, tall bearings (bearings with B2 and B3 geometries) tend to experience large roll-off and thus force their

laminates to flex and rotate according to the roll-off (see laminates of bearings B2TS2, B2TS4, B3TS2 in Figure 4.7(c,d)). In this regard, the shapes of rotationally misaligned and bent laminates can partially conform with the roll-off shape, and thus reduce the opposition of those laminates to the roll-off. For instance, in bearing B3TS2θ25 sheared toward the negative X-axis (see Figure 4.7(d)), the overall shape of rotationally misaligned laminates (θ about positive Z-axis) partially conforms with the roll-off shape. This finally causes extended regions of the initially vertical surfaces of bearing B3TS2θ25 to contact the support surfaces in comparison to when it is sheared toward the positive X-axis (Figure 4.7(d)).

The maximum absolute horizontal force, denoted as F, is assessed together with the K_{eff} and ξ_{eff} in order to quantify the effects of imperfections on the hysteretic responses. In this regard, Figure 4.14 shows the sensitivity of the K_{eff} and F of all the examined bearings to the imperfections at different ESS levels. The top-row and bottom-row graphs reveal the percentage changes of these two quantities with respect to bearings without imperfections, i.e., $\delta K_{eff}/K_{eff0} = (K_{eff} - K_{eff0})/K_{eff0}$ and $\delta F/F_0 = (F - F_0)/F_0$. The top-row graphs in Figure 4.14 show that imperfections increase the stiffness of bearings at different ESS levels. It is observed that the percentage increase in stiffness due to imperfections can either intensify at higher ESS levels (i.e., for short bearings (see top graphs of Figure 4.14(a))) or be fairly constant at different ESS levels (i.e., for bearings with low width-to-rubber-height ratio (see top graphs of Figure 4.14(b))). Additionally, for bearings with B1 geometry, imperfections of thicker laminates cause the largest increase in $\delta K_{eff}/K_{eff0}$, which is more pronounced at higher ESS levels (see Figure 4.14(a)). However, this might not be true for bearings with B2 and B3 geometries because of the earlier mentioned effects of laminate imperfection on the roll-off of these bearings. For instance, rotationally misaligned laminates lead to the contact of major regions of initially vertical surfaces of bearing B3TS2θ25 with the support surfaces at about -2.0 ESS. Once this occurs, the bearing stiffens considerably; this stiffening is evident from the corresponding curve of the top graph of Figure 4.14(c). The top-row graphs of Figure 4.14 also show that at higher ESS

levels, rotationally misaligned laminates cause larger increases in $\delta K_{eff}/K_{eff0}$ compared to bent laminates. In summary, imperfections could increase the bearings stiffnesses up to 5% at 0.5 ESS and up to 18% at 2.0 ESS.

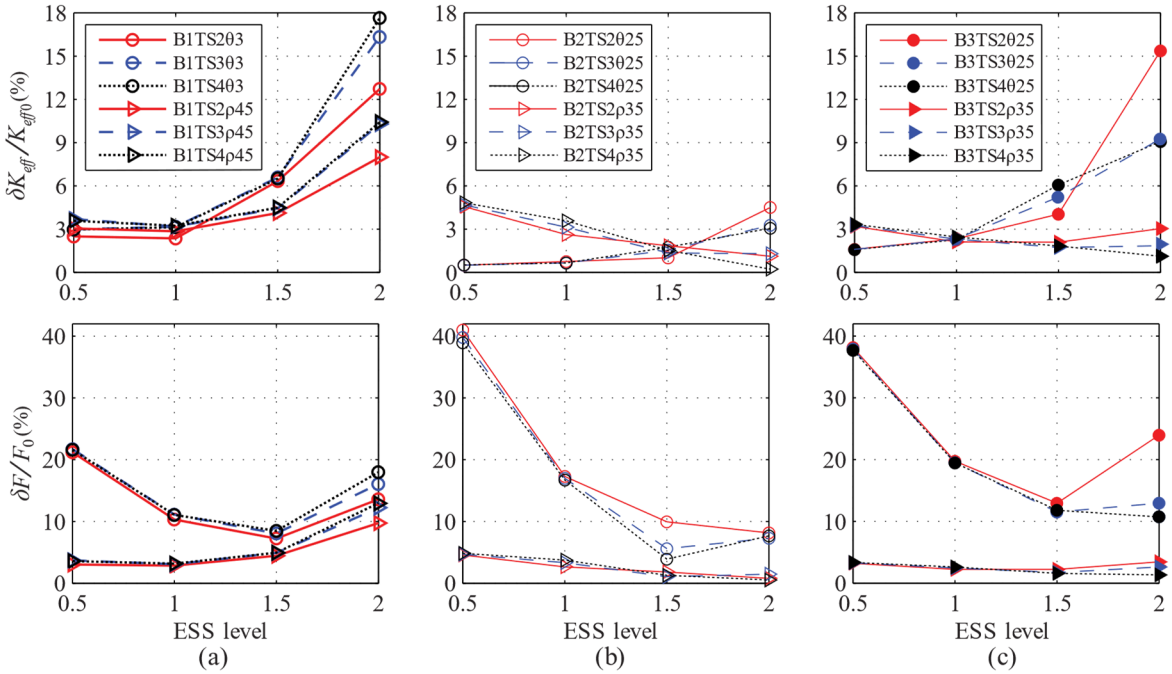

Figure 4.14 Sensitivity of $\overline{K}_{eff}$ and F of bearings with geometries (a) B1, (b) B2, and (c) B3 to the imperfections at different ESS levels

The bottom-row graphs in Figure 4.14 show that F of all bearings increases due to imperfections, with a maximum percentage increase at either 0.5 ESS or 2.0 ESS. For bearings with rotationally misaligned laminates, the increase in F at 0.5 ESS corresponds mainly to the induced reaction force that arises in order to maintain the zero rotation and translation boundary conditions of the top plate during the compression of these asymmetric bearings, which can be up to about 40% in bearings with eight laminates. Although F values at 0.5 ESS are relatively small by themselves, such a 40% increase in F would be at the service-level condition and might be an issue with regard to the serviceability limit states of bridges. The curves that correspond to bearings with bent laminates indicate that this form of imperfection has minor effects on F for bearings with B2 and B3 geometries but can increase F by up to about 13% for bearings with B1

geometry. Rotationally misaligned laminates can also increase F at 2.0 ESS up to 19%, 9%, and 23% in bearings with B1, B2, and B3 geometry, respectively. Also, the relative increase in F due to the examined imperfections (i.e., rotationally misaligned and bent laminates) does not depend on the thickness of the laminates, provided that major portions of the initially vertical surfaces of the bearings do not contact with the support surfaces at the considered ESS level. Note that the lateral force capacity of bearings not experiencing instability would be basically the frictional strength of the interfaces. Considering this and the observed slight effect of imperfections on the overall deformed shapes of bearings, their lateral force capacity is not expected to be notably affected by the imperfections. However, any increase in the stiffness or lateral force of bearings with imperfections at an ESS level before their potential sliding would be equivalent to the increase in the force transmitted to the bridge superstructure under seismic actions. Therefore, this might increase the vulnerability of substructure before their sliding and would be undesirable if it leads to any damage to the substructure components such as piers.

It is noted that the effects of imperfections on ξ_{eff} were studied but found to be marginal and therefore, for the sake of brevity, discussion is kept to a minimum here. In summary, imperfections can increase ξ_{eff} by up to 15% and decrease it by up to 12% depending on the geometry of the bearing, thickness of the laminates, and the ESS level. However, considering the maximum ξ_{eff} value of 9% in the examined bearings without imperfections (see Figure 4.11(b)), these relative changes are rather insignificant.

4.8 Damage in the Laminates

When bearings are subjected to large lateral displacements, their laminates can experience high flexural deformations and yielding due to the roll-off effect. To quantify and compare the intensity and extent of such a potential damage in different bearings and ascertain their vulnerabilities to this kind of damage, this study evaluates the von Mises stress, maximum principal plastic strain, and plastic energy dissipation in the laminates of the examined bearings. To this end, the distribution of von Mises stress and plastic strain is initially

examined for laminates of bearings without imperfections. Then, a strain-based ductility factor, μ_ε, and an energy-based damage factor, Ω_E, are used to assess the *intensity* of plasticity and its *extent*, respectively, in laminates of bearings with or without imperfections. μ_ε is defined as

$$\mu_\varepsilon = \varepsilon_{max}/\varepsilon_{ys} \tag{4.2}$$

where ε_{ys} = yield strain of steel (i.e., 0.0012), and ε_{max} = maximum total (i.e., plastic plus yield strain) principal strain in the laminates. The energy-based damage factor, Ω_E, (proposed by Camara et al. (2017) for distinguishing the damage in different structural members and used by Kalfas et al. (2020) for the damage assessment in fully bonded bearings) is defined as

$$\Omega_E = \sum_j \Omega_j = \sum_j (E_{Sp,\,j}/E_W) \tag{4.3}$$

where j = index that increments over the laminates; $E_{Sp,\,j}$ = plastic energy dissipation in the jth laminate at the end of considered cycle; and E_W = input energy from the application of compressive load and lateral displacement (i.e., the work done by external forces).

Figure 4.15 illustrates the distribution of von Mises stress and maximum principal plastic strain in the laminates of bearings without imperfection and with 2-mm-thick laminates (i.e., B1TS2, B2TS2, and B3TS2), in which the roll-off of corners develops rapidly as ESS increases. Grey color in the von Mises stress contours denotes regions exceeding the yield stress at the indicated ESS level. Similarly, grey color in the maximum principal plastic strain contours shows the plastic regions at the end of cycle 5. The following observations can be derived from the contour plots in Figure 4.15: (i) The extreme values of von Mises stress always occur close to the left and right ends of the laminates, which is attributed mainly to the flexural deformations. (ii) The grey color regions (denoting the yielded regions) are observable first at deformed states corresponding to 1.0 and 1.5 ESS in bearings B2TS2 and B3TS2 and bearing B1TS2, respectively. (iii) At ESS values higher than about 1.5, the plasticity spreads rapidly in the laminates of bearings B2TS2 and B3TS2, and its extent (i.e., the total yielded area) becomes much larger than that of bearing B1TS2. This is attributed to the large roll-off occurring at the corners of bearings B2TS2

and B3TS2. By the end of cycle 5, the plasticity spread over approximately 24%, 75%, and 55% of the total plan areas of all laminates of bearings B1TS2, B2TS2, and B3TS2, respectively. (iv) Shearing of these bearings from the end of cycle 2 to the end of cycle 5 leads to an increase in maximum principal plastic strain by up to 850% and in plasticity extent by up to approximately 2500%. This shows that the plastic damage in sheared bearings tends to spread over the laminates rather than intensify in their critical regions.

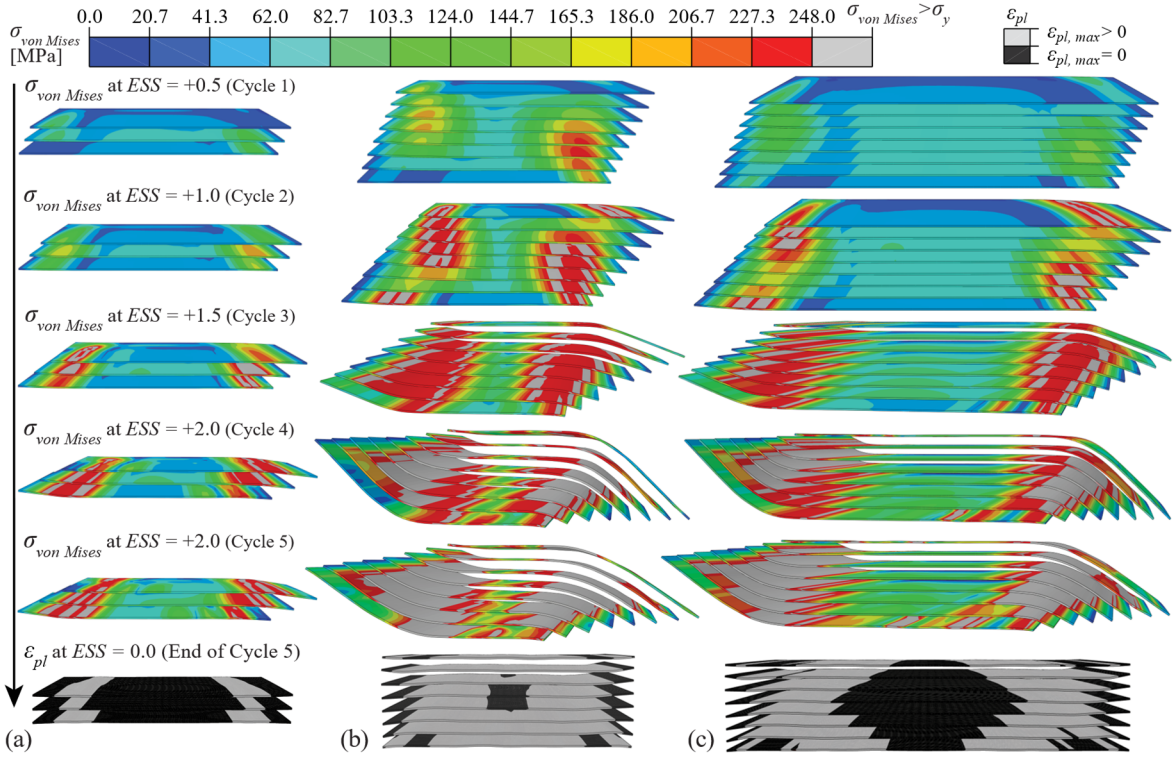

Figure 4.15 Contours of von Mises stress and plastic strain in laminates of bearings (a) B1TS2, (b) B2TS2, and (c) B3TS2

In Figure 4.15, comparison of the grey color areas of the von Mises stress contours, that correspond to cycles 4 and 5 in each bearing, indicates that the plasticity spreads under subsequent cycles of the same amplitude. For instance, the plasticity extents in bearings B1TS2, B2TS2, and B3TS2 increase by approximately 13%, 4%, and 12%, respectively, when they are subjected to cycle 5. The observed spread of plasticity in bearings B1TS2, B2TS2, and B3TS2 indicates that bearings with thin laminates might finally lose their vertical stiffness or become unstable if they are subjected to a large number of displacement

cycles with even the same amplitudes. However, a notable reduction in the vertical stiffness is not expected under excitations of one seismic event because further assessment of the examined bearings shows that their vertical deflection negligibly increases from cycle 1 to the end of cycle 5. Therefore, the laminates of the bearings can effectively constrain the bulging of rubber layers even if the plasticity spread over up to 75% of their total area (i.e., the case for bearing B2TS2). This is because the yielded regions of the laminates in the examined bearings are still in the early portions of the strain hardening stage of the used steel material and are very far from its potential strain softening stage.

The horizontal axes of Figure 4.16 show μ_ε of all laminates in bearings without imperfections subjected to five cycles of lateral displacements, from which the following observations can be made: (i) For bearings with B1 geometry, the μ_ε value of the top and bottom laminates is higher than that of the middle laminate. However, in bearings with B2 and B3 geometries, distribution of μ_ε becomes relatively more uniform along the height of the bearing; and even in bearings B2TS2 and B3TS2, laminates closer to the mid-height experience the maximum μ_ε within that bearing. This observation is attributed to two different deformation mechanisms that induce flexural deformations and plasticity close to the end of the laminates. The first is the roll-off, where laminates flex close to their ends. The FEA shows that in bearings experiencing large roll-off (e.g., B2TS2 and B3TS2 in Figure 4.15), laminates close to the bearing mid-height experience flexural deformations with the most extreme curvatures, and thus experience the most extreme plasticity ratios. The second deformation mechanism is lateral bulging of a rubber layer under compression. In contrast to the first deformation mechanism, this mechanism causes flexing of its adjacent laminates close to their ends that arises when adjacent rubber layers have different thicknesses, and it is mainly observed for the top and bottom laminates because of the thickness difference of their adjacent rubber layer and cover rubber layer. Additionally, when a bearing is sheared, a bending moment distribution develops along the bearing's height which has maximum values at top and bottom, and thus, the bearing experiences additional pressures on the confined rubber close to the ends of the laminates (Kalfas et al.

2020). The roll-off amount in bearings with B1 geometry is limited (see Figure 4.7(b)), and the pressure caused by the axial load and moment induces additional flexural deformations and shear stresses in the top and bottom laminates, resulting in maximum μ_ε within these bearings. (ii) Increasing the laminate thickness from 2 to 3 mm decreases the peak values of μ_ε by up to 58%, 14%, and 27% for the bearings without imperfections with B1, B2, and B3 geometries, respectively. (iii) A further increase from 3 to 4 mm decreases the peak values of μ_ε by up to 14%, 11%, and 34% for the bearings. (iv) Although the μ_ε peak values within the bearings that experience large roll-off (e.g., bearings B2TS2 and B3TS2) are multiple times higher than those within the bearings with thick laminates or limited roll-off (e.g., bearing B1TS4), they are all much smaller than the ductility of mild steel at fracture. All in all, it is comprehensible that designwise the use of thicker laminates (e.g., 4-mm-thick) is safer in especially thick bearings, which can experience large roll-off, while costwise and weightwise the use of thinner laminates (e.g., 2-mm-thick) is preferred. A logical compromise between design and practice would be the use of thicker laminates for the more critical ones (e.g., middle laminates in thick bearings), provided that this would not much complicate the manufacturing. This would be also helpful in reducing the risks of rollover and instability in slender bearings.

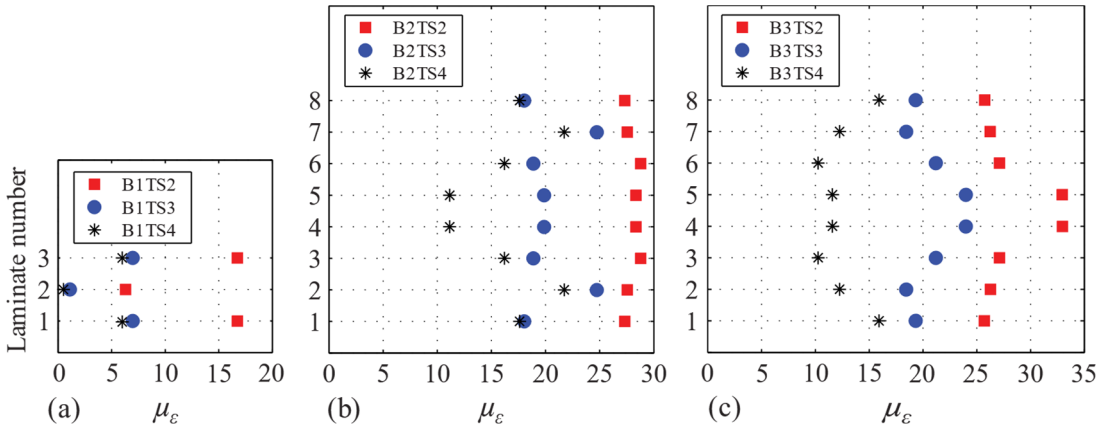

Figure 4.16 μ_ε of laminates in bearings without imperfections and with geometries (a) B1, (b) B2, and (c) B3

Figure 4.17 shows the sensitivity of damage factors Ω_E and μ_ε to the thickness of the laminate for all the examined bearings subjected to the five-cycle loading protocol. Figure 4.17 also provides comparisons of Ω_E and μ_ε values among bearings with and without imperfections. The following observations can be drawn: (i) As the thickness of laminates increases, both damage factors μ_ε and Ω_E decrease considerably in almost all the bearings. For example, an increase in laminate thickness from 2 to 3 mm will decrease μ_ε and Ω_E by up to 73% and 92%, respectively, and a further increase from 3 to 4 mm will decrease μ_ε and Ω_E by up to 34% and 68%. (ii) Imperfections increase both Ω_E and μ_ε for the majority of the bearings. However, for bearings with bent laminates (as an imperfection), the values of these two damage factors are in most cases either very close to or even less than the corresponding values in the corresponding bearings without imperfection. For bearings with B1 geometry, the examined imperfections increase μ_ε and Ω_E by up to 72% and 564%. However, the 564% increase corresponds to the increase in Ω_E from very small value of 0.0045 for bearing B1TS3 to still the small value of 0.03 for bearing B1TS3θ3. The examined imperfections also increase μ_ε and Ω_E by up to 24% and 12% for bearings with B2 geometry and by up to 25% and 63% for bearings with B3 geometry. Although the examined imperfections cause the maximum percentage increase in damage in bearings with B1 geometry, the plastic damage is relatively small in these bearings. For instance, Ω_E in bearings with B1 geometry attains a value of up to 0.1, while it attains a value of up to 0.48 and 0.41 in bearings with B2 and B3 geometry, respectively. The 0.48 value corresponds to bearing B2TS2θ25 and denotes that 48% of the external work is dissipated in the laminates of the bearing. All in all, although the overall plastic damage increases when the imperfections are present or when thinner laminates are used and the bearing experiences large roll-off, all the examined bearings exhibit fairly stable hysteretic loops under the five-cycle loading protocol of this study (as shown in Figure 4.12(b)). Also, in all examined bearings, the induced peak principal plastic strains are still far below the fracture limit of mild steel, and the vertical deflection of all examined bearings is negligibly affected by the induced plastic damage under the five-cycle loading protocol. Therefore,

the increased plastic damage during a strong seismic event in bearings with or without imperfections does not seem to cause an immediate failure (such as laminate fracturing and loss of axial load capacity), provided that the plastic damage and fatigue effects in laminates are minimal prior to the seismic event and under the service-level condition.

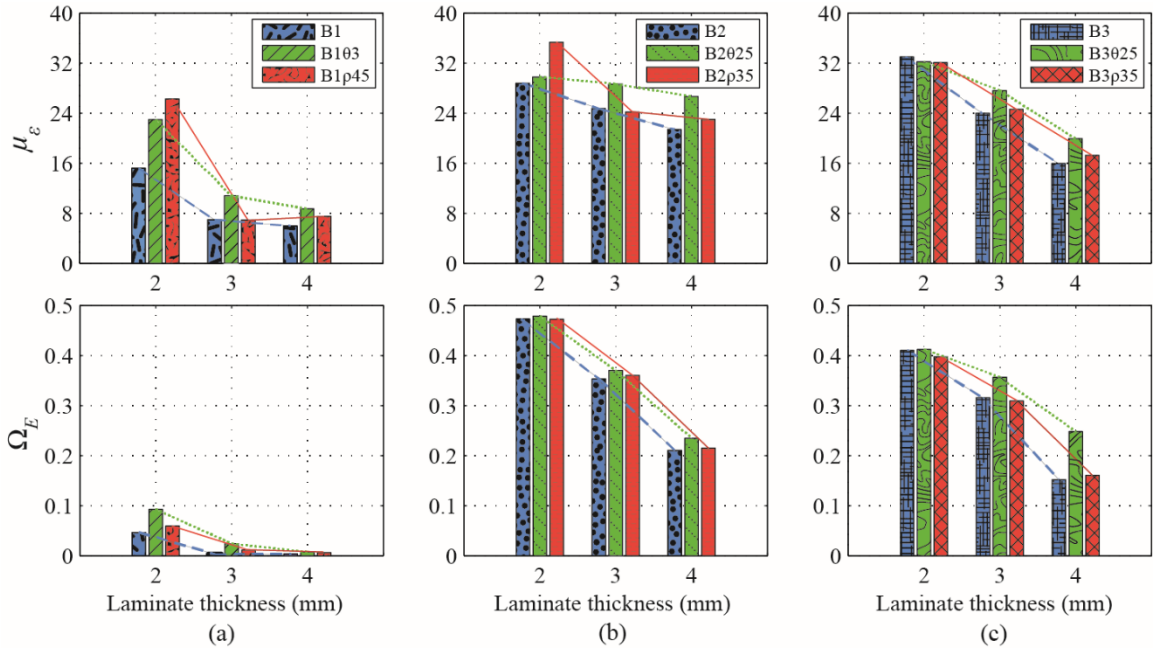

Figure 4.17 Ω and μ_ε of examined bearings with geometries (a) B1, (b) B2, and (c) B3

4.9 Conclusion

This paper investigated the behavior of unbonded elastomeric bridge bearings with and without imperfections and with different steel laminate thicknesses, when subjected to seismic-level demands. The examined imperfections were rotationally misaligned laminates and bent laminates and were examined in bearings with different plan dimensions, number and thickness of laminates, and shape factor. Abaqus was used to develop and analyze the 3D finite element models of the bearings. The models were subjected to axial loads equivalent to an average pressure of 5.5 MPa, followed by five cycles of lateral displacements with increasing amplitude, up to 200% equivalent shear strain. The FEA results were used to assess the deformation patterns and hysteretic

responses of the bearings and quantify the potential damage in the laminates in terms of von Mises stress and maximum principal plastic strain, and plastic energy dissipation.

The main conclusions of the study are:

- Thicker steel laminates in bearings promote a deformation pattern dominated by simple shear, reducing the amount of roll-off at higher shear strains. Increasing the laminate thickness can prevent the potential instability of bearings with low second shape factor (e.g., second shape factor of 3) under large displacements. In this regard, slender bearings with thin steel laminates (e.g., 2-mm-thick) should be avoided.
- For a given laminate thickness, the amount of roll-off can be increased or decreased when imperfections are present in the bearing, depending on the imperfection type (i.e., rotational misalignment or bending) and the shearing direction; most notably, rotationally misaligned laminates can increase the roll-off and expedite the potential rollover of the bearing in lower shear strains. Therefore, slender bearings (i.e., bearings with second shape factor of lower than 3) with rotationally misaligned laminates should be avoided to minimize the risks of rollover and instability.
- The effective lateral stiffness of bearings can be considerably different from their nominal lateral stiffness depending on the target equivalent shear strain and the geometry of the bearing. Therefore, an accurate characterization of the lateral stiffness and also damping based on not only the material description and geometric properties of rubber but also other geometric properties such as laminate thickness and second shape factor and the target equivalent shear strain is needed if equivalent linear models of bearings are used in the design and evaluation.
- The examined imperfections negligibly affected the damping of bearings but increased the effective stiffness and the horizontal force of the bearings by up to 18% and 40%, respectively, at target equivalent shear strains beyond the service-level condition and before sliding. Such increases in the effective stiffness and lateral force occur in short bearings with imperfections and slender bearings with imperfections, respectively. The potential effects of such increases in the response characteristics of bearings on the

vulnerability of other bridge components need to be evaluated before bearings with imperfections are used in a bridge.

- The increase in plastic damage in yielded laminates took the form of increased total yielded area more than the form of increased intensity, and the ductility of the laminates in all examined bearings was much smaller than the ductility of mild steel at fracture. The yielded laminates can effectively constrain the lateral bulging of rubber layers if they experience widespread plasticity but with relatively low ductility. Therefore, in bearings without initial plastic damage or with limited of it, the induced plastic damage during a strong seismic event does not seem to lead to an immediate failure of them.

Future works can focus on studying the performance of fully bonded elastomeric bridge bearings with imperfections under seismic-level demands. Of particular interest would be to investigate the potential effects of imperfections on the tensile stresses induced in these bearings by the vertical force-induced moment (arising due to the combined actions of vertical force and shear deformation). Also, future works are suggested to focus on the system-level behavior of bridges with elastomeric bridge bearings with manufacturing imperfections

Data Availability Statement

All data, models, and code generated or used during the study appear in the submitted article.

Acknowledgments

This research was partially supported by the Ministry of Transportation of Ontario (MTO) through the Highway Infrastructure Innovation Funding Program. The authors are grateful to Kris Mermigas (Head Engineer, Structures Office, MTO) and Ben Huh (Lead Engineer, Structures Office, MTO) for their committed support during this work. Any opinions, findings, or recommendations in this paper are those of the authors and do not necessarily reflect the views of the sponsor.

References

AASHTO. (American Association of State Highway and Transportation Officials). 2017. *AASHTO LRFD bridge design specifications*. Washington, DC: AASHTO.

Ahmadi Soleimani, S., D. Konstantinidis, and G. P. Balomenos. 2020. "Vision-Based Quality Control Testing of Elastomeric Bridge Bearings." In *Proc., Structures Congress,* 651-664. Reston, VA: ASCE.

Ahmadi Soleimani, S., D. Konstantinidis, and G. P. Balomenos. 2021. "Nondestructive assessment of elastomeric bridge bearings using 3D digital image correlation." *J. Struct. Eng.*, 148 (1), 04021233. https://doi.org/10.1061/(ASCE)ST.1943-541X.0003200.

Belivanis, K. V. 2017. "Expanding the use of elastomeric bearings for higher demand applications." Ph.D. thesis, Dept. of Civil, Architectural and Environmental Engineering, The Univ. of Texas at Austin.

Belivanis, K. V., L. Han, C. Sun, T. Helwig, M. Engelhardt, J. Tassoulas, and E. Williamson. 2015. *Extending use of steel-laminated elastomeric bearings to higher demand applications*. *Report 0-6785-1*, Center for Transportation Research, The Univ. of Texas at Austin.

Bergström, J. S., and M. C. Boyce. 1998. "Constitutive modeling of the large strain time-dependent behavior of elastomers." *J. Mech. Phys. Solids.*, 46 (5), 931-954. https://doi.org/10.1016/S0022-5096(97)00075-6.

Caltrans. 1994. *Bridge Memo to Designers*. Section 7: Bridge Bearings. California Department of Transportation, Sacramento, California.

Camara, A., R. Cristantielli, M. A. Astiz, and C. Málaga-Chuquitaype. 2017. "Design of hysteretic dampers with optimal ductility for the transverse seismic control of cable-stayed bridges." *Earthq. Eng. Struct. Dyn.*, 46 (11), 1811-1833. https://doi.org/10.1002/eqe.2884.

CSA. (Canadian Standards Association). 2019. *S6-19 Canadian highway bridge design code*. Section 11: Joints and Bearings. Toronto, Ontario.

Dassault Systemes. 2019. "ABAQUS 2019 Theory manual." *Dassault Systemes Simulia Corp., Providence, Rhode Island*.

ECS. (European Commission for Standardization). 2005. *Structural Bearings-Part 3: Elastomeric Bearings*. Brussels, Belgium.

El-Reedy, M. 2016. *Onshore structural design calculations: Power plant and energy processing facilities*. Butterworth-Heinemann.

Filipov, E. T., L. A. Fahnestock, J. S. Steelman, J. F. Hajjar, J. M. LaFave, and D. A. Foutch. 2013a. "Evaluation of quasi-isolated seismic bridge behavior using nonlinear bearing models." *Eng. Struct.*, 49, 168-181. http://dx.doi.org/10.1016/j.engstruct.2012.10.011.

Filipov, E. T., J. R. Revell, L. A. Fahnestock, J. M. LaFave, J. F. Hajjar, D. A. Foutch, and J. S. Steelman. 2013b. "Seismic performance of highway bridges with fusing bearing components for quasi-isolation." *Earthq. Eng. Struct. Dyn.*, 42 (9), 1375-1394. https://doi.org/10.1002/eqe.2277.

Han, L. 2016. "Elastomeric bearings in high demand applications: Numerical study and experimental Validation." Ph.D. thesis, Dept. of Civil, Architectural and Environmental Engineering, The Univ. of Texas at Austin.

Han, Q., X. Du, J. Liu, Z. Li, L. Li, and J. Zhao. 2009. "Seismic damage of highway bridges during the 2008 Wenchuan earthquake." *Earthq. Eng. Eng. Vib.*, 8 (2), 263-273. https://doi.org/10.1007/s11803-009-8162-0.

Huang, W., X. Xu, K. Wang, and W. Liu. 2018. "Numerical Simulation of Steel-Laminated Bearing Considering Friction Slipping." *International Journal of Engineering and Technology*, 10 (2). https://doi.org/10.7763/IJET.2018.V10.1052.

IDOT. (Illinois Department of Transportation). 2012. *IDOT Bridge Manual*. Springfield, IL.

Kalfas, K. N., S. A. Mitoulis, and D. Konstantinidis. 2020. "Influence of Steel Reinforcement on the Performance of Elastomeric Bearings." *J. Struct. Eng.*, 146 (10), 04020195. https://doi.org/10.1061/(ASCE)ST.1943-541X.0002710.

Kawashima, K., S. Unjoh, J.-I. Hoshikuma, and K. Kosa. 2011. "Damage of bridges due to the 2010 Maule, Chile, earthquake." *J. Earthq. Eng.*, 15 (7), 1036-1068. https://doi.org/10.1080/13632469.2011.575531.

Kelly, J. M., and D. Konstantinidis. 2011. *Mechanics of rubber bearings for seismic and vibration isolation*. Chichester, UK: John Wiley & Sons.

Khaloo, A., A. Maghsoudi-Barmi, and M. E. Moeini. 2020. "Numerical parametric investigation of hysteretic behavior of steel-reinforced elastomeric bearings under large shear deformation." *Structures*, 26, 456-470. https://doi.org/10.1016/j.istruc.2020.04.029.

Konstantinidis, D., and J. M. Kelly. "Two low-cost seismic isolation systems." In *Proc., 15th world conference on earthquake engineering. Lisbon, Portugal,* 24-28.

Konstantinidis, D., J. M. Kelly, and N. Makris. 2008. *Experimental investigation on the seismic response of bridge bearings*. *Report EERC-2008/02*, Earthquake Engineering Research Center, University of California, Berkeley.

Kumar, A. 2001. "Performance related parameters of elastomeric bearings." Ph.D. Dissertation, Dept. of Civil, Architectural and Environmental Engineering, The Univ. of Texas at Austin.

Li, J., T. Peng, and Y. Xu. 2008. "Damage investigation of girder bridges under the Wenchuan earthquake and corresponding seismic design recommendations." *Earthq. Eng. Eng. Vib.*, 7 (4), 337-344. https://doi.org/10.1007/s11803-008-1005-6.

Li, Y., Q. Li, and Q. Wu. 2017. "Ultimate shear performance and friction sliding response of laminated elastomeric bridge bearings." *J. Vibroengineering*, 19 (8), 6301-6312. https://doi.org/10.21595/jve.2017.18321

Liu, K.-Y., K. C. Chang, and B. X. Wu. "The role of rubber bearings of the bridges during the 1999 Taiwan Chi-Chi earthquake." In *Proc., 8th US National Conference on Earthquake Engineering 2006,* 7307-7316.

Luo, J., L. A. Fahnestock, D. L. Kozak, and J. M. LaFave. 2017. "Seismic analysis incorporating detailed structure–abutment–foundation interaction for quasi-

isolated highway bridges." *Struct. Infrastruct. Eng.*, 13 (5), 581-603. https://doi.org/10.1080/15732479.2016.1177094.

Magliulo, G., V. Capozzi, G. Fabbrocino, and G. Manfredi. 2011. "Neoprene–concrete friction relationships for seismic assessment of existing precast buildings." *Eng. Struct.*, 33 (2), 532-538. https://doi.org/10.1016/j.engstruct.2010.11.011.

Moghadam, S. R., and D. Konstantinidis. 2017a. "Finite element study of the effect of support rotation on the horizontal behavior of elastomeric bearings." *Compos. Struct.*, 163, 474-490. http://dx.doi.org/10.1016/j.compstruct.2016.12.013.

Moghadam, S. R., and D. Konstantinidis. 2017b. "Simple mechanical models for the horizontal behavior of elastomeric bearings including the effect of support rotation." *Eng. Struct.*, 150, 996-1012. http://dx.doi.org/10.1016/j.engstruct.2017.07.079.

Mordini, A., and A. Strauss. 2008. "An innovative earthquake isolation system using fibre reinforced rubber bearings." *Eng. Struct.*, 30 (10), 2739-2751. http://dx.doi.org/10.1016/j.engstruct.2008.03.010.

Mori, A., P. J. Moss, N. Cooke, and A. J. Carr. 1999. "The behavior of bearings used for seismic isolation under shear and axial load." *Earthquake Spectra*, 15 (2), 199-224. https://doi.org/10.1193%2F1.1586038.

Muscarella, J. V., and J. Yura. 1995. "An experimental study of elastomeric bridge bearings with design recommendations." Ph.D. thesis, Center for Transportation Research, The University of Texas at Austin.

NYSDOT. (New York State Department of Transportation). 2019. *NYSDOT Bridge Manual*. Section 12: Bridge Bearings.

OPSS. (Ontario Provincial Standard Specification). 2017. *Material specification for bearings - elastomeric plain and steel laminated*.

Rastgoo Moghadam, S., and D. Konstantinidis. 2021. "Experimental and Analytical Studies on the Horizontal Behavior of Elastomeric Bearings under Support Rotation." *J. Struct. Eng.*, 147 (4), 04021024. https://doi.org/10.1061/(ASCE)ST.1943-541X.0002962.

Schrage, I. "Anchoring of bearings by friction." In *Proc., Joint sealing and bearing systems for concrete structures, world congress on joints and bearings,* American Concrete Institute Niagara Falls, NY, USA.

Steelman, J. S., L. A. Fahnestock, E. T. Filipov, J. M. LaFave, J. F. Hajjar, and D. A. Foutch. 2012. "Shear and friction response of nonseismic laminated elastomeric bridge bearings subject to seismic demands." *J. Bridge Eng.*, 18 (7), 612-623. http://dx.doi.org/10.1061/(ASCE)BE.1943-5592.0000406.

Sun, C. 2015. "Material study of the steel reinforced elastomeric bridge bearings." Ph.D. thesis, Dept. of Civil, Architectural and Environmental Engineering, The Univ. of Texas at Austin.

Wu, G., K. Wang, G. Lu, and P. Zhang. 2018. "An Experimental Investigation of Unbonded Laminated Elastomeric Bearings and the Seismic Evaluations of Highway Bridges with Tested Bearing Components." *Shock and Vibration*, 2018. https://doi.org/10.1155/2018/8439321.

Xiang, N., M. S. Alam, and J. Li. 2018. "Shake table studies of a highway bridge model by allowing the sliding of laminated-rubber bearings with and without restraining devices." *Eng. Struct.*, 171, 583-601. https://doi.org/10.1016/j.engstruct.2018.05.121.

Xiang, N., Y. Goto, M. S. Alam, and J. Li. 2021. "Effect of bonding or unbonding on seismic behavior of bridge elastomeric bearings: lessons learned from past earthquakes in China and Japan and inspirations for future design." *Advances in Bridge Engineering*, 2 (1), 1-17. https://doi.org/10.1186/s43251-021-00036-9.

Xiang, N., and J. Li. 2017. "Experimental and numerical study on seismic sliding mechanism of laminated-rubber bearings." *Eng. Struct.*, 141, 159-174. http://dx.doi.org/10.1016/j.engstruct.2017.03.032.

Yeoh, O. H. 1993. "Some forms of the strain energy function for rubber." *Rubber Chemistry and technology*, 66 (5), 754-771. https://doi.org/10.5254/1.3538343.

Yura, J., A. Kumar, A. Yakut, C. Topkaya, E. Becker, and J. Collingwood. 2001. *Elastomeric bridge bearings: Recommended test methods*. *Report NCHRP 449*, National Cooperative Highway Research Program (NCHRP), Washington, DC: Transportation Research Board.

Zhang, R., and A. Li. 2019. "Finite element study of effect of parameters on stress distribution of steel shim in elastomeric bearings." *Adv. Struct. Eng.*, 22 (9), 2124-2135. https://doi.org/10.1177/1369433219834748.

5 Summary, Conclusion, and Recommendations

This chapter summarizes the most important findings of this work and recommends some areas for further research.

5.1 Summary

Elastomeric bridge bearings are generally manufactured using compression molding wherein the flow of rubber inside the mold might misalign the steel laminates vertically and rotationally or force them to bend. In this regard, bridge codes (OPSS 2017; AASHTO 2018) specify certain design tolerances, which requires destructive testing of elastomeric bearings according to the current quality control procedures. This type of testing is also costly and time-consuming. To address this, the first objective of this study was to develop an efficient nondestructive methodology for quality control testing of elastomeric bearings. Then, once manufacturing imperfections are detected and quantified, the question that arises is: what is their effect on the performance of elastomeric bearings? Studies aimed at answering this question have been very scarce, and the logic behind the majority of current design tolerances for imperfections in bridge codes (OPSS 2017; AASHTO 2018) is not clearly presented. Therefore, the second and third objectives of this study were to investigate the effects of different forms of manufacturing imperfections (vertically misaligned, rotationally misaligned, and bent steel laminates) on the performance of elastomeric bearings under the service-level condition and beyond service-level conditions, respectively. The main findings of the work presented in this dissertation and potential areas of future research are outlined in the following sections.

5.2 Conclusions

5.2.1 Vision-based Quality Control Testing of Elastomeric Bearings Using 3D-DIC

3D FEAs were conducted on different models of elastomeric bearings to develop a nondestructive quality control procedure based on the displacements and strains on the surface of bearings. Consequently, a methodology involving an error correction procedure was developed, enabling accurate identification of the vertical positions of steel laminates

and thickness of side cover at any location within the bearings. Then, 3D-DIC (which is needed to apply the methodology) was implemented during the compression testing of two elastomeric bearings to assess its applicability for measuring the fields of displacement and strains on the vertical surface of the bearings. Different elements of 3D-DIC including the application of speckle pattern on the bearings' surfaces, implementation of the stereo-camera system, and postprocessing of the recorded images were done meticulously. Then, the methodology was applied using the 3D-DIC measurements on the surfaces of tested bearings in compression. The main findings are:

- Local extrema on the fields of in-plane vertical strain and horizontal displacement can reasonably well identify the locations of steel laminates in elastomeric bearings subjected to relatively low compressive loads.
- 3D-DIC can accurately measure the full spatial field of displacement and strain on the surface of bearings.
- The predictions of the important geometrical aspects of the bearings using the methodology were in a very good agreement with the actual values, determined by destructive testing (cutting the bearings open).
- The developed methodology for quality control testing requires only the implementation of 3D-DIC during the compression testing of elastomeric bearings and then postprocessing of the measured data.
- It is noted that while the *development* of the proposed methodology involved FEA, the future *application* of the methodology does not require any FEA.

5.2.2 Service-Level Performance of Elastomeric Bearings

Following the proposed methodology for quantifying the important geometrical properties of bearings such as potential manufacturing imperfections, an extensive 3D FEA study was conducted to assess the potential effects of vertically misaligned, rotationally misaligned, and bent steel laminates on the performance of bearings subjected to maximum service loading according to AASHTO's Method B (2017). In this regard, finite element models of bearings with and without imperfections were analyzed under combined actions that

include maximum allowable compression, rotation, and shear displacement. The study was focused on the deformation pattern in the bearings, shear strain and bond stress at steel–rubber interfaces, potential plastic damage in the steel laminates, and vertical stiffness and deflection of the bearings. The following conclusions were made:

- The peak interfacial shear strain demands on all examined bearings were considerably lower than what was expected according to the linear analytical solutions mainly due to the strain hardening of the rubber close to the edges of laminates.
- Depending on the rubber's shear modulus and strain hardening rate, the maximum bond stress demands at steel–rubber interfaces can be substantially different. This shows that the total shear strain approach used in the design of elastomeric bearings might be insufficient in ensuring a bearing's safety.
- Imperfections can considerably increase the overall bulging of critical rubber layers, making them visually objectionable. However, the peak interfacial shear strain demand and bond stress demands (i.e., most important performance variables, the increase of which expedite shear delamination in bearings) were minimally affected by the imperfections.
- The steel laminates in especially examined fully unbonded bearings flexed close to their edges, which could lead to the yielding of at least one laminate in most of the unbonded bearings without imperfections. Although the yielded laminates experienced very modest levels of strain ductility, the observed yielding shows that the design provisions specified by bridge codes (e.g., AASHTO (2017) and CSA (2019)) on the laminate thickness is not necessarily sufficient for preventing laminate yielding.
- The examined imperfection forms increase plasticity in the steel laminates, but the vertical misalignment of laminates leads to more plasticity compared to their rotational misalignment and bent shapes. In summary, examined imperfections could increase the yielded area in steel laminates by up to 70%.

- The simultaneous rotational misalignment or bending of all laminates did not cause substantial differences in the stiffness and deflection compared to what are caused by a single-laminate imperfection.
- Imperfections almost always decrease the vertical stiffness or increase the vertical deflection. However, the increased vertical deflections due to imperfections were minimal (i.e., less than 1 mm), demonstrating no need for concern about the vertical behavior of bearings with imperfections in at least short-term.

5.2.3 Behavior of Elastomeric Bearings Subjected to Large Lateral Displacements

Following the 3D FEAs conducted to assess the service-level performance of bearings with and without imperfections, 3D FEAs were also undertaken to investigate the behavior of fully unbonded bearings with and without imperfections under large cyclic lateral displacement. Of primary focus was how steel laminate thickness affects the behavior of bearings with different characteristics in terms of plan dimensions, number and thickness of steel laminates, shape factor, and imperfection forms including rotationally misaligned and bent laminates. Vertically misalignment of laminates was not included in this study because preliminary FEAs showed that this imperfection form has negligible effect on the lateral behavior of bearings. The examined bearings were subjected to axial loads equivalent to an average pressure of 5.5 MPa, followed by five cycles of lateral displacements with increasing amplitudes, up to 200% of their total rubber thickness (i.e., equivalent shear strain of 2). The study was focused on the deformation and displacement patterns in the examined bearings, their lateral force and hysteretic response characteristics at different equivalent shear strains, and the potential plastic damage in their steel laminates. The study found that:

- All examined bearings experienced shear deformations in their central portions with curling deformations at their corners, and minor slippage under the cyclic displacement, and they could maintain stable lateral response under the five-cycle loading protocol of this study.

- Imperfections can increase or decrease the roll-off amount in bearings depending on the imperfection type (i.e., rotational misalignment or bending) and the shearing direction. Especially, the rotationally misaligned laminates had the largest effect on the roll-off amount and could expedite the rollover of the bearings in lower shear strains.
- At relatively high equivalent shear strains (e.g., 2), the roll-off amount was substantially dependent on the steel laminate thickness in slender bearings (i.e., bearings with second shape factors lower than 3).
- The examined bearings showed narrow hysteretic loops with effective damping ratios ranging from about 3% to 9% depending on not only the material and thickness properties of the rubber component but also the geometric characteristics of bearings such as slenderness of bearing and thickness of steel laminates. The effective lateral stiffness of bearings varies from 55% to 100% of their nominal shear stiffness depending on mainly the geometric characteristics of bearings and target shear strain.
- The examined bearings with 2-mm thick laminates and second shape factor of 3 (i.e., the minimum allowed in Ontario for the service-level condition) could barely avoid instability up to 2.0 ESS. Thick steel laminates (e.g., 4-mm thick) can effectively prevent the potential instability of slender bearings by increasing their tangent stiffness at high shear strains.
- The examined imperfections could increase the effective stiffness and the lateral force of bearings at a target sharing strain by up to 18% and 40%, respectively, and could negligibly affect their damping capacity. The increased lateral force and stiffness of bearings can be interpreted as the increase in force transferred to the substructure under seismic actions.
- Under cyclic displacement, the plastic damage tends to spread over all steel laminates rather than intensify in a small region. For instance, under the five-cycle loading protocol, the plasticity could spread over up to approximately 75% of the total plan area of all laminates in one bearing. However, the experienced ductility of all steel laminates in all examined bearings was much smaller than the ductility of mild steel at fracture. The yielded portions of steel laminates were still in the early portions of the

strain-hardening stage of steel and thus could effectively constrain the lateral bulging of rubber layers.

- Plastic damage grows under subsequent cycles of the same amplitude, and thus steel laminates might eventually lose their effectiveness if bearings are subjected to a large number of displacement cycles with the same amplitude.
- Both thickness properties and placement conditions of steel laminates have considerable effects on the induced plastic damage under cyclic lateral displacement.
- During a strong earthquake, the increased plastic damage in both bearings with and without imperfections and with thin laminates (e.g., 2-mm thick) is not expected to cause an immediate failure of these bearings (e.g., laminate fracturing and loss of axial load capacity), provided that limited or no plastic damage occurs prior to it under the service-level condition.

5.2.4 Recommendations for Practice

This section presents recommendations useful for practice regarding the manufacturing imperfections and also design of elastomeric bridge bearings.

- If the 3D-DIC system is set appropriately and permanently beside a compression testing machine, the developed vision-based methodology enables the efficient identification of the internal structure of elastomeric bearings and their potential imperfections. Therefore, the developed methodology is strongly recommended to transportation departments/ministries and elastomeric bearing manufacturers as an alternative to the current destructive procedures for quality control testing of elastomeric bearings.
- For bearings subjected to service loading, imperfections can be troublesome with regard to only their effects on the plastic damage to the steel laminates. Therefore, preventing plastic damage by using sufficiently thick laminates (e.g., 4-mm-thick for demands close to maximum service loading) or by avoiding demands close to maximum service loading is recommended. Maximum service loading is meant the loading that cause the effective shear strain of 5 in the rubber of bearings according to bridge codes (e.g., AASHTO (2017) and CSA (2019)).

- Considering the observed plastic damage in the steel laminates of the examined bearings without imperfections, sufficiently thick laminates (e.g., 4-mm-thick) are recommended in bearings designed for loading demands close to maximum service loading.
- Slender unbonded bearings with thin steel laminates (e.g., 2-mm-thick) should be avoided in bridges due to their high risks of instability and rollover and rapid spread of plastic damage in their laminates under cyclic displacement.
- As long as plastic damage in the laminates is prevented under service loading by avoiding imperfections and also demands close to maximum service loading, thinner steel laminates (e.g., 2-mm-thick) are recommended in short unbonded bearings because of their lower cost and weight, and the limited risk of rollover under seismic-level demands.
- Slender unbonded bearings in which the majority of laminates feature relatively large rotational misalignments (in the order of 0.025 rad, or more) should be avoided due to their increased risk of instability under large lateral displacements.
- During a seismic event, imperfections in the bearings of a bridge might increase the force demands transferred to the bridge substructure before their full sliding. Therefore, the potential effects of such an increase in force demands on the vulnerability of other bridge components is suggested to be evaluated before bearings with imperfections are used in a bridge. In this regard, simulations and seismic performance of bridges featuring bearings with modified effective lateral stiffnesses and damping accounting for potential imperfections are recommended.

5.3 Recommendations for Future Research

This section presents the proposed future research to extend the application of 3D-DIC on the performance assessment of elastomeric bearings, to complement the understanding about the effects of imperfections in elastomeric bearings, and to improve the design tolerances and quality control testing procedures.

- The vision-based assessment methodology developed in this study (which requires the implementation of 3D-DIC) was limited to elastomeric bridge bearings. Future studies can focus on extending the proposed methodology to seismic-isolation elastomeric bearings. These bearings are intended to sustain extreme load and displacement demands caused by seismic excitations, and they are needed to meet more stringent quality requirements. These bearings have very high shape factors, which is equivalent to low thicknesses of their rubber layers, and their lateral bugling is hardly detectible under pressure. Also, seismic-isolation elastomeric bearings are usually circular and thus have curved vertical surfaces which is different from rectangular bearings. These features of seismic-isolation elastomeric bearings might affect the accuracy of the proposed methodology or cause new challenges in the application of 3D-DIC for their quality control assessment.
- The application of 3D-DIC can also be extended to improve or calibrate analytical or numerical models of elastomeric bearings under various states of deformation, (i.e., compression, rotation, and shear), as well as combinations thereof. For instance, it was observed that the analytical solutions in AASHTO (2017) for the design of bearings cannot predict the true shear strains accurately or prevent the yielding of steel laminates in bearings without imperfections. In this regard, validated finite element models of bearings with 3D-DIC measurements can be used to better calibrate the analytical solutions or improve different formula used for the design of bearings.
- Although the results of this research study indicated that imperfections are expected to have negligible effects on the shear delamination of bearings due to cyclic loading, further cyclic compression and cyclic shear tests on bearings with imperfections are suggested. In this context, the 3D-DIC can be used to assess the imperfection effects on the onset and propagation of the debonding of rubber from steel laminates. Such a failure appears on the surface of a bearing in form of merging two discrete lateral bulging of rubber layers into a larger one on the surface of bearings. Therefore, 3D-DIC can be used to meticulously monitor any minor evolution of the deformation pattern on the surface toward the coalescence of two discrete lateral bulging (i.e., the

onset of debonding). DIC would be also helpful to monitor the spread of this coalescence along the critical side of bearings up to 25% of the bearing's length (which is considered to be the failure limit of bearings according to AASHTO (2017)).

- Considering the observed yielding of steel laminates in bearings without imperfections under service-level loading and also the increased plastic damage due to imperfections, further cyclic tests with sufficiently large number of cycles are suggested to investigate how this kind of damage affects their long-term performance under service-level condition. Although the induced plastic damage in the bearings examined in this study caused negligible difference in their overall short-term behavior, the plastic damage was observed to grow with repeated cycles of the same amplitude. Therefore, the effect of plastic damage growth in their long-term behavior is suggested to be investigated.
- This study focused on the lateral behavior of only unbonded elastomeric bearings. Further research is suggested to investigate the effects of bent and rotationally misaligned steel laminates on the lateral behavior of fully bonded elastomeric bearings. The lateral behavior of fully bonded bearings is expected to be quite similar to the lateral behavior of short unbonded bearings with limited roll-off and no sliding. It was observed that the increases in lateral force and stiffness of short unbonded bearings due to imperfections intensifies at higher equivalent shear strains (e.g., equivalent shear strain of 2). However, the force capacity of unbonded bearings is generally limited to the frictional resistance of the interfaces, and these bearings are expected to experience sliding at equivalent shear strains slightly lower or higher than 2. However, fully bonded bearings would be able to experience larger equivalent shear strains before reaching their force capacity, and thus any further increase in lateral force and stiffness of fully bonded bearings due to imperfections would become much more critical at larger shear strains.
- There are scenarios in which elastomeric bearings are subjected to light axial loads and large rotations. In such scenarios, fully bonded bearings experience hydrostatic tension stress on their tension sides, which can lead to, at worst, the sudden, brittle, internal rupture of rubber there (i.e., usually referred to as uplift). Similarly, fully unbonded

bearings experience lift-off in which some parts of the bearings' top surface are separated from the end plates, resulting in significant increase in the stress and strain demands on their loaded region. Both lift-off and uplift are undesirable phenomena and should be avoided. In this regard, further research is suggested to investigate whether manufacturing imperfections in bearings may or may not increase their vulnerability under these circumstances.

- The potential effects of imperfections in bearings on the performance of bridges subjected to seismic excitations is an area that requires study. This would advance the knowledge of the effects of imperfections in bearings from the component level to the system level. In this context, suitable nonlinear models for the axial, rotational, and shear behavior of bearings with imperfections are needed to be developed using the results of a comprehensive numerical or experimental study. Models of bearings with imperfections are needed to be implemented in a suitable bridge model. Finally, the performance assessment of such a bridge model under seismic excitations would provide valuable information about the effects of imperfections in bearings on the vulnerability of other bridge components. For instance, the detrimental effects of increase in the lateral stiffness of bearings and thus the expected increase in inertial force transferred to the substructure due to imperfections is needed to be investigated.

References

AASHTO. (American Association of State Highway and Transportation Officials). 2017. *AASHTO LRFD bridge design specifications*. Washington, DC: AASHTO.

AASHTO. (American Association of State Highway and Transportation Officials). 2018. *Standard specification for plain and laminated elastomeric bridge bearings*. Washington, DC.

CSA. (Canadian Standards Association). 2019. *S6-19 Canadian highway bridge design code*. Section 11: Joints and Bearings. Toronto, Ontario.

OPSS. (Ontario Provincial Standard Specification). 2017. *Material specification for bearings - elastomeric plain and steel laminated*.